



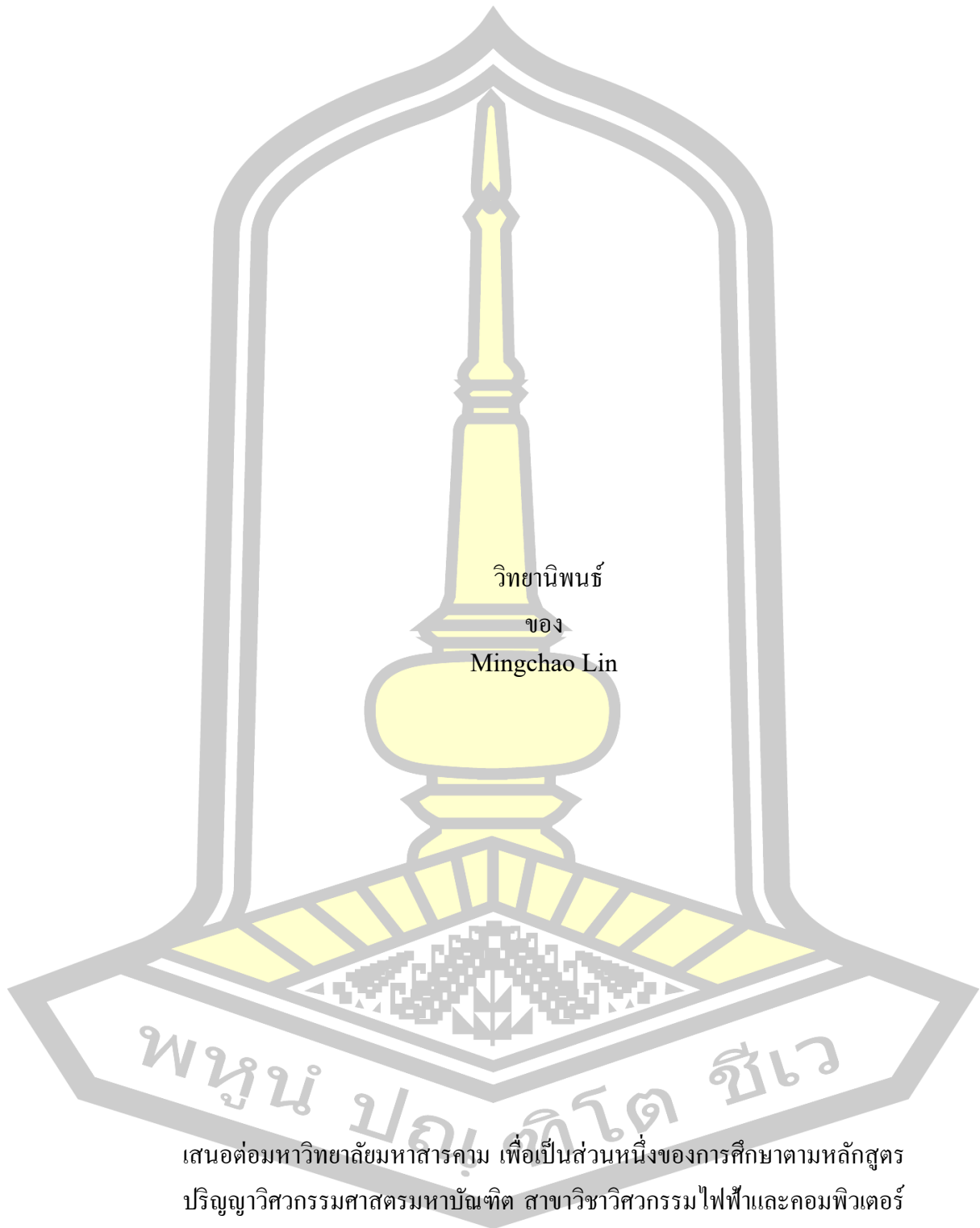
Smart Sensor for Current Leakage Detection for EV Charger Station

Mingchao Lin

A Thesis Submitted in Partial Fulfillment of Requirements for
degree of Master of Engineering in Electrical and Computer Engineering
February 2024

Copyright of Maharakham University

Smart Sensor for Current Leakage Detection for EV Charger Station



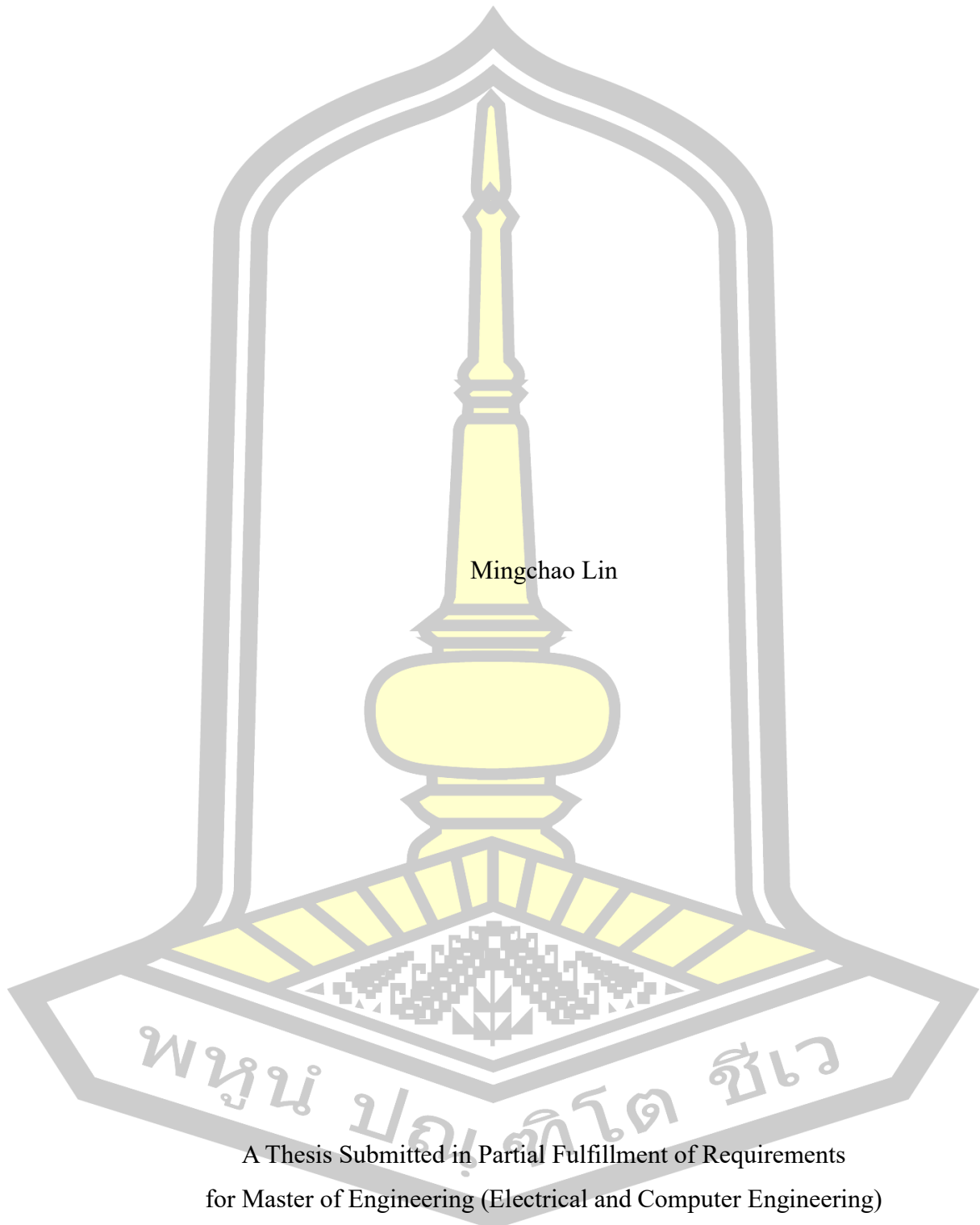
วิทยานิพนธ์
ของ
Mingchao Lin

เสนอต่อมหาวิทยาลัยมหาสารคาม เพื่อเป็นส่วนหนึ่งของการศึกษาตามหลักสูตร
ปริญญาวิศวกรรมศาสตรมหาบัณฑิต สาขาวิชาวิศวกรรมไฟฟ้าและคอมพิวเตอร์

กุมภาพันธ์ 2567

ลิขสิทธิ์เป็นของมหาวิทยาลัยมหาสารคาม

Smart Sensor for Current Leakage Detection for EV Charger Station



Mingchao Lin

A Thesis Submitted in Partial Fulfillment of Requirements
for Master of Engineering (Electrical and Computer Engineering)

February 2024

Copyright of Mahasarakham University



The examining committee has unanimously approved this Thesis, submitted by Mr. Mingchao Lin , as a partial fulfillment of the requirements for the Master of Engineering Electrical and Computer Engineering at Mahasarakham University

Examining Committee

..... Chairman
(Asst. Prof. Adirek Jantakun , Ph.D.)

..... Advisor
(Assoc. Prof. Chonlatee Photong ,
Ph.D.)

..... Committee
(Asst. Prof. Nawarat Piladaeng ,
Ph.D.)

..... Committee
(Asst. Prof. Chaiyong Soemphol ,
Ph.D.)

Mahasarakham University has granted approval to accept this Thesis as a partial fulfillment of the requirements for the Master of Engineering Electrical and Computer Engineering

.....
(Assoc. Prof. Keartisak Sriprateep ,
Ph.D.)
Dean of The Faculty of Engineering

.....
(Assoc. Prof. Krit Chaimoon , Ph.D.)
Dean of Graduate School

พญม ปณทโท ขเ

TITLE Smart Sensor for Current Leakage Detection for EV Charger Station

AUTHOR Mingchao Lin

ADVISORS Associate Professor Chonlatee Photong , Ph.D.

DEGREE Master of Engineering **MAJOR** Electrical and Computer Engineering

UNIVERSITY Mahasarakham University **YEAR** 2024

ABSTRACT

In the growing electric vehicle market, the efficiency, cost, and safety requirements of charging stations are increasing. Non-isolated DC charging stations use AC/DC non-isolated converters, which provide higher efficiency, lower cost, and greater potential for growth compared to traditional industrial frequency or high frequency AC/DC converters. However, when compared to traditional charging stations that are isolated from the grid, non-isolated DC charging stations have the potential risk of leakage current rising to dangerous levels. Therefore, this paper thoroughly analyzes the negative effects of leakage current in non-isolated charging stations and proposes a fluxgate leakage current sensor suitable for detecting leakage current in non-isolated DC charging stations.

This paper identifies the location of leakage current detection by analyzing the generation mechanism and current path of the AC/DC non-isolated converter. The Jiles-Atherton hysteresis model is established and solved using the fourth-order Lunger Kuta method to accurately describe the B-H mapping relationship. The mathematical model is optimized to consider the effect of temperature. This text presents an analysis of the sensor temperature drift problem and proposes an aerogel thermal insulation scheme to optimize sensor performance under DC charging station operating conditions. The effect of the insulation scheme on the performance of the leakage current sensor is evaluated using ANSYS thermal simulation. Additionally, a MATLAB simulation model is used to analyze the effect of relative capacitance on the accuracy of the fluxgate sensor. These research results support the improvement of charging station safety and performance.

Keyword : Non-isolated DC charging stations, leakage current, fluxgate, Jiles-Atherton hysteresis, aerogel thermal insulation

ACKNOWLEDGEMENTS

As I wrote this acknowledgement, the dissertation chapter was coming to an end, and I felt a sense of relief, but also a little reluctance to say goodbye. My master's program is coming to an end, which means that I am saying goodbye to my student days, and I have many feelings as I look back on this period of growth. I would like to take this opportunity to express my heartfelt gratitude to my teachers, friends and family who have helped me in my life and studies.

First and foremost, I would like to express my heartfelt gratitude to my advisor, Dr. Chonlatee Photong. From choosing my topic to completing my dissertation, I owe my progress to the patience and guidance of my advisor. My advisor's advice has been a beacon of light in my journey.

I would like to thank my Ph.D. brothers, especially Wenwei Li, Jun Shen, and Can Zhu, whose guidance and help were the important support for me to laugh at the difficulties and grow up together in the early stage of my study. Looking back on my time in Thailand, I can't forget the wonderful time I spent with my classmates doing research and experiments, and sharing laughs and trivialities of life after work.

To my friends who are studying or working far away, thank you for your encouragement and listening, which made me feel warm in a foreign country. Your company is the biggest help for me to move forward in my life.

Finally, to my family, I am eternally grateful. Thank you for your support and understanding at every important point of my life, it is your company that makes me move forward. To all my teachers, classmates, and family members who have helped me, I thank you from the bottom of my heart.

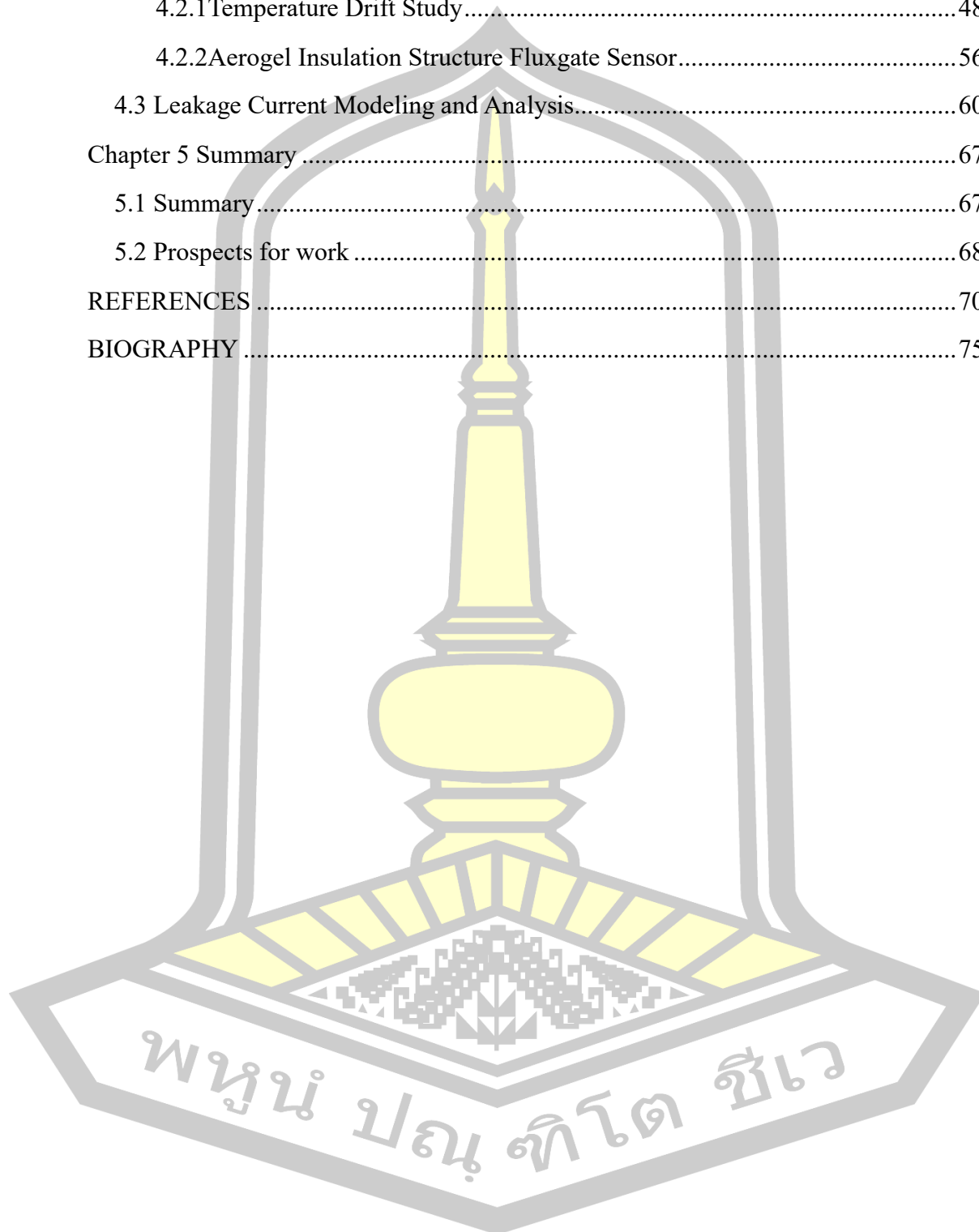
พหุบัณฑิต ชีวะ

Mingchao Lin

TABLE OF CONTENTS

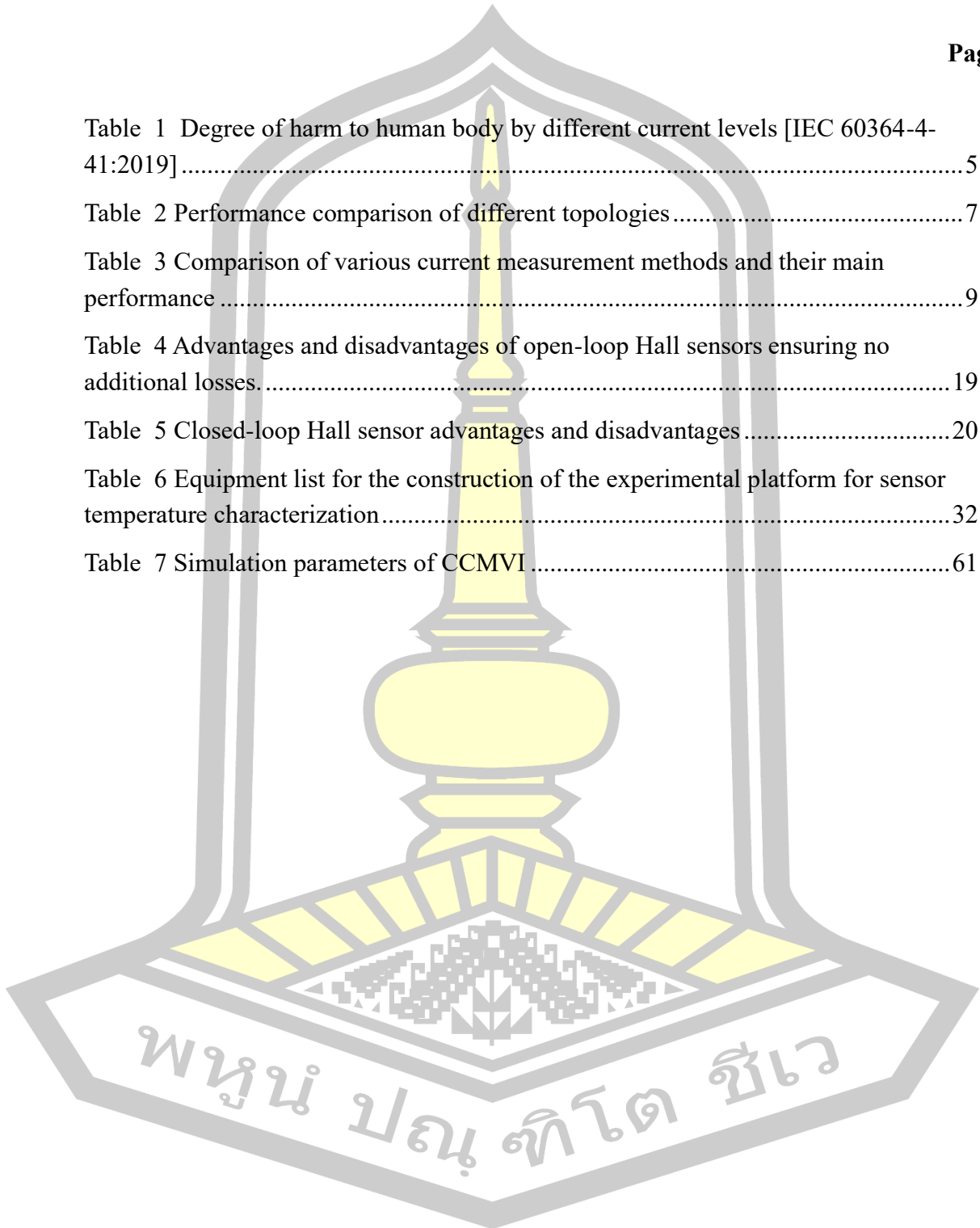
	Page
ABSTRACT.....	D
ACKNOWLEDGEMENTS.....	E
TABLE OF CONTENTS.....	F
LIST OF TABLES.....	H
LIST OF FIGURES.....	I
Chapter 1 Introduction.....	1
1.1 Research background.....	1
1.2 Objectives.....	11
1.3 Research Benefits.....	11
Chapter 2 Literature Reviews.....	13
2.1 Current Status of Research on Leakage Current in Non-Isolated Low-Voltage DC Power Supply Systems.....	13
2.2 Current research status of leakage current detection technology.....	15
2.2.1 shunt.....	16
2.2.2 Hall sensor.....	17
2.2.3 Fluxgate sensor.....	20
2.3 MEMS fluxgate sensor.....	24
Chapter 3 Research Methodology.....	28
3.1 Analysis of the Leakage Current Mechanism to Establish the Common Mode Equivalent Model of the Stack Circuit.....	28
3.2 Temperature characterization of fluxgate sensors, insulation scheme design. ...	30
Chapter 4 Results and Discussions.....	34
4.1 Leakage analysis of DC charging station.....	34
4.1.1 Different earthing systems.....	35
4.1.2 AC side leakage analysis.....	38
4.1.3 DC side leakage analysis.....	41

4.2 Sensor Temperature Characterization Study.....	48
4.2.1 Temperature Drift Study.....	48
4.2.2 Aerogel Insulation Structure Fluxgate Sensor.....	56
4.3 Leakage Current Modeling and Analysis.....	60
Chapter 5 Summary.....	67
5.1 Summary.....	67
5.2 Prospects for work.....	68
REFERENCES.....	70
BIOGRAPHY.....	75



LIST OF TABLES

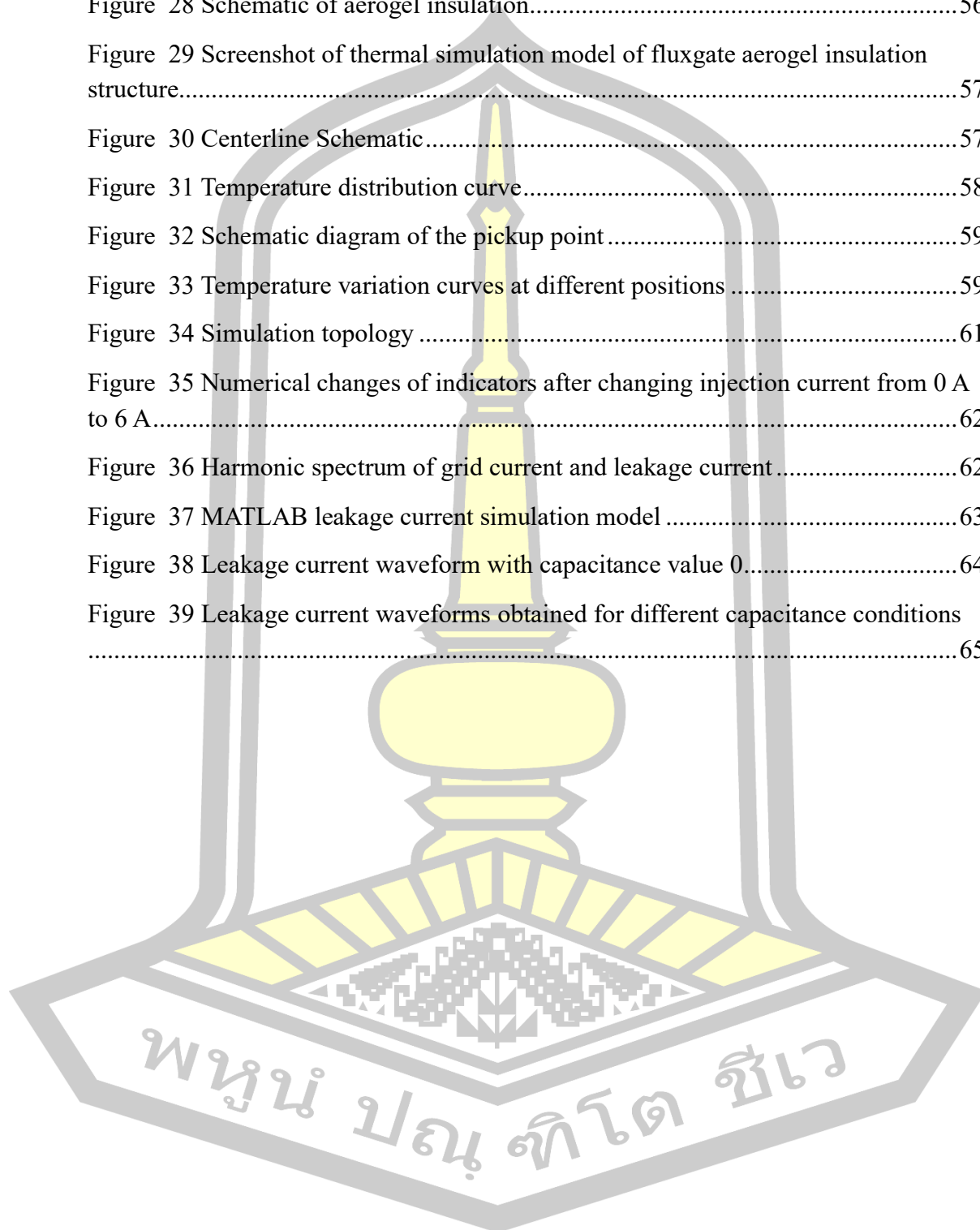
	Page
Table 1 Degree of harm to human body by different current levels [IEC 60364-4-41:2019].....	5
Table 2 Performance comparison of different topologies.....	7
Table 3 Comparison of various current measurement methods and their main performance	9
Table 4 Advantages and disadvantages of open-loop Hall sensors ensuring no additional losses.....	19
Table 5 Closed-loop Hall sensor advantages and disadvantages.....	20
Table 6 Equipment list for the construction of the experimental platform for sensor temperature characterization.....	32
Table 7 Simulation parameters of CCMVI.....	61



LIST OF FIGURES

	Page
Figure 1 Splitter	16
Figure 2 Principle of the Hall effect.....	17
Figure 3 Principle of open-loop Hall sensors.	18
Figure 4 Principle of closed-loop Hall sensors.	19
Figure 5 Fluxgate Sensor	21
Figure 6 Core excitation voltage signal at $I_p=0$	21
Figure 7 Core excitation voltage signal when $I_p \neq 0$	22
Figure 8 Variation curve of magnetic permeability μ	23
Figure 9 Aerogel preparation process	27
Figure 10 MATLAB simulation steps.....	29
Figure 11 ANSYS thermal simulation steps	31
Figure 12 Temperature Characterization Experiment Procedure.....	32
Figure 13 Schematic diagram of DC charging stations system	34
Figure 14 TT grounding system.....	36
Figure 15 TN grounding system	37
Figure 16 IT Grounding System	38
Figure 17 Schematic diagram of AC ground fault measurement.....	39
Figure 18 Schematic of common mode current.....	42
Figure 19 Simplified diagram of common mode circuit.....	43
Figure 20 Simplified path of common mode current.....	44
Figure 21 System leakage current distribution	44
Figure 22 Equivalent Circuit Diagram for Zero Protection	46
Figure 23 Leakage current simulation schematic	47
Figure 24 V-T diagram of fluxgate sensor without aerogel structure.....	49
Figure 25 B-T Mapping Relationship	51
Figure 26 Hysteresis regression line	54

Figure 27 MATLAB fitting of hysteresis return curve with temperature	55
Figure 28 Schematic of aerogel insulation.....	56
Figure 29 Screenshot of thermal simulation model of fluxgate aerogel insulation structure.....	57
Figure 30 Centerline Schematic.....	57
Figure 31 Temperature distribution curve.....	58
Figure 32 Schematic diagram of the pickup point	59
Figure 33 Temperature variation curves at different positions	59
Figure 34 Simulation topology	61
Figure 35 Numerical changes of indicators after changing injection current from 0 A to 6 A.....	62
Figure 36 Harmonic spectrum of grid current and leakage current	62
Figure 37 MATLAB leakage current simulation model	63
Figure 38 Leakage current waveform with capacitance value 0.....	64
Figure 39 Leakage current waveforms obtained for different capacitance conditions	65



Chapter 1 Introduction

1.1 Research background

In recent years, the world has been faced with increasingly serious environmental pollution and energy shortages, which have fueled the development of new green energy sources and become an international consensus. In particular, China has put forward a "double carbon" target, emphasizing carbon emission reduction and carbon peaks, which has led to a gradual expansion of the market share of green energy. Against this backdrop, electric vehicles, as green new energy vehicles, have gradually become mainstream in market development. By 2021, the number of electric vehicles worldwide has exceeded 10 million [1]. Global electric vehicle sales are expected to maintain strong growth in the future, with an estimated Compound Annual Growth Rate (CAGR) of approximately 22%. The market size of the industry is expected to reach approximately \$700 billion by 2028 [2]. Electric vehicles, as an environmentally friendly and efficient means of transport, are gradually gaining widespread attention worldwide. Its importance is reflected in environmental protection, energy sustainability, reduction of energy costs, and innovative technology drive. Electric vehicles are an environmentally friendly option that eliminates tailpipe emissions, reduces air pollution, and improves energy sustainability by utilizing renewable energy sources. They have relatively low running costs, and the stable price of electricity enables users to save on fuel costs in the long term. Furthermore, the development of electric vehicles has driven technological innovation and facilitated advances in areas such as battery technology, charging technology, and smart driving. These factors are driving society towards a more sustainable and innovative direction.

Various governments have implemented policy measures to support the development of electric vehicles. The Chinese government has been particularly supportive and has launched a series of policies, such as car purchase subsidies, free license plates, and free parking, to encourage consumers to buy electric vehicles. Furthermore, China has implemented rigorous standards for vehicle emissions, which has led automakers to expedite the development and manufacturing of electric

vehicles [4]. Several European countries have implemented policies to promote the use of electric vehicles, including car purchase subsidies, tax exemptions, and the development of extensive charging infrastructure networks. Norway and the Netherlands have even set timetables to ban the sale of fuel vehicles [5]. In the United States, the government has introduced federal and state-level tax incentives to encourage the purchase of electric vehicles. Some states have set zero-emission vehicle goals and provided funding for charging infrastructure [6]. Government-level support and guidance have facilitated the significant global growth of electric vehicles, promoting the transformation of sustainable transportation. Effective policy implementation has provided a strong impetus for the electric vehicle industry, enabling it to rapidly develop from an emerging technology to a mainstream transportation option with broad market share and consumer recognition. The demand for charging stations is driven by the need to charge electric vehicles and is essential for the widespread adoption of electric vehicles. Electric vehicles are closely tied to charging stations. The demand for charging stations is driven by the need to charge electric vehicles and is essential for the widespread adoption of electric vehicles. As the number of electric vehicles increases, it is crucial to expand and optimize the charging infrastructure to meet the growing demand. When choosing electric vehicles, users now consider range and charging speed as important factors. The continuous innovation of power battery technology has improved the cruising range of electric vehicles, which is gradually approaching or even surpassing that of traditional fuel vehicles. However, the development of charging technology has not kept pace, and has become a bottleneck that restricts the popularity of electric vehicles. According to data from May 2022, China alone has approximately 3.581 million charging stations, of which 1.411 million are public charging stations [7]. This significant number highlights the importance of constructing charging stations to meet the changing requirements of electric vehicle users in different situations and to further the advancement of electric vehicles.

In summary, EV charging stations are critical to promoting EV adoption, driving environmental sustainability, reducing dependence on fossil fuels, and delivering economic, technological and social benefits. The expansion and ubiquity of

charging infrastructure is a key component of the transition to a more sustainable, low-carbon transportation system.

The rise of electric vehicles has led to the rapid development of charging facilities and diversified charging methods. Currently, electric vehicle charging methods are mainly divided into standard charging and fast charging. Standard charging, also known as 'slow charging', has lower charging power and takes longer (usually within 5 to 10 hours) to fully charge. However, it has lower requirements for charging facilities. DC charging stations are used for fast charging and can charge the battery to 80% in 20 to 120 minutes. While the charging power is higher, it comes with increased construction and installation costs, as well as potential impacts on the battery pack and charging equipment safety. These requirements are more stringent [8].

Mainstream DC charging stations in the Chinese market typically have a charging power of 60 to 80 kilowatts, requiring 1 to 2 hours for a full charge. To reduce charging time, high-power DC fast charging has emerged, with a charging power of up to 350 kilowatts. This technology allows for a battery life comparable to that of fuel vehicles in just 10 to 30 minutes [9]. Traditional chargers typically use a structure that is isolated from the power grid. However, non-isolated integrated chargers are becoming increasingly popular to increase the charging power of electric vehicles, reduce charging system costs, and achieve compact designs during the charging process. Non-isolated chargers have broad market prospects in the electric vehicle industry and are expected to become the next important trend in technological development. The development of this technology is expected to enhance the charging speed, efficiency, and popularity of electric vehicles, providing new opportunities for the industry.

While DC distribution systems offer advantages such as low system complexity, large capacity, and small line loss, the expansion of DC network scale and increase of DC load types have led to an increase in electrical safety hazards. Currently, research on protection technology for DC distribution systems is still in its early stages. Traditional protection technology used for AC systems cannot be directly applied to DC systems, which has hindered the development of DC distribution systems. Compared to the AC power grid, a DC system offers convenient access to

distributed power sources. However, in order to interact with the AC power grid, the DC system must be equipped with an AC/DC converter. Non-isolated AC/DC converters can improve efficiency and reduce costs, but they come with the drawback of losing the electrical isolation function of the transformer. This increases the risk of electric shock in non-isolated low-voltage DC power supply systems, making electrical safety a key issue that limits the application of non-isolated systems [10].

In low-voltage DC power supply systems, selecting a non-isolated structure can result in various issues, including leakage current. Leakage current refers to the flow of electricity through exposed or unintended parts, which can pose a risk to electrical safety. Common-mode voltage charging and discharging the distributed capacitance of the system to ground is one of the primary sources of leakage current. In addition to cable-to-ground distributed capacitance, distributed power sources such as photovoltaics and energy storage also have distributed capacitance to ground. The distributed capacitance to ground of crystalline silicon photovoltaic cells is approximately 50-150nF/kWp, while the distributed capacitance to ground of thin film photovoltaic cells is approximately 1 μ F/kWp. The high-frequency changing common-mode voltage interacts with the distributed capacitances, causing them to charge and discharge. This generates leakage current in the common-mode loop, which is composed of the power grid, converter, distributed capacitance, and the earth. Leakage current flow can cause various issues, such as harmonic pollution of the power grid and equipment aging. This can further compromise the system's electric shock protection performance and even personal safety.

According to IEC 60364-4-41:2019, the harm caused by electric current to the human body increases with the current strength. Table 1 shows the maximum current that an adult male and female can withstand, which is approximately 16mA and 10.5mA, respectively. At 20mA, the human body experiences severe pain and breathing difficulties. A current of 50mA or more can cause serious conditions such as ventricular fibrillation and respiratory paralysis and may even lead to sudden death. Additionally, a current of 100mA can be fatal if it lasts only 1 second.

Table 1 Degree of harm to human body by different current levels [IEC 60364-4-41:2019]

Current size	the level of danger	effect
< 1mA	No perception	Usually, no noticeable sensation
1-5mA	weak feeling	A slight tingling sensation, similar to a needlepoint irritation
5-16 mA	Muscle paralysis, which can cause death	Muscle paralysis, which may cause difficulty breathing but is usually not fatal
16-20mA	Muscle paralysis, fatal threshold	In adult males, may cause heart palsy
20-50mA	Severe pain, difficulty breathing	Intense, severe pain that may cause difficulty breathing but is usually not fatal
50-100mA	ventricular fibrillation, respiratory paralysis, fatal threshold	May cause cardiac ventricular fibrillation, respiratory paralysis, and fatal
>100mA	Instantly fatal	Currents greater than 100 mA may cause instant death in a short period of time

Charging stations offer convenience for electric vehicles, but it is important to also consider potential safety hazards associated with electricity use. In recent years, there have been reports of accidents caused by charging electric vehicles [11]. To enhance the safety of charging stations, the Chinese government established the national standard GB/T18487.1-2015. This standard mandates that charging piles must be equipped with insulation monitoring devices to ensure electrical isolation and user safety during the charging process. The objective of this requirement is to safeguard users from electrical hazards and promote safe development in the electric vehicle charging industry.

When using a non-isolated converter, the AC side and DC side of the charging pile will be coupled to the ground through the power converter, and the existence of parasitic capacitance of the charging system to the ground is inevitable. When there is an unbalanced load on the DC network, common mode voltage and leakage current may be generated [12]. In actual engineering, because it is difficult to achieve complete symmetry of circuit parameters and parasitic parameters, domestic and

foreign scholars have conducted a lot of research. At present, there are two main ways:

1. Propose a topology that reduces leakage current generation and ensures compliance with relevant safety standards.
2. Implement methods to detect leakage current and enhance the safety of the charging system.

In order to reduce and eliminate leakage current, the circuit is currently optimized through the following topologies:

Full H4-bridge topology: In order to deal with possible leakage current problems in full H-bridge photovoltaic inverters, an effective method is to use bipolar PWM modulation technology. The main goal of this modulation technique is to eliminate the high-frequency components of the common-mode voltage on the circuit to reduce the generation of leakage current. With bipolar PWM modulation, the common-mode voltage typically contains only a low-frequency component of one harmonic, thereby reducing the adverse effect on leakage current.

H5 bridge topology: This topology is improved on the basis of the H 4 bridge inverter. Through a specific control strategy, the generation of leakage current can be reduced, thereby improving the safety and efficiency of the charging system.

Heric topology: Heric topology is an improved structure based on the full-bridge converter. It can reduce the risk of leakage current and improve the performance of the charging system by optimizing the layout and control strategy of the circuit.

H6 bridge topology: The H6 bridge is developed on the basis of the H-bridge topology. It achieves finer control by adding more switch tubes and diodes, thereby reducing leakage current problems.

a switch tube in series on the H5 bridge: This structure combines the H5 bridge with a series switch tube, which can effectively suppress leakage current and improve the electrical performance of the charging system.

For the above-mentioned commonly used topologies that can suppress leakage current, we can compare and analyze them in terms of the number of switch tubes, the

number of diodes, the number of input capacitors, EMI suppression capabilities, efficiency, and application conditions, as shown in Table 2.

For the above-mentioned commonly used topologies that can suppress leakage current, we can compare and analyze them in terms of the number of switch tubes, the number of diodes, the number of input capacitors, EMI suppression capabilities, efficiency, and application conditions, as shown in Table 2.

Table 2 Performance comparison of different topologies

Topology	Number of switch tubes	Number of diodes	icM suppression ability	Efficiency range	Application	
Full bridge	H5	5	0	good	higher	widely used
	HB_ZV R	5	5	good	higher	laboratory
	FB-DCBypass	6	2	good	higher	widely used
Improve topology	Heric	6	2	better	optimal	widely used
	H6	6	2	better	higher	laboratory
Half bridge	Diode NPCs	4	2	very good	higher	widely used
	Active NPCs	6	0	very good	higher	laboratory
Improve topology	Energy NPCs	4	0	very good	high	widely used

Table 2 shows that the FB-DC Bypass topology is the most effective in suppressing leakage current, while other topologies are slightly inferior. Among the single-phase full-bridge improved topologies, the Heric topology performs best in terms of efficiency, with the smallest conduction pass loss and total loss. This type of topology generally has a high efficiency ranging from 95% to 98%, making it widely used in engineering practice [13]. Although improved leakage current suppression topologies have certain limitations and potential hazards cannot be completely eliminated, it is crucial to accurately detect leakage current to prevent electric shock to charging station operators. Real-time monitoring of leakage current allows for early warning and control, thereby preventing potential safety problems in advance.

Electric current is a fundamental physical quantity with significant importance in accurate measurement. There has been extensive research conducted by scholars both domestically and internationally. Currently, there are over a dozen widely used technologies for measuring current, which vary in implementation

difficulty, performance, and cost. These measurement methods can be broadly classified into two categories: direct and indirect measurement.

Direct measurement mainly relies on Ohm's law, which states that the output voltage at both ends is proportional to the measured current. Shunt technology is a common method used for this purpose. Direct measurement mainly relies on Ohm's law, which states that the output voltage at both ends is proportional to the measured current. It began to develop in the 1880s and is still widely used today due to its low cost and ease of use. However, when measuring large currents, shunts need to be connected in series in the circuit, resulting in significant energy losses and a lack of electrical isolation.

In industry, current sensors based on Ampere's loop law are one of the most commonly used indirect methods for measuring current. These sensors measure the magnetic field to indirectly determine the magnitude and direction of current flow, with electrical insulation between the primary and secondary sides. The current sensors used in industry typically rely on the following measurement technologies: This text describes various types of current sensors, including Hall current sensors, fluxgate current sensors, and magneto resistive (MR) current sensors such as AMR, GMR, and TMR. It also mentions Roche Coil (Rogowski coil) and current transformers. Additionally, there are current sensors that utilize magnetic fields and other physical principles for indirect measurement. These include the Faraday effect, magneto-optical effect, nuclear magnetic resonance (NMR), magnetostriction effect, Quantum Hall effect, and superconducting quantum interference device (SQUID). These technologies and their products have distinct characteristics and are utilized in various market segments. They are often complex to use and come with a higher price point.

Different application fields have different requirements for current sensors. Select the appropriate measurement method according to the specific engineering conditions to meet the requirements of measurement accuracy and economic benefits.

Table 3 Comparison of various current measurement methods and their main performance

Measurement methods	Measurement accuracy (%)	Temperature Coefficient (ppm/month)	Measure DC	Stability	Measuring range	Power consumption	Isolation or not
shunt method	0.001 ~ 0.03	3	Yes	medium	A~kA	Low	no
Hall effect method	0.5 ~ 5	50	Yes	Low	A~kA	medium	yes
fluxgate sensor	0.001 ~ 0.5	0.2	Yes	high	A~kA	Low	yes
Magneto-resistive effect method	0.5 ~ 5	100	Yes	high	A~kA	Low	yes
Nuclear Magnetic Resonance (NMR)	-	-	Yes	high	A~kA	high	yes
Rogowski coil	0.2 ~ 5	-	No	medium	A ~ MA	Low	yes
Current Transformer	0.1 ~ 1	-	No	high	A ~ kA	high	yes
magneto-optical effect	5000	100	-	high	kA~MA	high	yes

Various technologies, such as the Faraday effect, magneto-optical effect, nuclear magnetic resonance (NMR), magnetostriction effect, quantum Hall effect, and superconducting quantum interference devices, use a combination of magnetic fields and other physical principles to indirectly measure current. These technologies have unique characteristics that vary depending on their application. While some have been utilized in laboratory instruments and equipment to a limited extent, others are still in the development or improvement stage and have not yet matured. However, for widely used products like electric vehicle charging stations, the aforementioned technologies and testing methods may be too complex or expensive. The magneto-resistive and Faraday magneto-optical methods have relatively low

quantitative accuracy. The HALL sensing unit is not suitable for high-power charging conditions due to its low sensitivity and large temperature drift. In industrial and instrumentation fields, fluxgate current sensors are commonly used for precise measurement of large DC currents [14]. Fluxgate technology is currently one of the most accurate methods for measuring magnetic fields. Its induction unit can measure DC or low-frequency AC magnetic fields in the range of 10^{-10} ~ 10^{-4} T, which makes it suitable for charging pile engineering. In recent years, the rapid development of MEMS (microelectromechanical systems) sensing technology has led to the miniaturization of products and reduced costs. As a result, companies such as Swiss LEM Company, American Allegro Company, German VAC Company, and Japanese Tamura Company, among other international manufacturers, have made MEMS magnetic flux gates one of the more ideal solutions for monitoring leakage current.

The fluxgate sensor measures weak magnetic fields by utilizing the nonlinear relationship between the magnetic induction intensity and the magnetic field intensity of a high permeability magnetic core under the saturation excitation of an alternating magnetic field. This physical phenomenon can be compared to the formation of a 'door' in the measured environment, through which the magnetic flux is modulated, generating an induced electromotive force. The current can be indirectly measured by utilizing the magnetic field generated by this phenomenon.

With the continuous development of microelectromechanical systems (MEMS) technology and the expansion of research on flexible substrate materials, researchers have combined the advantages of fluxgate technology and flexible substrates to explore flexible substrate fluxgate sensors based on MEMS technology. This kind of sensor has broad application prospects in fields such as non-planar surface magnetic field detection, online current measurement, biomedical detection, wearable sensors, and flexible electronics. By optimizing the core coil topology and soft magnetic properties of the core of the fluxgate sensor, the flexible substrate fluxgate sensor is prepared using MEMS technology, which can achieve accurate detection of magnetic fields and currents. The product information currently provided by manufacturers on the market shows that it has a bandwidth of 160 kHz and a fast delay time of less than 2 μ s. MEMS fluxgate sensors are very suitable for measuring DC, AC, pulse and mixed currents. This contactless current sensing solution causes no

additional power losses and features high dielectric isolation between the main circuit and the sensor electronics. Fluxgate sensors have become one of the vector magnetic field sensors with the best overall performance due to their advantages in temperature stability, accuracy, resolution and sensitivity, as well as their simple structure and ability to measure static and low-frequency magnetic fields. The fluxgate sensor's high precision, high stability and miniaturization characteristics brought by MEMS technology will further expand its application fields.

The fluxgate sensor is prepared through the MEMS process, resulting in a smaller size and a 2/3 reduction in manufacturing costs. This technology provides a sensitive, low-power, and compact security method for popular products such as charging stations. Additionally, it has positive implications for promoting the development of the efficient DC fast charging market and the replacement of fuel vehicles with electric vehicles.

1.2 Objectives

This study analyzes the causes and mechanisms of leakage current generated by a three-phase converter in a charging pile. A common-mode equivalent model of the circuit is constructed to clarify the pathways and routes of leakage current generation. The study focuses on DC high-current measurement based on MEMS fluxgate sensors by comparing different current measurement techniques. The objective is to create a smart sensor that measures leakage current in DC charging piles, providing a precise and dependable current measurement solution.

1.3 Research Benefits

The objective of this paper is to analyze the mechanism of the leakage current generated by the charging pile converter in the electric charging system and to construct a common mode equivalent model of the circuit. To achieve this, we propose a solution using open-loop fluxgate technology after analyzing the path of common-mode current generation. The aim is to create an intelligent sensor for detecting leakage current in electric vehicle charging stations. The sensor accurately measures the parameters of the charging station's leakage current and triggers a power failure protection mechanism when abnormal conditions are detected. This ensures the safety of both the charging station and its users. Appropriate solutions will be

suggested based on the test data to ensure that the leakage current sensor can accurately measure the leakage current under the working conditions of DC charging piles. The proposed device will enhance the operational reliability of charging piles and contribute positively to the growth of the electric vehicle market.

This paper aims to address the issues of low measurement accuracy and complicated operation of traditional insulation testing devices by designing a new device that is highly accurate, easy to operate, automated, and provides fast testing in compliance with national standards. To ensure protection against electric shock risks in outdoor charging pile applications and non-professional operation, charging pile product designs must be based on solid theoretical foundations.



Chapter 2 Literature Reviews

The division of electrical systems with or without transformer power supply is used, i.e., isolated and non-isolated systems. In non-isolated systems, special attention is given to transformerless grid-connected inverters, which have the advantages of small size, low cost, and simple structure, and are especially capable of improving the efficiency of the whole system [15]. However, non-isolated DC power supply systems for charging piles pose an increased risk of electric shocks and leakage current. The latter is mainly caused by the charging and discharging of the system's distributed capacitance to ground due to the common mode voltage.

This chapter reviews the current status of research on leakage current and detection techniques for non-isolated low-voltage DC power supply systems. It introduces various principles for detecting leakage current in detail and compares their performance. The aim is to provide a comprehensive understanding of the problem of leakage current in non-isolated systems.

2.1 Current Status of Research on Leakage Current in Non-Isolated Low-Voltage DC Power Supply Systems

A great deal of research has been carried out on the leakage current problem, especially in the field of photovoltaics. One of the main ideas is to suppress the generation of leakage current by constructing a new continuation loop, disconnecting the PV cell from the AC grid side during its continuation phase, and combining it with an appropriate switching modulation method to clamp the level of the continuation loop to a fixed value, even though the common mode voltage remains unchanged [16]. In literature [12] common mode (CM) leakage currents from four non-isolated integrated charger topologies based on permanent magnet synchronous motors (PMSMs) are analyzed by on-board filters. It is illustrated that the leakage currents may reach unsafe levels and pose electrocution risks to the user. In addition, the negative safety impacts and dangers of leakage currents from different grounding systems are explored. Experimental results verify the accuracy of the leakage current analysis. Finally, leakage current mitigation methods are also presented. In the literature [17], the focus is on deriving the high-frequency common-mode equivalent model of a non-isolated single-phase grid-connected inverter with full consideration

of the parasitic parameters, and based on this model, two paths to eliminate the common-mode current are summarized. The effectiveness of the sinusoidal pulse modulation (SPWM) off approach to eliminate the leakage current in single-phase full-bridge circuits is verified by simulation and experimental means, but the leakage current cannot be completely eliminated due to the existence of parasitic parameters. Literature [18] proposes a leakage current modeling method for DC bus charging station with transformerless structure based on differential mode voltage and common mode voltage theory. The technique is based on the leakage current model to obtain mathematical analytical expressions for the common-mode voltage UCM and the leakage current leakage i . Then, it is used to analyze the three-phase DC bus charging station. Then, the three-phase SVPWM simulation is used to analyze the five different ways of organizing the rectifier space vectors. The effects of the five space vector organizations on the common-mode voltage and common-mode leakage current are tested in charging station systems with and without isolation transformers. Literature [19] In order to eliminate leakage current due to using the parasitic capacitor of PV panel, MPC control method is utilized to achieve high overall efficiency. To confirm the operation of presented structure and theoretical analysis, PSCAD/EMTDC software is used. In terms of suppressing leakage current, scholars have proposed a variety of methods from the perspectives of both topology and modulation strategy. In the area of leakage current suppression, scholars have proposed various methods from the perspective of topology and modulation strategy. For instance, several new topologies have been proposed to reduce common-mode voltage and suppress leakage current, including H5 topology [20], H7 topology [21-22], H8 topology [23], Heric topology [24], and Diode NPC [25]. However, these topologies and modulation methods have not yet been fully applied to non-isolated systems due to various reasons. The article [13] provides a comprehensive analysis of the leakage current analysis model, the switching modulation method, and the new non-isolated inverter circuit topologies. The study summarizes the advantages and disadvantages of various topologies and compares their efficiency. The results indicate that the efficiency of these topologies generally ranges from 95% to 98%, but they do not completely eliminate eventualities.

If a leakage fault occurs on the DC side, the AC side's leakage current protector (RCD) may not provide proper protection [26]. Liu et al. analyzed fault current scenarios under various grounding resistances in low-voltage DC systems and found that when the grounding resistance is high, the fault current is low, and the system's short-circuit protection may not activate [27]. The household type A RCD leakage protector has a response current of 30mA and a response time of 0.3 seconds, exceeding the requirements of the international standard IEC 62955/IEC 62752, which mandates the ability to detect 6mA DC leakage current. The phenomenon of 'blinding effect' occurs in the presence of insulation faults.

On the other hand, literature [28] analyzes the generation mechanism, influencing factors and impact of residual current on electric shock hazards in non-isolated low-voltage DC systems. Regarding electric shock hazards and protection, the authors identified deficiencies in current leakage protection for four types of residual current: contact current, ground fault current, impulse current, and leakage current. They established the necessary requirements for RCD protection functions and developed a MATLAB simulation model. Although this study provides a reference for research modeling and simulation of leakage current, it does not effectively address leakage current detection. Liu et al. obtained data on electric shock voltage and current by building a biological electric shock experimental test platform. They then applied Ohm's law to calculate the corresponding impedance values. A numerical simulation model based on MATLAB was established to simulate the transient process of biological electric shock [29]. In addition to analyzing and suppressing leakage current, it is essential to detect and provide safety protection against it.

2.2 Current research status of leakage current detection technology

Current sensors are electronic measuring instruments widely used in industrial automation control systems and energy management systems. The demand for current sensors continues to rise as global industry grows. Over a dozen current measurement techniques have been developed since the 1880s, including the use of shunts. In this context, we present a detailed introduction to various types of leakage current detection techniques for non-isolated DC charging piles. We compare these

techniques from multiple perspectives, including performance reliability, economy, scope of application, and response speed.

2.2.1 shunt

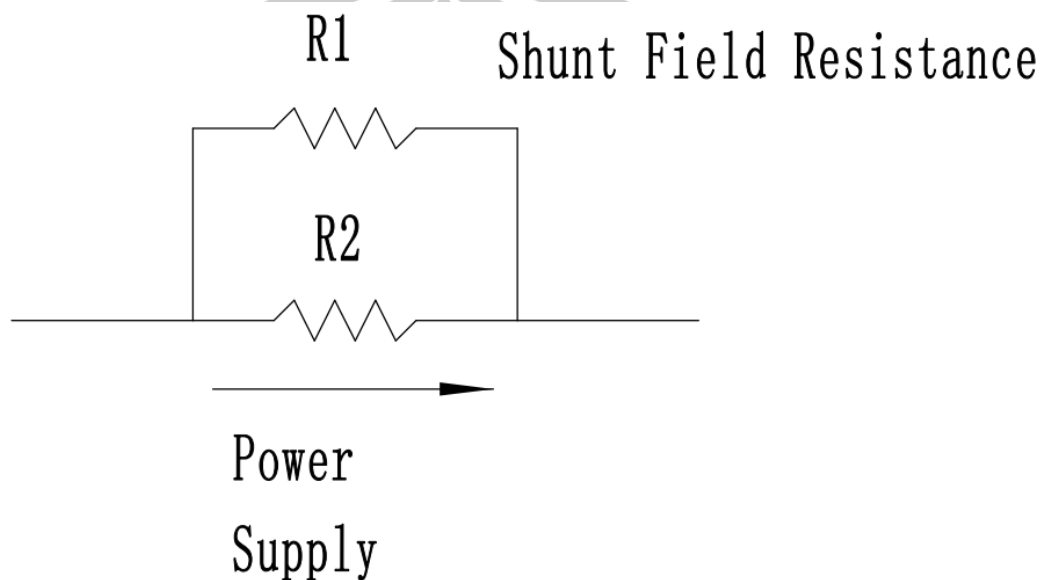


Figure 1 Splitter

The current monitoring scheme based on a shunt resistor utilizes the resistor to measure the current. This method is known for its high accuracy and small temperature drift. The current passing through the shunt can be calculated by measuring the voltage drop across its two ends. In electric vehicles, the operating current range typically falls between -500A and $+500\text{A}$. Therefore, the shunt's resistance value is usually chosen as $0.1\text{m}\Omega$, $0.15\text{m}\Omega$, or $0.25\text{m}\Omega$. With a resistance value of this magnitude, the voltage drop across the shunt at maximum operating current is limited to 50mV .

Using a shunt resistor for current sampling offers the advantage of ensuring full scale accuracy and achieving high overall accuracy compared to other methods. The most common solution for amplification and acquisition in the market involves using a chip with an internal integrated amplifier and ADC, such as the AS8510. This chip can be configured in software to adjust the amplification factor.

However, the use of shunt resistors has some drawbacks. Firstly, it generates high thermal losses, especially at high currents, which can reach up to 25 W . This places stringent demands on the thermal design of the board. The shunt resistor scheme

requires isolation devices to ensure safe isolation for low-voltage power supply and CAN signal transmission, despite its high cost. This scheme is widely adopted in the electric vehicle sector, including models such as Tesla's Model 3 and the AS8510 chip.

However, circuits with shunts in series have some limitations. Measuring large currents can result in significant energy loss and lack of electrical isolation capability. While isolated measurements can be achieved by adding isolated op-amps, this may introduce new measurement errors due to the drift and noise of the op-amps themselves [30], as well as increase power consumption and cost.

2.2.2 Hall sensor

A Hall sensor is a type of magnetic sensor that utilizes the Hall effect, which was first discovered by Edwin Hall in 1879. No changes in content have been made. The Hall effect occurs when a current (I) is passed through a thin rectangular conductor plate and a magnetic field (B) perpendicular to the direction of the current is applied. This results in the Lorentz force producing a potential difference (E) in a direction perpendicular to both the current and the magnetic field [31].

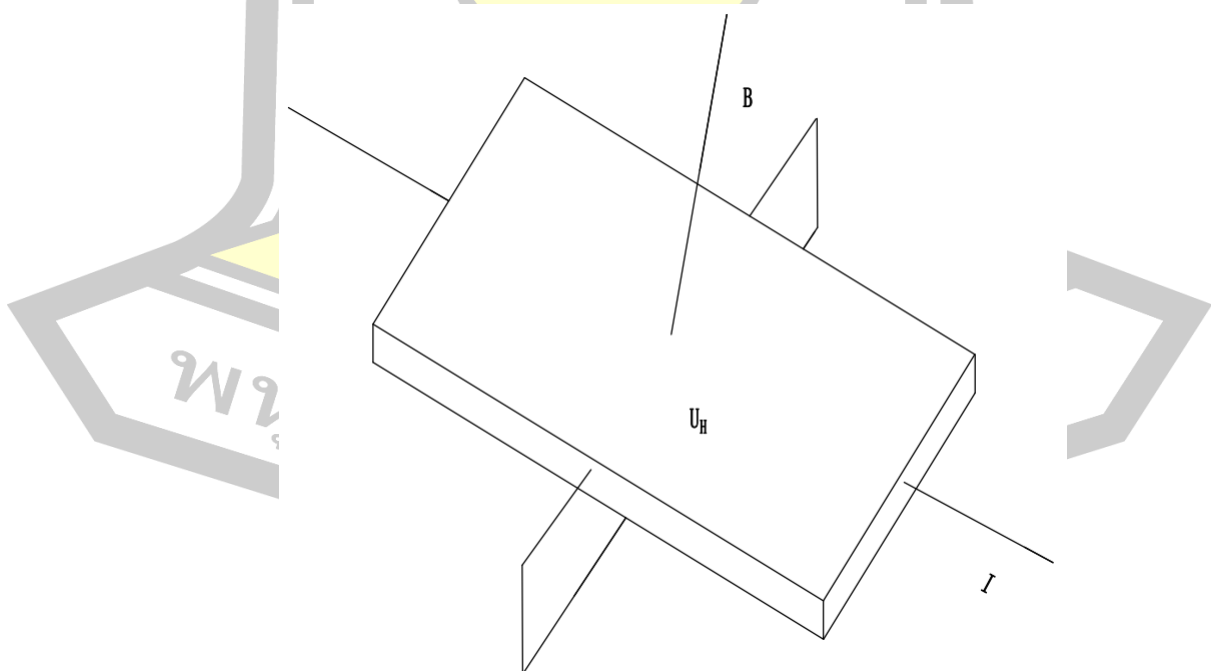


Figure 2 Principle of the Hall effect

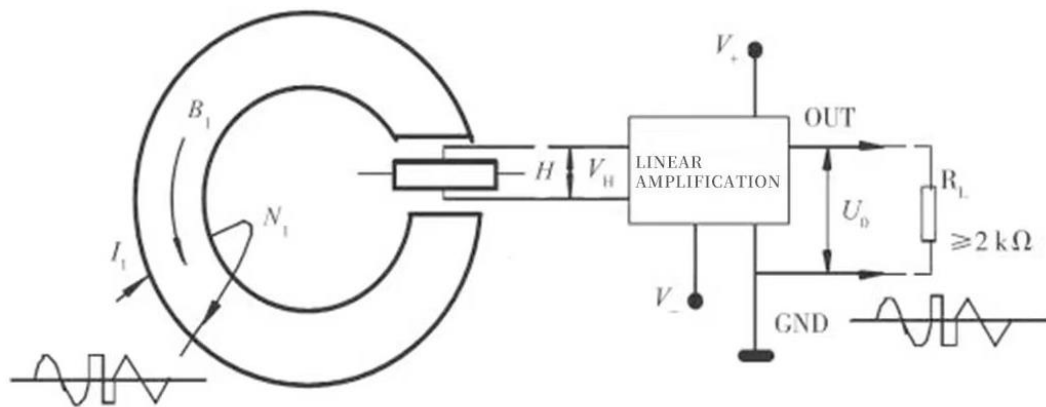


Figure 3 Principle of open-loop Hall sensors. [31]

Based on Ampere's law, a magnetic field strength B_1 is generated in the open toroid when a current flows through the primary winding of the N -turn coil. This magnetic field strength is proportional to the current. The magnetic sensor chip measures this magnetic field, generating a Hall voltage V . After linear amplification, V is converted into an output voltage signal U_o .

When the current measurement is zero, there is no magnetic flux in the open magnetic ring. This results in the output voltage of the magnetic chip being half of the supply voltage ($\frac{V_+}{2}$). However, when a current flows through the open magnetic ring, the magnetic chip detects a change in magnetic flux. This change is added to the zero-point voltage in the equation provided below, resulting in an output voltage that is proportional to the amount of flux change:

$$OUT = \frac{V_+}{2} + K\Delta V \quad (1)$$

The equation describes the relationship between the output voltage of the magnetic chip (OUT), the zero output voltage ($\frac{V_+}{2}$), the sensitivity of the magnetic chip (ΔV), which is the amount of voltage change caused by a unit change in magnetic flux, and the amplification (K) adjusted by an external resistor. Figure 1 shows that when the magnetic line of force passes perpendicularly through the front side of the magnetic-sensitive chip, the chip outputs a positive voltage change ($\Delta V > 0$). Conversely, when the magnetic line of force passes through the back side, the chip outputs a negative voltage change ($\Delta V < 0$).

HALL open loop current sensors usually have total accuracy errors within a few percentage points. They are appropriate for measuring a wide range of currents, from a few amperes to 30 kA, and can measure DC, AC, and complex current waveforms. These transducers are electrically insulated on both the primary and secondary sides,

Table 4 Advantages and disadvantages of open-loop Hall sensors ensuring no additional losses.

Advantages	Disadvantages
Low power consumption	Limited measurement bandwidth and response time
Small size and light weight	Large temperature drift
Low price	High-frequency currents, high eddy current losses

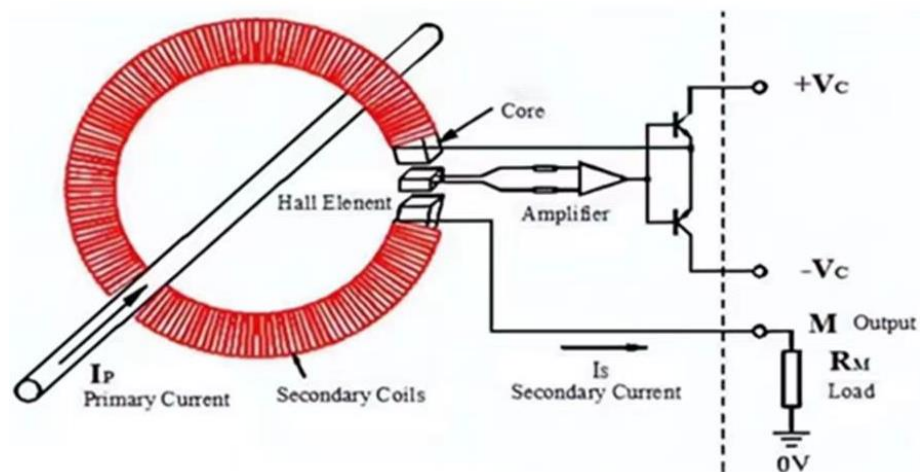


Figure 4 Principle of closed-loop Hall sensors. [32]

The HALL closed-loop current sensors are an improved version of the HALL open-loop current sensors. They use a compensation circuit to enhance their performance [32]. Hall current sensors operate on the magnetically balanced Hall principle, also known as the closed-loop principle. In this principle, the primary current (I_p) generates a magnetic flux that is concentrated in the magnetic circuit by a high-quality magnetic core. The Hall element is placed in the air gap to detect this flux. A multi-turn coil wound around the core outputs a reverse compensating current to cancel out the flux generated by the primary current, ensuring that the flux in the magnetic circuit is always zero. The sensor's output is processed through special circuitry to accurately reflect the change in the primary current as a current signal.

Advantages

Disadvantages

Very good accuracy and linearity	High current consumption
Low temperature drift	Large size, high cost
Fast response, large bandwidth	
High EMI immunity	

Table 5 Closed-loop Hall sensor advantages and disadvantages

Currently, HALL closed-loop current sensors typically have an error rate of less than 1% and can measure a range from a few amperes to 20 kA, with some optimized designs reaching up to 500 kA. To address issues with large temperature drift and low sensitivity in HALL sensing units, researchers are exploring the use of graphene-based HALL sensing units [33]. This sensing unit utilizes the properties of graphene material and is expected to achieve better performance in HALL sensing technology.

2.2.3 Fluxgate sensor

The fluxgate sensor was developed based on the fluxgate phenomenon. The first fluxgate patent was granted to H.P. Thomas in 1931 [34]. It is a device used for residual flux detection, employing a fluxgate sensor instead of a Hall element. It is commonly used for precision current measurement. The fluxgate sensing unit can measure DC or low-frequency AC magnetic fields in the range of $10^{-10} \sim 10^{-4}$ T. Fluxgate sensors can be classified as open-loop or closed-loop, depending on the direction difference between the excitation magnetic field and the external magnetic field. These two types of fluxgate sensors have different operating principles and application scenarios. The fluxgate sensors are classified into three categories: parallel type, orthogonal type, and hybrid type. Within the parallel type, they can be further subdivided into single rod, double rod, and ring types based on the structure of the magnetic core. This classification aids in understanding the various types of fluxgate sensors, their characteristics, and their applications [35].

A: Fluxgate sensor principle

The Flux Gate Principle is based on the fact that the inductance of a magnetic core that is easily saturated changes as the excitation current changes. This change in

inductance leads to a change in magnetic flux, which is similar to the process of opening and closing a door. This principle is imaginatively called the Flux Gate Principle. The figure shows the structure of a Flux Gate sensor unit. On a soft magnetic material core, two coils are typically wound: an excitation coil (primary coil) and a signal-sensing coil with N turns (secondary coil). The fluxgate sensor structure includes a magnetic core with a cross-sectional area of S , a permeability of μ , and is in a magnetic field with an ambient field strength of H_0 .

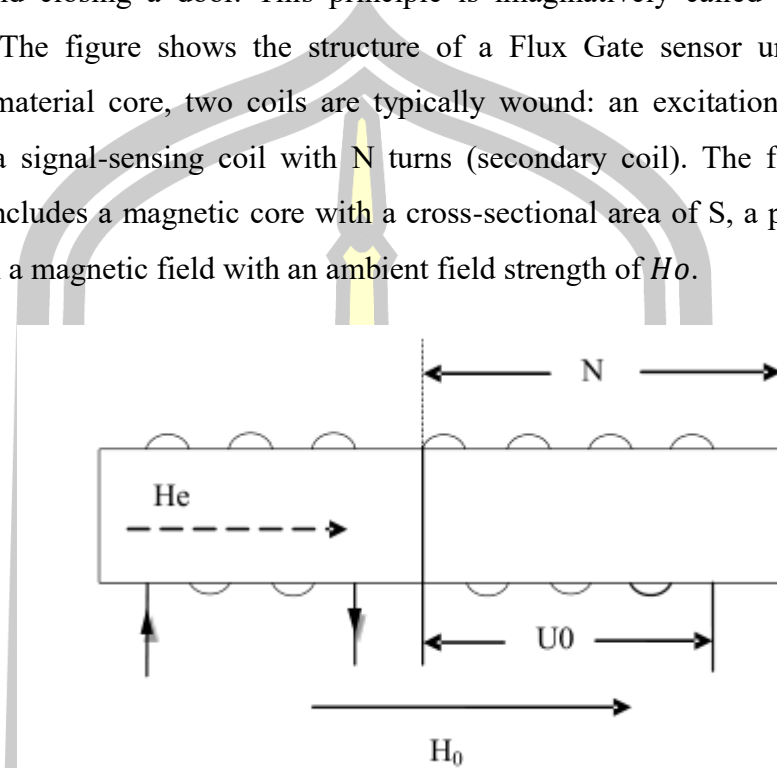


Figure 5 Fluxgate Sensor

When the current measured is zero ($I_p=0$), the core in the fluxgate sensor presents a complete excitation voltage signal. The excitation current flowing inside the coil is shown below.

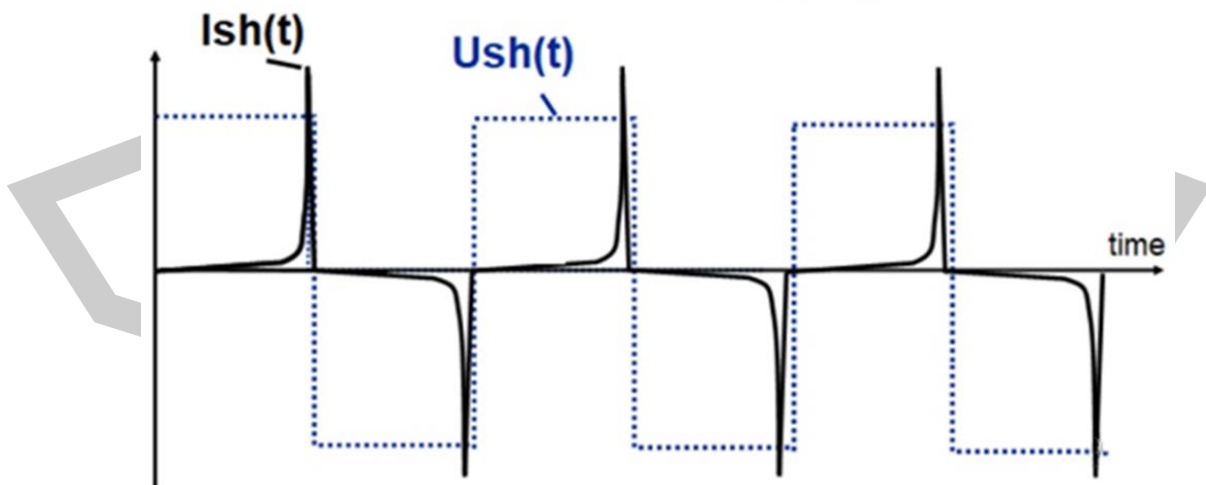


Figure 6 Core excitation voltage signal at $I_p=0$

When the current being measured is not equal to zero ($I_p \neq 0$, $I_p > 0$ in this figure), both the excitation current (I_{sh}) and the external current (I_p) act on the core

simultaneously. This results in an advance of the core saturation and a decrease in inductance. As a result, the current waveform is no longer symmetrical, and even-order harmonic currents are generated.

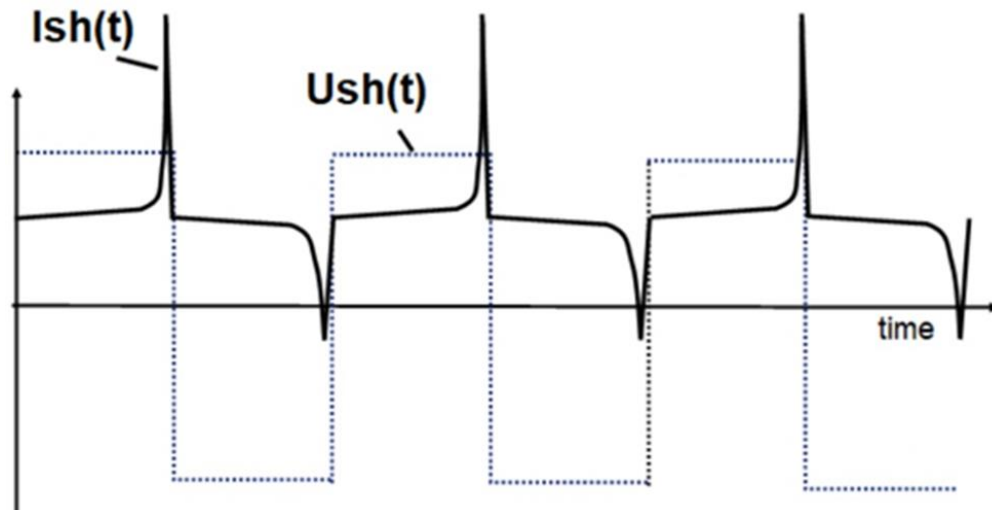


Figure 7 Core excitation voltage signal when $I_p \neq 0$

The magnitude of the measured current I_p determines its degree of asymmetry. By processing the waveform of the excitation current I_{sh} , we can obtain a voltage or current signal proportional to I_p , thus realizing the measurement of the I_p current. This is the principle of the open-loop fluxgate sensor.

If the second harmonic signal generated by the fluxgate excitation current is amplified and driven to the compensation coil so that the magnetic flux in the core and the flux caused by the primary current cancel each other and remain "zero", as shown in the figure below, this is called a closed-loop fluxgate current sensor.

B: Mathematical model of fluxgate sensor

The equation for generating the excitation magnetic field H_e can be obtained by applying a sinusoidal excitation current of angular frequency ω to the excitation coil.

$$H = H_m \sin(\omega t) \quad (2)$$

Where H_m denotes the amplitude of the excitation magnetic field strength.

From this, we can derive the magnetic induction strength B inside the core with the following equation:

$$B = \mu(H + H_m \sin(\omega t)) \quad (3)$$

The magnetic field described above generates an induced electromotive force, U , in the signal coil. The equation for this force is:

$$U = -N \frac{d\Phi}{dt} = -NS\mu A \left(\frac{dH}{dt} + H_m \omega \cos(\omega t) \right) \quad (4)$$

In the equation, N represents the number of coil turns, S represents the coil area, and A represents the number of coil windings. The magnetic core has a permeability curve as shown in the figure. When the amplitude of the excitation magnetic field strength H_m is smaller than the saturation magnetic field strength H of the core, the core is in the linear region of the magnetic permeability. At this point, the magnetic permeability μ remains constant. When the amplitude of the excitation magnetic field strength exceeds the saturation magnetic field strength H , the core will periodically switch between the linear and nonlinear regions of magnetic permeability. As a result, the magnetic permeability μ becomes a variable that changes with the magnitude of the magnetic field strength. Figure 8 shows a curve depicting the variation of magnetic induction with excitation magnetic field strength.

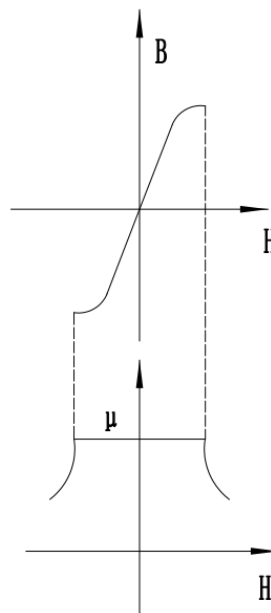


Figure 8 Variation curve of magnetic permeability μ

The magnetic permeability (μ) is a scalar quantity that varies with the excitation magnetic field strength (H_e) and has no positive or negative value. Therefore, when a core coil is excited using a polarized excitation field with an angular frequency of ω , μ can be regarded as a periodic signal with an angular frequency of 2ω and an even function. The Fourier series can be used to expand the varying permeability signal $\mu(t)$.

$$\mu = \mu_a + \sum \mu_i \cos(2i\omega t) \quad (5)$$

where μ_a is the DC component of the permeability and μ_i is the amplitude of each $2i$ harmonic component. Substituting Eq. (5) into Eq. (4) yields the following equation:

$$U = NSH\omega \sum 2\mu_i \sin(2i\omega t) + NSHm\omega \cos(\omega t) \sum 2\mu_i \cos(2i\omega t) \quad (6)$$

From the above formula, it can be clearly seen that for a single-core flux gate, the output induced electromotive force contains information about the measured ambient magnetic field H and the excitation magnetic field H_e . When the ambient magnetic field is zero ($H_o = 0$), the output induced electromotive force contains information about the excitation magnetic field H_e . When the ambient magnetic field is zero ($H_o = 0$), the induced electromotive force output contains only information about the excitation magnetic field H_e , so the output signal contains only odd harmonic components of the excitation signal frequency. When the environmental magnetic field is not zero ($H_o \neq 0$), the output induced electromotive force contains both the information of the excitation magnetic field H_e and the information of the measured magnetic field H_o . The information of the measured magnetic field H_o is reflected in the frequency domain as the even harmonic component of the excitation signal frequency. Therefore, by extracting the even harmonic component in the fluxgate output signal and measuring its amplitude, the intensity of the magnetic field H_o to be measured can be accurately measured.

2.3 MEMS fluxgate sensor

Nowadays, miniaturization research is crucial as devices tend to be miniaturized, placing higher demands on fluxgate sensors in terms of mass, volume, power consumption and integration [36]. Microelectromechanical systems (MEMS) processing technology provides technical support for this purpose. In recent years, the rapid development of semiconductor and microelectronic technologies has promoted MEMS-based fluxgate sensors. They have the advantages of low cost and easy mass production, making them the main direction for future sensor development in the field of current sensing.

In 1990, Seitz was the first to partially fabricate fluxgate structures using silicon micromachining technology, although at that time the technology was so limited that only thin cores and induction coils could be fabricated and the excitation coil could not be fabricated [37]. Subsequently, Kawahito et al. fabricated a thin core layer by an electroplating process and succeeded in fabricating the excitation and induction coils by a micromachining process [38]. In 2000, Chiesi first fabricated a miniature fluxgate sensor using a full CMOS process with a POMO alloy core, with a measurement range of $\pm 60 \mu\text{T}$, and with a current excitation of 17 mA, 125 kHz, the sensitivity reached 3760 V/T with a power consumption of 12.5 mW, a demagnetization error of 0.5%, and a nonlinear error equivalent magnetic field measurement error of $\pm 0.45 \mu\text{T}$, with an area of only 5.3 mm² and a thickness of only a few tens of micrometers [39].

With the continued maturation of the MEMS process, since 2010, researchers have focused on how to further reduce the size of miniature fluxgates and improve their sensitivity [40]. In 2014, Texas Instruments released a Foster-type MEMS fluxgate that could be integrated with a CMOS process for non-contact current sensing, and in 2016, Martijn F. Snoeij integrated a 250 V/T sensitivity fluxgate with a 500 kps readout circuit on a chip and used it for isolated current testing, requiring only 5.4 mW of excitation power, with a power efficiency 20 times that of existing techniques [41].

Due to its small size, low cost, high integration and high matching, MEMS technology is currently the hotspot of fluxgate miniaturization research. MEMS technology fluxgates have been widely used in many fields such as robotics, biomagnetic detection, aerospace and so on.

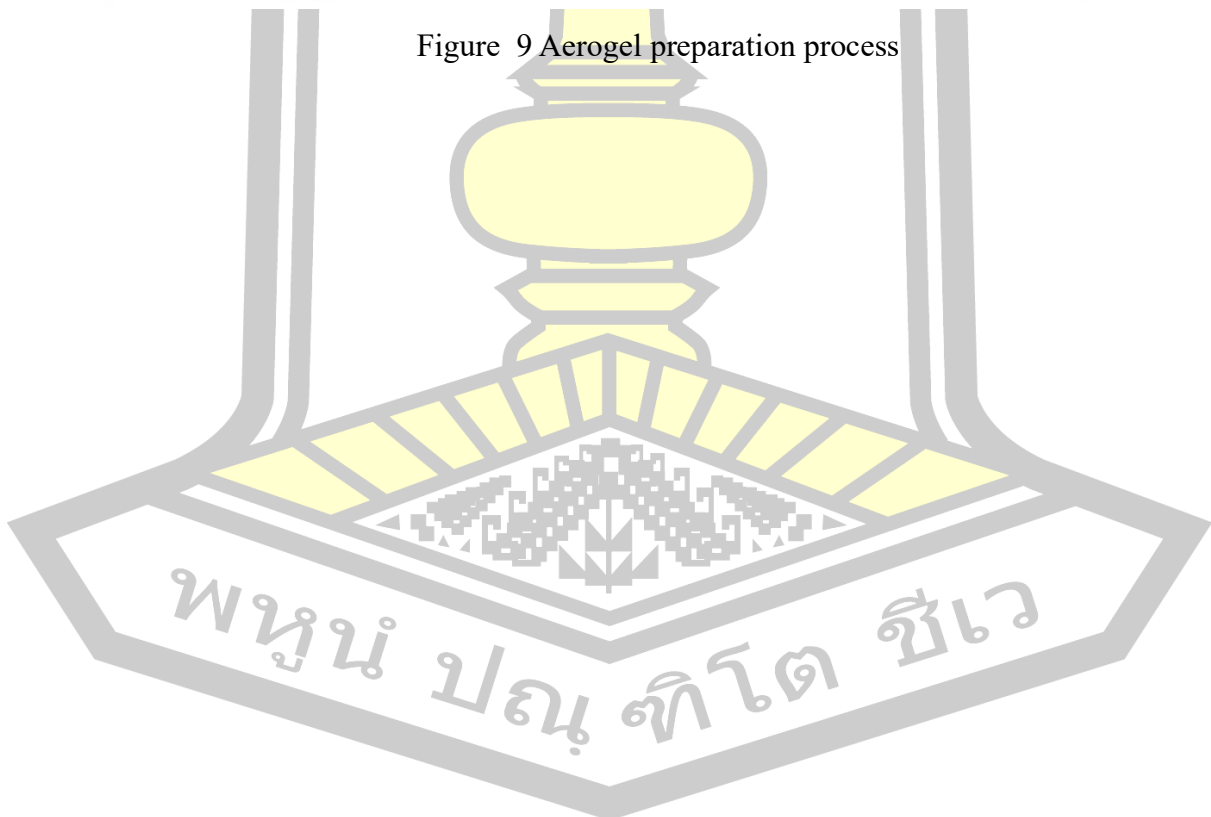
The study [42] investigated the temperature drift of the fluxgate sensor by subjecting the probe to a temperature range of -40 to 150 degrees Celsius. The results indicated that the main causes of the temperature drift were the thermal shift of the core hysteresis loop and the thermal expansion and contraction of the coil enameled wire with temperature. To wind the probe, it is recommended to use a low permeability core and high temperature enameled wire. Temperature drift can be compensated for using the least-squares method. As the charging pile is typically located outdoors, it is subject to natural factors such as seasonal changes and

temperature fluctuations ranging from several degrees below zero to 40 degrees Celsius. This can cause the temperature inside the box to rise when charging with a high-power charging cable, leading to a relatively large temperature difference experienced by the sensor and resulting in temperature drift. It is necessary to take certain measures to address this issue. Literature [43] analyzed the temperature characteristics of the output value of the fluxgate sensor and found that its accuracy is significantly affected by temperature. The study employed BP neural networks to identify the system and established a neural network for temperature compensation. The results indicate that the temperature compensation function is effective. According to literature [44], the coil constant of the sensor coil affects the temperature of the output of the instrument and, therefore, the accuracy of the system in the design of fluxgate magnetometers. Therefore, to improve the temperature characteristics of the balance test within a limited measurement temperature range, the instrument should be designed with a compensating reference source circuit that has a temperature compensation function. This will increase the cost of materials, production, and other expenses, and require a high level of consistency for the fluxgate sensor. The two aforementioned methods are unable to achieve long-term temperature equilibrium, despite their ability to improve sensor measurement accuracy. According to literature [45], SiO₂ aerogel composites possess excellent thermal insulation properties. In addition, [46] CN215297431U, 2021-12-24, draws on other sensor insulation approaches, utilizing aerogel composites to insulate the TMR chip and ensure accurate speed sensor measurement.

To sum up, it is an objective problem that the accuracy of the door sensor is affected by temperature. Airgel composites are inexpensive and manufacturable, making them a good solution to the deficiencies in the temperature characteristics of fluxgate sensors. This article will use the good thermal insulation properties of SiO₂ airgel composite materials to carry out structural design of the fluxgate sensor to improve the measurement accuracy, and compare and analyze the improvement effect of thermal insulation performance on the temperature characteristics of the fluxgate sensor through experiments.



Figure 9 Aerogel preparation process



Chapter 3 Research Methodology

3.1 Analysis of the Leakage Current Mechanism to Establish the Common Mode Equivalent Model of the Stack Circuit

Leakage current generation in a charging pile converter system is due to the presence of incomplete insulation in the circuit, which causes current to flow to ground through unintended paths. In order to gain a deeper understanding of this phenomenon, this paper focuses on the mechanism of leakage current generation in the charging electrical system of the charging pile converter by analyzing it in detail through the circuit model and mathematical relation equation.

In this paper, a common-mode equivalent model of the charging pile circuit is constructed, through which the path of common-mode current generation and the relationship between the common-mode voltage and the circuit structure parameters are analyzed in detail. The MATLAB simulation model is used to verify the system, and the fault current characteristics during normal operation and electric shock accident are simulated, respectively. We also investigated the effect of distributed power access on the fault current and the variability of fault current changes when the converter fails.

MATLAB has a rich toolbox and documentation to help researchers with power electronics simulation and analysis, and Simulink is a particularly powerful tool for modeling complex power electronics systems. In addition, MATLAB supports integration with other engineering tools and hardware, making it a powerful tool for power electronics engineers.

MATLAB is a powerful mathematical modeling and simulation tool that can also be used to simulate power electronic systems. The following are the general steps for performing power electronics simulation in MATLAB:

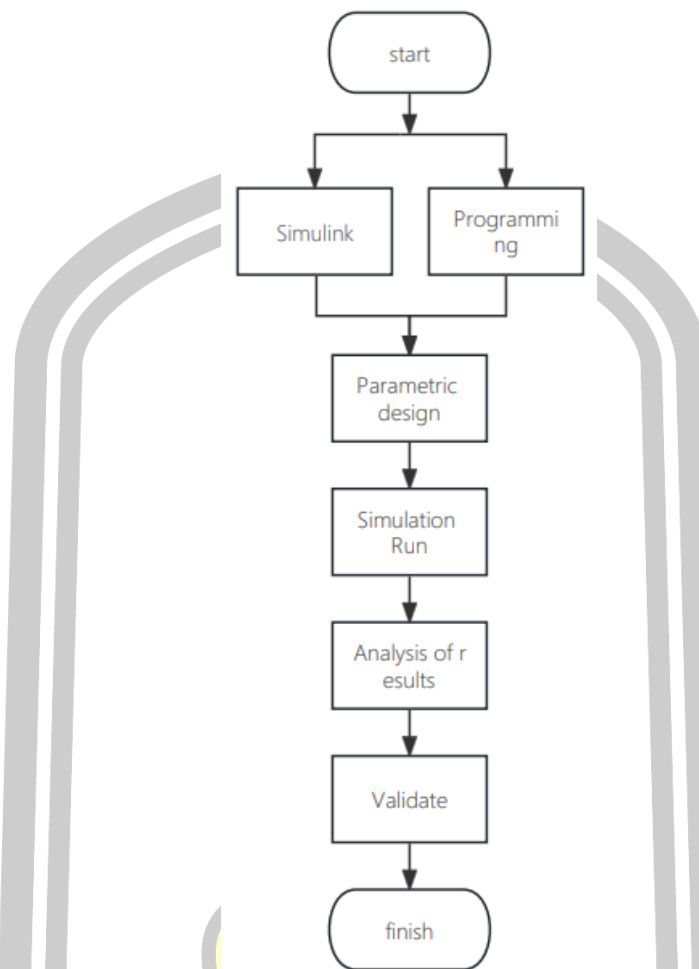


Figure 10 MATLAB simulation steps

First, a mathematical model of the power electronic system to be simulated in the DC non-isolated stack is created. This includes the parameters of the circuit components and the circuit topology. Use MATLAB to write a script to represent the power electronic system of the DC non-isolated battery stack. We can also use MATLAB's Simulink toolbox to create the system model and MATLAB scripts to describe the system equations. To run the simulation, this project requires setting up the initial conditions and parameters of the model. This includes the DC non-isolated charging pile supply voltage, load resistance, switching frequency, etc., run the MATLAB simulation and collect the data. MATLAB provides a number of different numerical solution methods to simulate the dynamic behavior of the system. The simulation results of the DC non-isolated charging stack are analyzed to evaluate the performance of the power electronic system. The behavior of the system can be understood by plotting waveforms, calculating spectral analysis, or performing other

analyses. Based on the simulation results, we can optimize and debug the system, including adjusting the control strategy, changing component parameters, or modifying the topology. Finally, we can validate the simulation results with real hardware to ensure that the simulation model matches the behavior of the real system.

Through the above analysis, this paper will clarify the path of leakage current generation, determine the optimal installation location of the sensor, and the overall system measurement scheme. These research results help to better understand the mechanism of leakage current in the charging pile converter system, and provide guidance and reference for solving the leakage current problem.

3.2 Temperature characterization of fluxgate sensors, insulation scheme design.

The temperature response of core magnetic characteristic parameters is investigated, and the fluxgate sensor temperature characteristics are described in detail. The effect of temperature on the hysteresis regression line is explored by establishing the Jiles-Atherton hysteresis model and solving it using the fourth-order Runge-Kutta method. Matlab was used for numerical simulation to output the hysteresis regression lines at different temperatures. The experimental results show that the temperature significantly affects the shape and characteristics of the hysteresis regression line, which in turn has an important impact on the accuracy of the current sensor.

Thermal simulation of fluxgate sensor with aerogel insulation material structure is carried out with the help of ANSYS software to simulate and analyze the dynamic hysteresis loop of fluxgate sensor. The following are the detailed steps, technical route for thermal simulation and analysis of magnetic fluxgate sensor with aerogel insulation structure using ANSYS software.

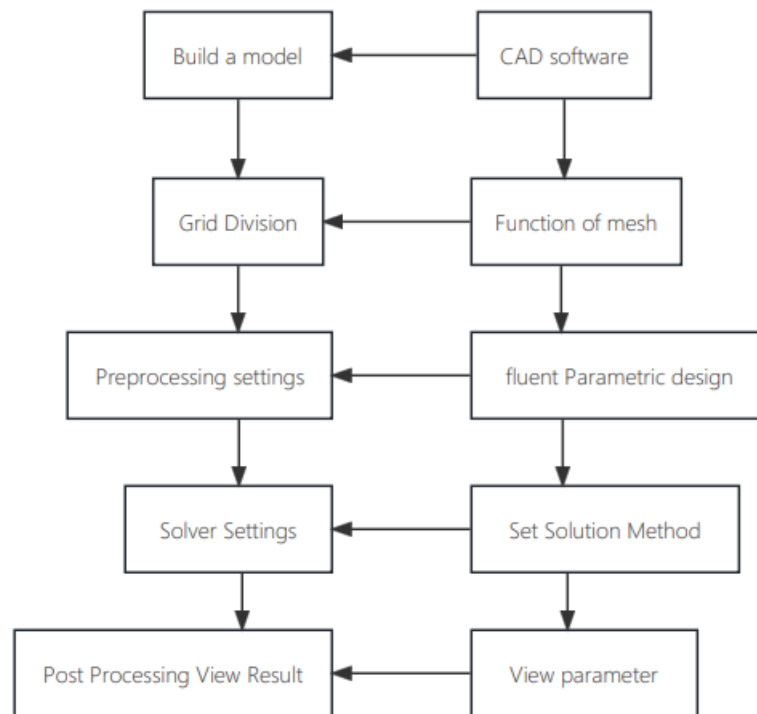


Figure 11 ANSYS thermal simulation steps

Thermal simulation of aerogel insulation materials in ANSYS is performed by importing the aerogel model into the engineering environment, defining material properties, meshing, setting boundary conditions, running the solver, and analyzing the simulation results through post-processing to simulate the thermal insulation properties of aerogels under different temperature conditions. This process allows engineers to gain a detailed understanding of the thermal conductivity behavior of aerogels, optimize designs, and verify the consistency of simulation results with actual experimental data, providing important information for the application and design of thermal insulation materials.

An experimental platform for sensor temperature characterization was established by obtaining a high and low temperature test chamber and other related equipment, which allows us to obtain the actual magnetic field value. On the experimental platform, we used the oscilloscope method to study the temperature effect of the dynamic hysteresis loop of the magnetic core material. By analyzing the experimental data, we obtained the temperature drift curves at different temperatures, from which we can clearly see the effect of temperature on the magnetic characteristic parameters of the magnetic core. Based on the SiO₂ aerogel composite material with

good thermal insulation performance, we design the thermal insulation structure for the magnetic fluxgate sensor, and obtain the data before and after thermal insulation through the constructed experimental platform, and analyze them comparatively.

Table 6 Equipment list for the construction of the experimental platform for sensor temperature characterization

serial number	installations
1	High temperature test chamber
2	Low Temperature Test Chamber
3	Sample Sensors
4	data acquisition
5	Oscilloscope or data logger

After setting up the experimental platform, make sure that the laboratory or test site is safe and ventilated for high and low temperature experiments. The following is the procedure for operating the fluxgate sensor temperature characterization experiment:

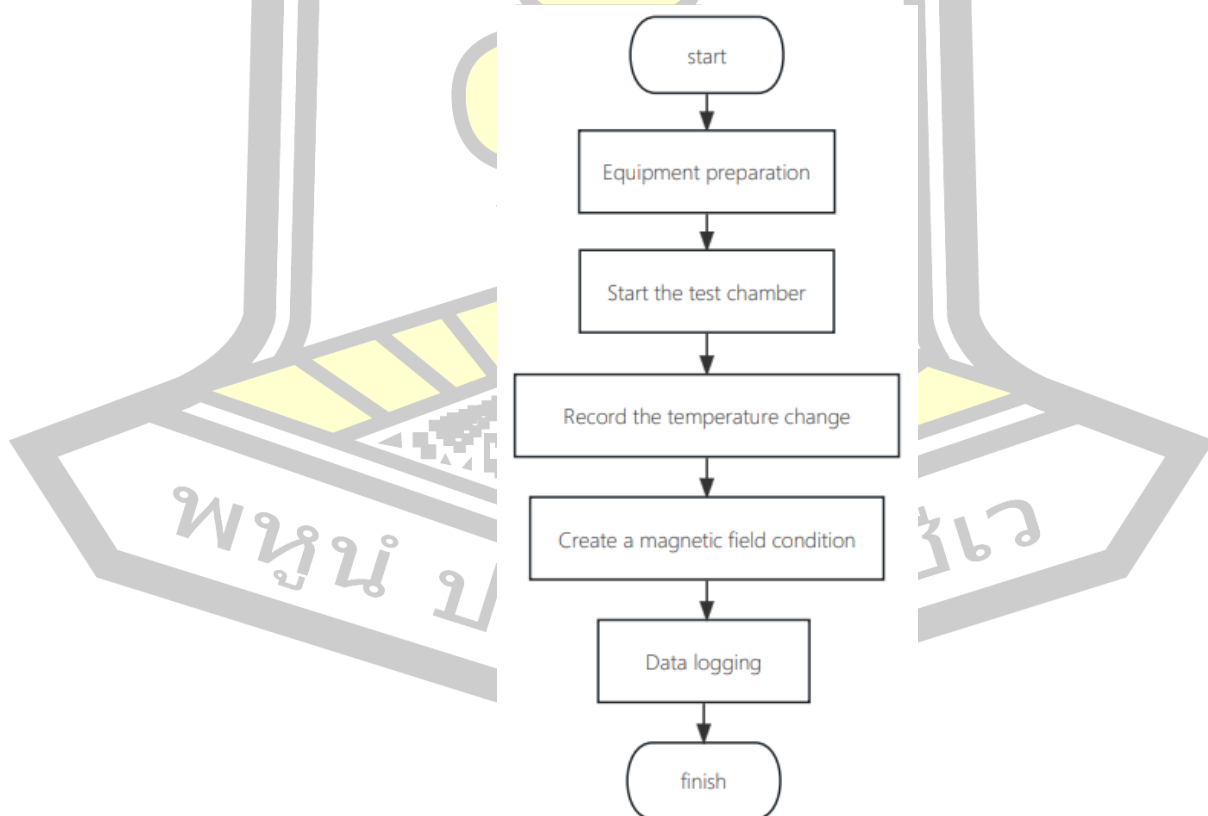
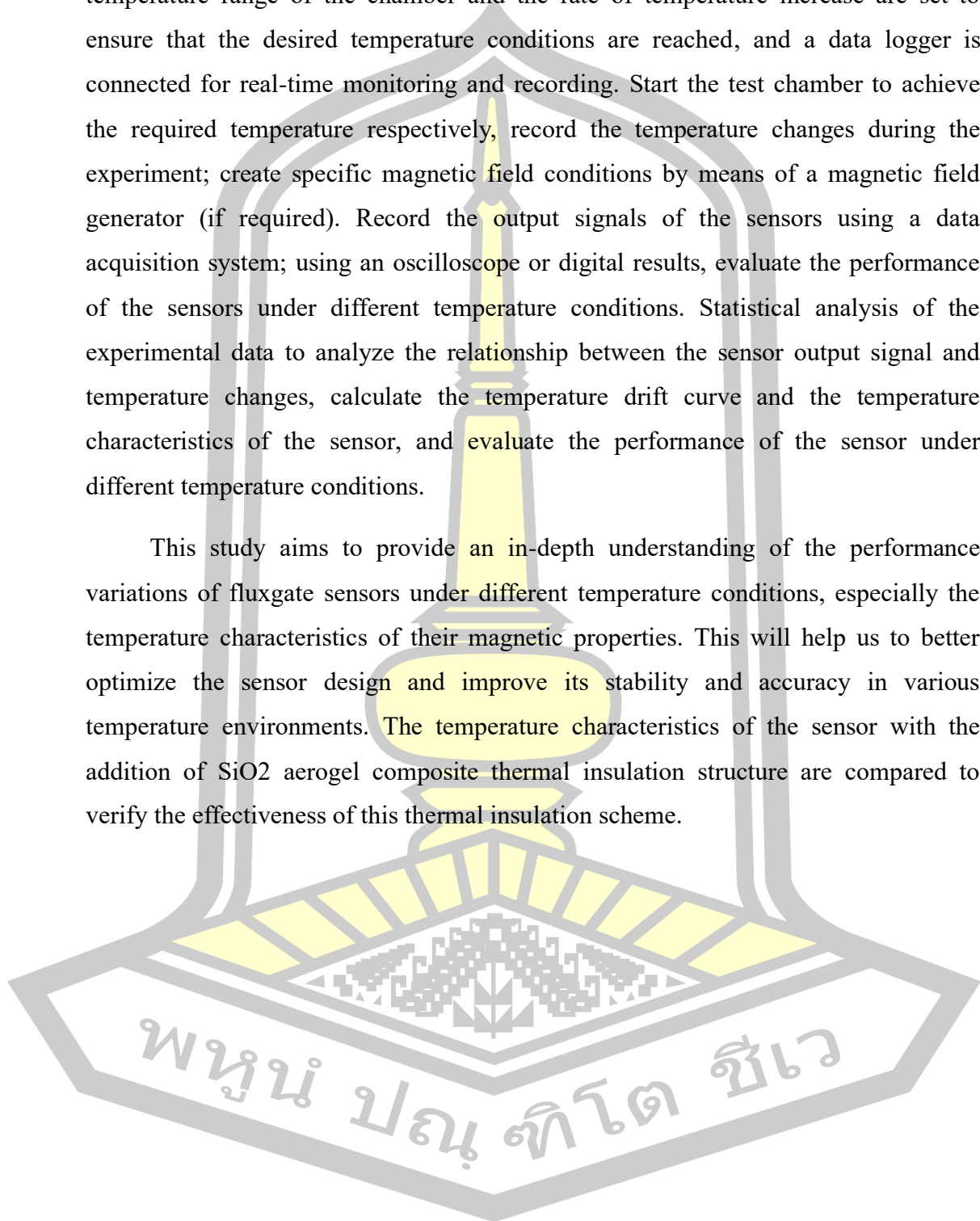


Figure 12 Temperature Characterization Experiment Procedure

Samples of the mounting sensors are placed in the test chamber, the temperature range of the chamber and the rate of temperature increase are set to ensure that the desired temperature conditions are reached, and a data logger is connected for real-time monitoring and recording. Start the test chamber to achieve the required temperature respectively, record the temperature changes during the experiment; create specific magnetic field conditions by means of a magnetic field generator (if required). Record the output signals of the sensors using a data acquisition system; using an oscilloscope or digital results, evaluate the performance of the sensors under different temperature conditions. Statistical analysis of the experimental data to analyze the relationship between the sensor output signal and temperature changes, calculate the temperature drift curve and the temperature characteristics of the sensor, and evaluate the performance of the sensor under different temperature conditions.

This study aims to provide an in-depth understanding of the performance variations of fluxgate sensors under different temperature conditions, especially the temperature characteristics of their magnetic properties. This will help us to better optimize the sensor design and improve its stability and accuracy in various temperature environments. The temperature characteristics of the sensor with the addition of SiO₂ aerogel composite thermal insulation structure are compared to verify the effectiveness of this thermal insulation scheme.



Chapter 4 Results and Discussions

4.1 Leakage analysis of DC charging station

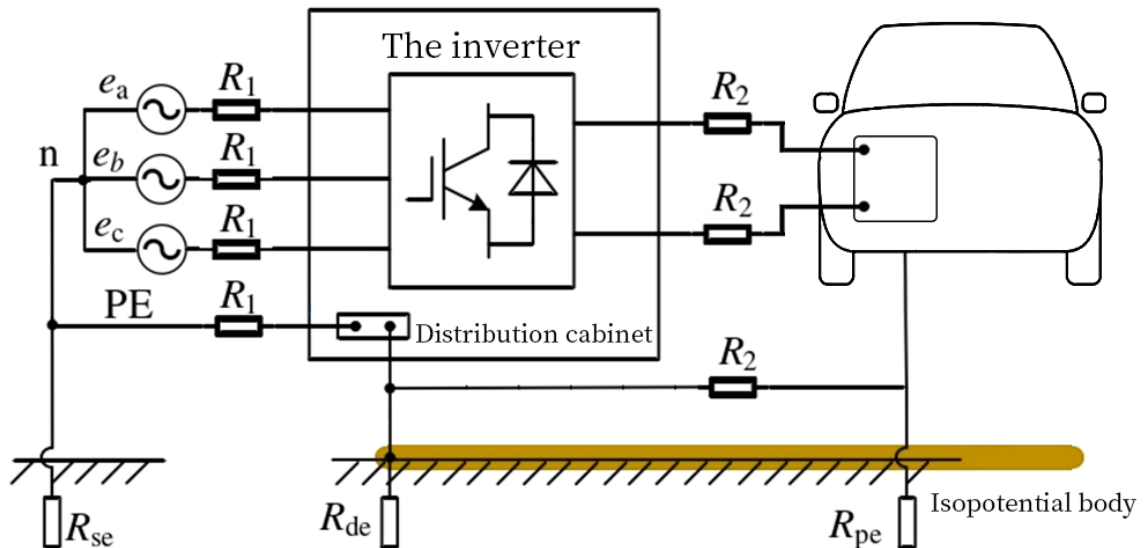


Figure 13 Schematic diagram of DC charging stations system [28]

As shown in the diagram, the DC charging pile system is mainly composed of AC side, converter and DC side. AC side: This is the input side of the charging pile, which is usually connected to the power grid or supply source. Here, AC power is supplied to the charging pile. Converter: One of the core parts of the charging pile, the converter is used to convert AC electrical energy into DC electrical energy so that the charging battery can accept it. DC Side: On this side, the converted DC power from the converter is transferred to the battery of the electric vehicle for charging. The basic principle of this system is to take AC energy from the grid and convert it into DC energy required by the electric vehicle battery through the converter, thus realizing the charging process.

Leakage currents can usually be categorized into several types, depending on the cause and path they take. Here are some common types of leakage currents:

Ground Leakage Current: This is the flow of current from a circuit to ground. Ground leakage current may be normal, but can cause problems when it exceeds equipment specifications or circuit design.

Common Mode Leakage Current: Common Mode Leakage Current is the current that flows through multiple conductors in a circuit, usually power and ground. It usually occurs between the power and ground lines and can cause problems such as electromagnetic interference.

Differential Mode Leakage Current: Differential mode leakage current is the current that flows between two conductors in a circuit. It is the opposite of common-mode leakage current and may be the result of unbalanced currents.

Cable Leakage: This occurs in cables or lines where current "leaks" out of the cable, possibly due to damage or aging of the cable.

Equipment Leakage Current: This is the leakage current generated by the appliance or equipment itself, which may be due to design defects, insulation failure or damage to the equipment.

4.1.1 Different earthing systems

Different grounding systems do have a significant impact on the safety and EMC of equipment. The three main earthing systems mentioned in your description (TT, TN, IT) are widely used in different countries and the IEC 60364 standard defines the installation and implementation of TT, TN and IT earthing systems. The three grounding systems have their own characteristics:

A. TT grounding system:

Application countries: mainly used in Japan, France, Italy, Egypt and other countries.

Features: The TT system is an earth-to-earth or ground-to-ground grounding system. This system provides a high level of safety by connecting equipment to ground with a separate ground.

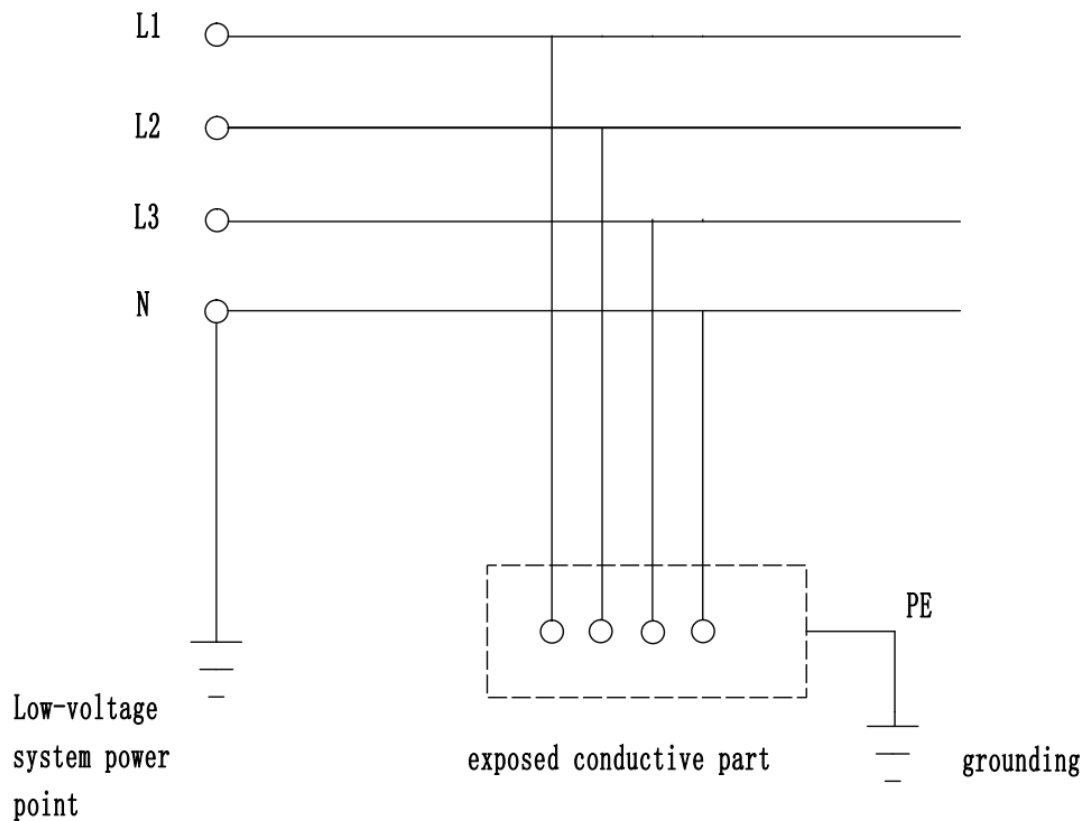


Figure 14 TT grounding system

B. TN grounding system:

Application countries: Widely used in China, the United States, the United Kingdom, Canada, Germany and other countries.

Characteristics: The TN system is an earth-neutral or ground-neutral grounding system. The earth of the equipment is realized by connecting to the neutral point of the power system. This system is designed for better electromagnetic compatibility and safety.

พหุ ประถมศึกษา

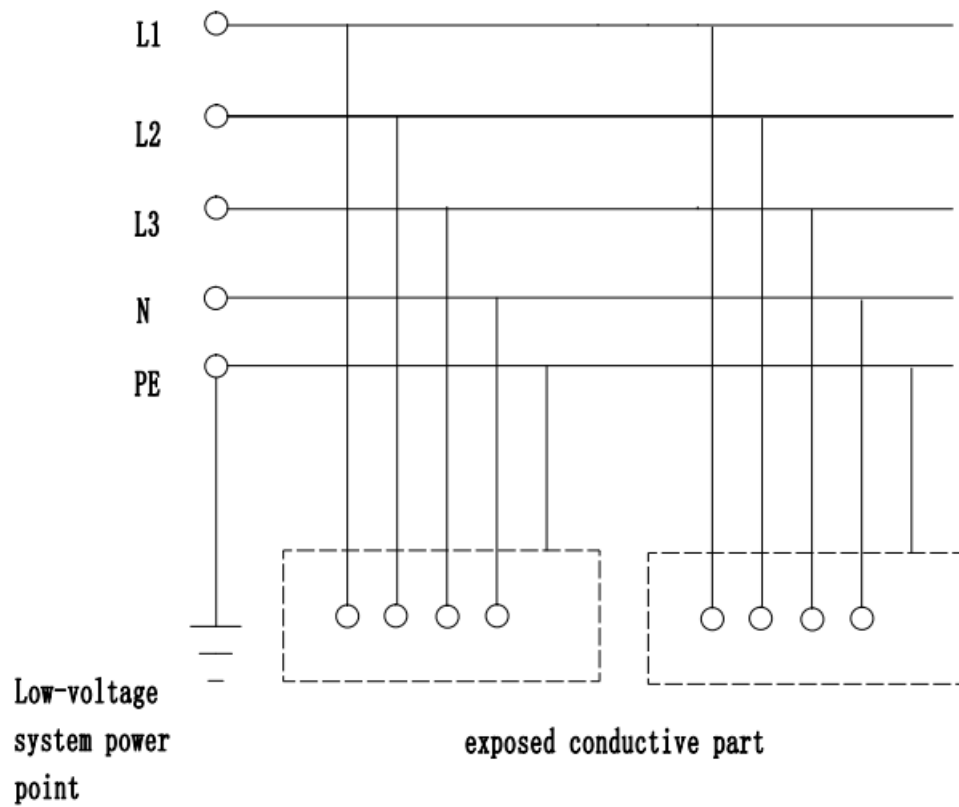
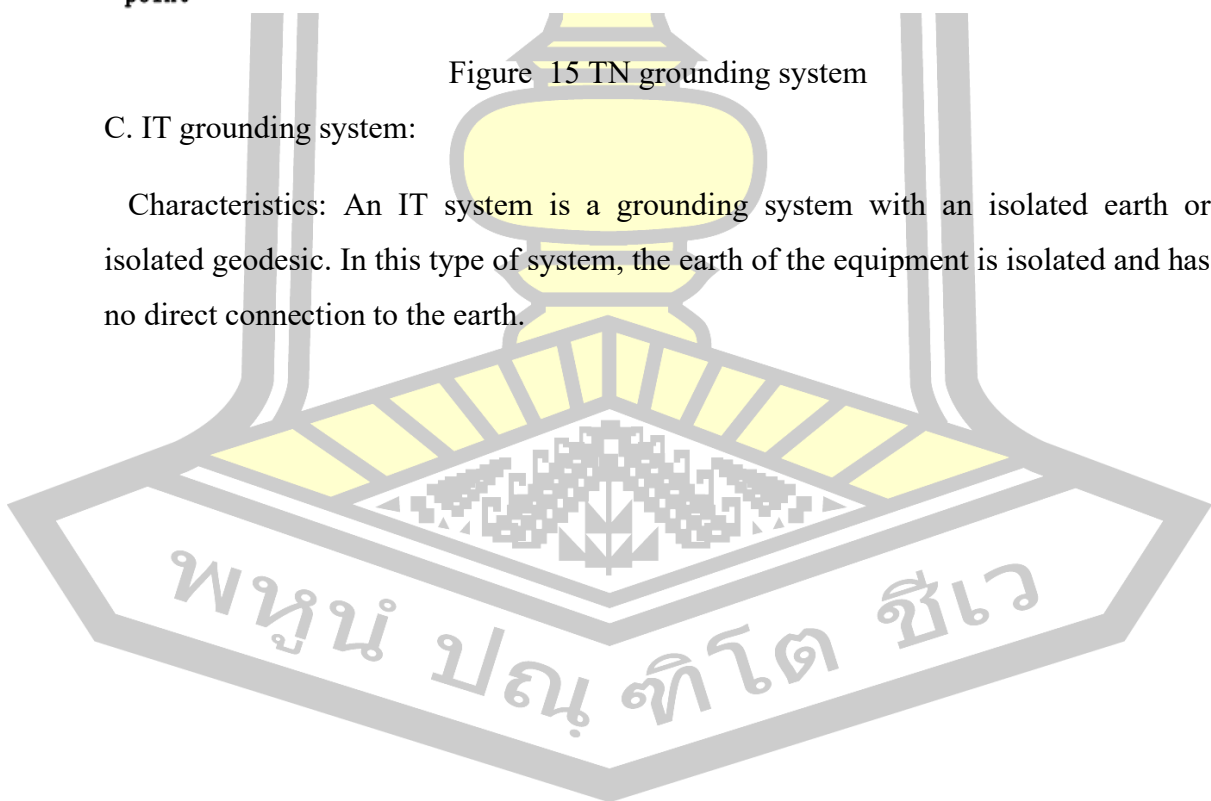


Figure 15 TN grounding system

C. IT grounding system:

Characteristics: An IT system is a grounding system with an isolated earth or isolated geodesic. In this type of system, the earth of the equipment is isolated and has no direct connection to the earth.



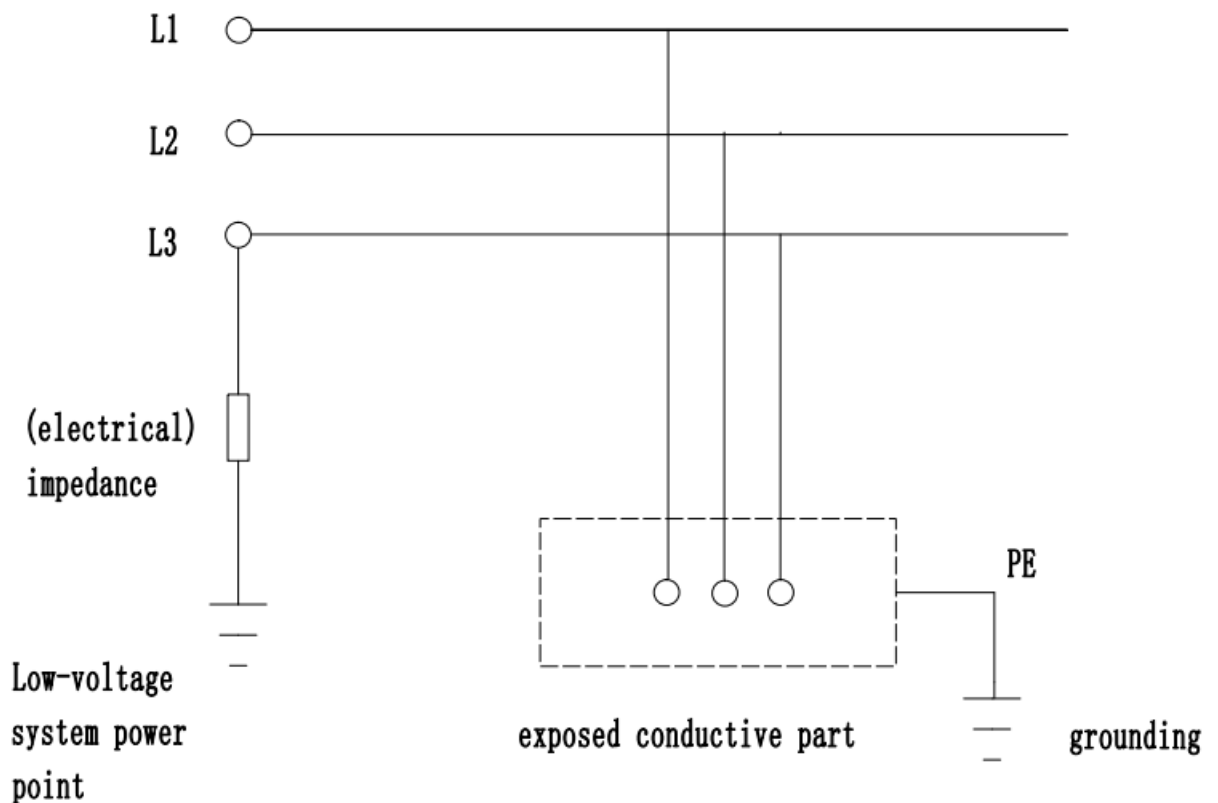


Figure 16 IT Grounding System

In addition, it is mentioned that in countries where full TN systems are dominant, TT grounding systems are also used when TN systems are not available. In DC buildings, the DC voltage is mostly rectified and converted from AC, and the DC side of the system is connected to the AC grid through a grid-connected converter for energy transfer and exchange, while the AC grid is mostly TN-grounded. In substations, the human body is ensured to be protected by connecting the protective earthing (PE) conductor with the lowest impedance, and most of the common-mode (CM) currents will flow through the PE conductor instead of the human body [48].

4.1.2 AC side leakage analysis

Charging station distribution systems are typically TN-S systems, a feature of such systems is a separate protective earth (PE) cable. However, when a ground fault occurs, it can lead to the generation of hazardous contact voltages.

In this case, the fault current is equal to the short-circuit current from the phase line to the PE cable. If the PE cable has the same dimensions as the phase cable, the

contact voltage (U_f) would exceed the safety voltage of 42.4 V specified in IEC 60950-1. This means that in the event of a fault, the human body may come into contact with the dangerous voltage and there is a risk of electric shock.

To minimize this risk, appropriate safety measures, such as the use of appropriately sized PE cables, suitable protective equipment and earthing systems, are usually required to ensure that the power supply can be cut off in time in the event of a fault and that the contact voltage is reduced to ensure personal safety. These measures help to prevent electric shock accidents.

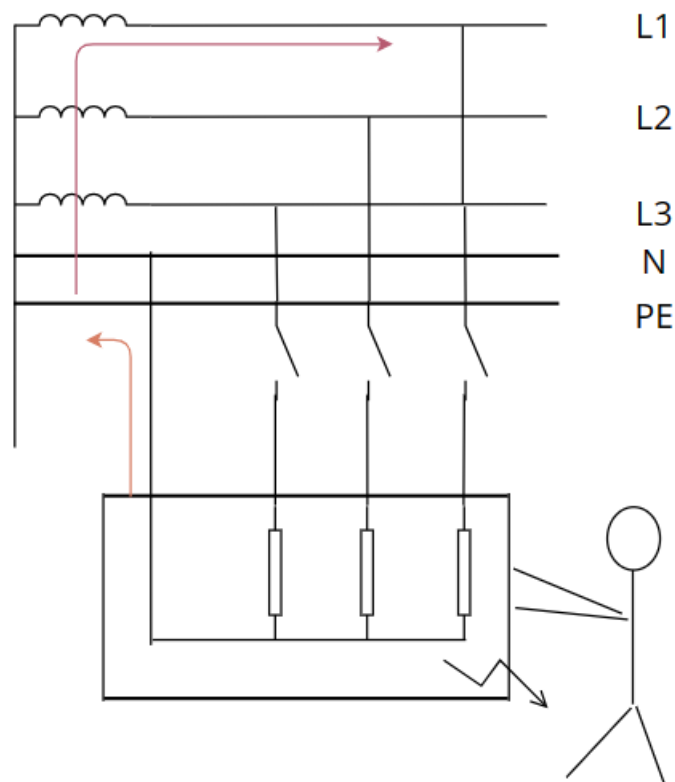


Figure 17 Schematic diagram of AC ground fault measurement
Short-circuit current in case of ground fault:

$$I_f = \frac{U_o}{R_{PE} + R_{ph}} \quad (7)$$

In Eq. $R_{PE} = \frac{\rho L}{S_{PE}}$, $R_{ph} = \frac{\rho L}{S_{ph}}$. such that $m = \frac{R_{ph}}{S_{PE}}$, the short-circuit current is

calculated as:

$$I_f = \frac{U_o \times S_{ph}}{[\rho \times (1+m) \times L]} \quad (8)$$

Where R_{PE} is the PE cable impedance, and S_{PE} is the cross-sectional area of PE cable, and R_{ph} is the phase line impedance, and S_{ph} is the cross-sectional area of the phase line.

The conditions for circuit breaker disconnection are $I_f > I_{mt}$, then the actual maximum cable length:

$$L_{max} = (U_o \times S_{ph} [\rho \times (1 + m) \times I_{mt}]) \quad (9)$$

Where I_{mt} is the instantaneous action tripping current of the circuit breaker. In practice, when the tripping conditions are not met, such as a ground fault that causes the short-circuit current to be less than the instantaneous tripping current of the circuit breaker, the tripping current setting can be reduced, and the RCD configured. these formulas can be used to determine short-circuit currents and the safety of the system in the event of a ground fault. If the short-circuit current exceeds the capacity of the circuit breaker, equipment damage or an electrical fire may result, so these calculations are critical to the design and safety of the electrical system.

When the human body is electrocuted, the human body current mainly consists of industrial frequency alternating current (AC), direct current (DC), and alternating current (AC) less than or equal to 1 kHz. f_s AC currents (including low-frequency currents less than or equal to 1 kHz and medium-frequency currents from 1 kHz to f_s). In addition to DC and I.C., AC currents less than or equal to f_s AC currents less than or equal to may also cause electric shock injury to humans. Referring to the standard IEC 60479-2-2019, the relationship between different frequencies of AC and the threshold for ventricular fibrillation in humans is shown in Table 1, where the value of the current required to produce a ventricular fibrillation response increases significantly with increasing frequency, especially at frequencies greater than 1 kHz.

In a TN grounding system, the lowest impedance protective earth (PE) conductor is the key element used to return leakage current to ground. In the event of a leakage on the AC side, the leakage current creates a return path through the PE conductor rather than through other equipment or the human body. This is a design intended to ensure personal safety and proper equipment operation.

In a TN grounding system, a PE conductor is connected between the equipment's neutral and earth. When a leakage occurs in the equipment, the leakage current will flow back to earth through the PE conductor. The PE conductor is designed to provide a low impedance path so that the leakage current can leave the equipment quickly and safely, minimizing potential hazards to humans and other equipment.

Overall, in a TN grounding system, the PE conductor is present to effectively manage and handle leakage situations to ensure the safety and stability of the system.

4.1.3 DC side leakage analysis

Common mode voltage and leakage current will exhibit different characteristics under different grounding methods. The following are the effects under different grounding methods:

A. Ungrounded or high-resistance grounding:

Common mode voltage: In this case, the common mode voltage is usually large. Since the DC side is not grounded or the grounding impedance is very high, the common-mode voltage cannot be effectively suppressed, and thus a large common-mode voltage occurs.

Leakage current: The DC side has only stray capacitance to ground and there is no DC reference bus to establish a balance point. As a result, even small leakage currents can lead to unpredictable voltage excursions, which may adversely affect the normal operation of the system.

B. The DC side is directly grounded:

Common Mode Voltage: In this case, the DC side forms a common mode path to ground, so the common mode voltage will usually be relatively small. Grounding can effectively suppress the increase in common mode voltage.

Leakage Current: The common mode path formed with ground results in a larger current to ground, which means that the system will have more leakage currents flowing to ground, but due to grounding, these leakage currents do not result in a large voltage offset.

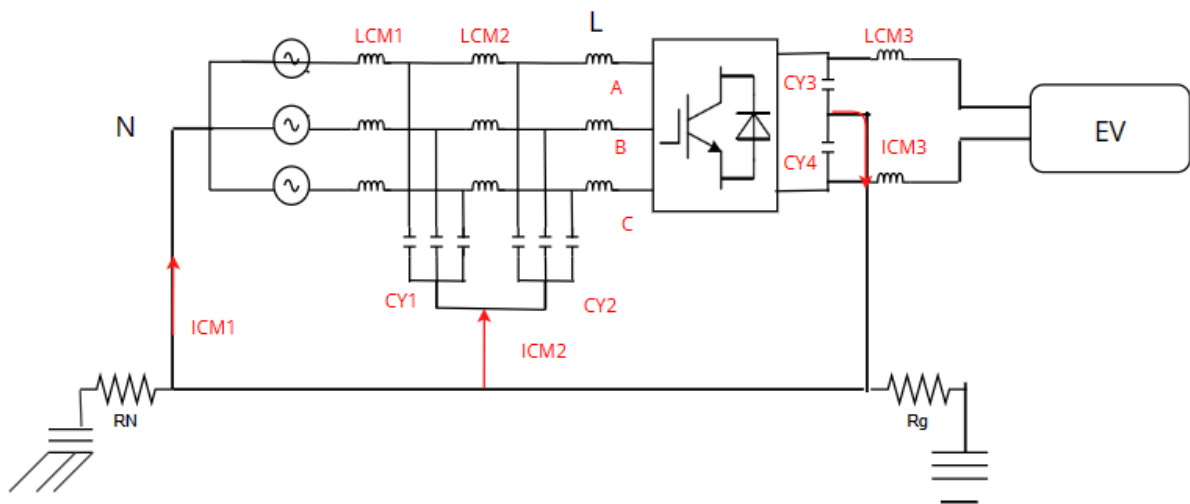


Figure 18 Schematic of common mode current

Due to the low impedance CM ring formed by the AC and Y capacitors, the CM voltage source (V_c) will introduce large common mode leakage current during normal operation. The common-mode voltage is mainly generated by the AC/DC converter, and the common-mode voltage forms a leakage current in the distribution capacitors and the equipment Y capacitors. In TN grounding system, its total CM leakage current (I_{CM}) has two paths to return to its source: one goes through the AC side capacitors (I_{CM_AC}); and the other goes through the protective earth (PE) conductor or the earth ground (IGND).

พหุ ประถมศึกษา ชีวะ

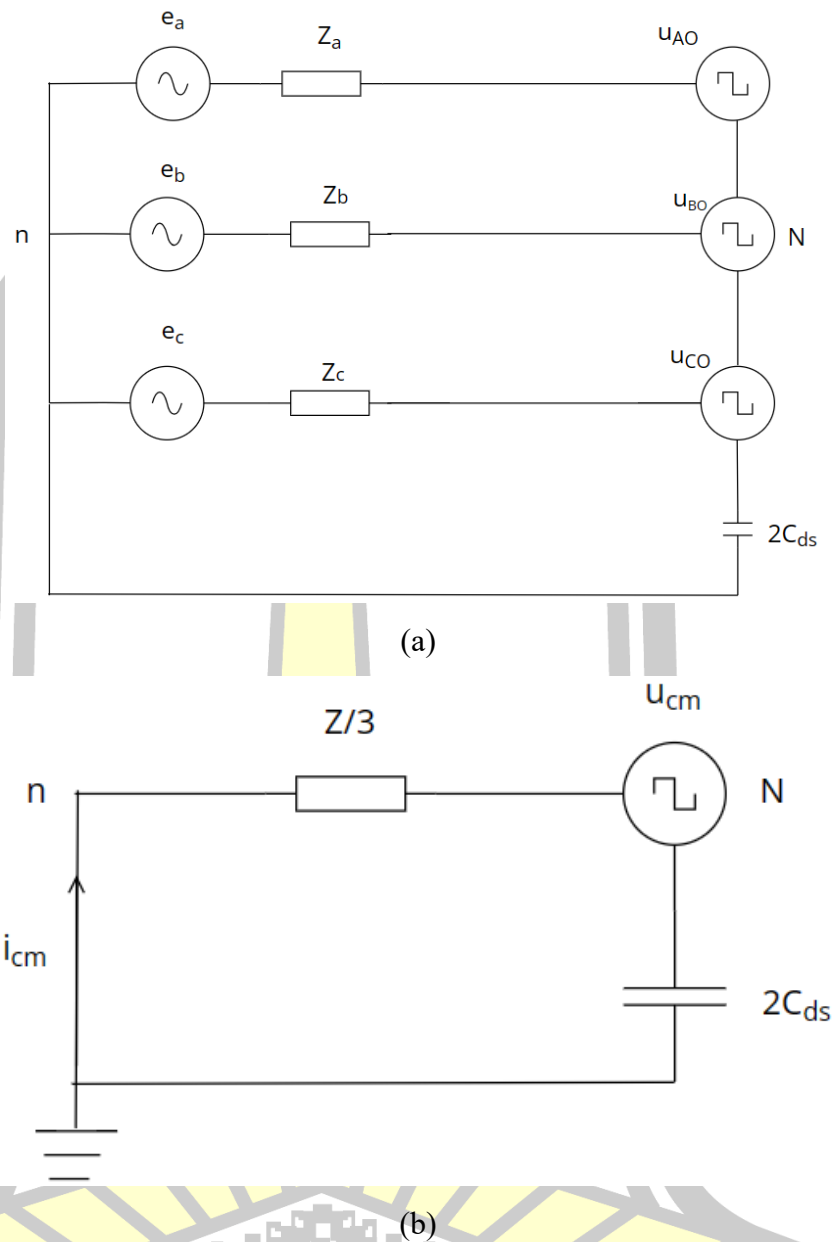


Figure 19 Simplified diagram of common mode circuit

A three-phase system generally ensures that the three-phase parameters are balanced (i.e., $Z_a = Z_b = Z_c = Z$), then the common mode voltage converted from differential mode.

u_{dcm} It can be neglected that the grid voltage does not generate leakage current when the three phases are balanced, and finally the common mode voltage expression is obtained as shown in (10).

$$u_{cm} = \frac{u_{AO} + u_{BO} + u_{CO}}{3} \quad (10)$$

According to the equivalent model of grid-connected converter for three-phase system, the leakage current flowing through the distributed capacitance of the system to the ground and the voltage at the two ends of the distributed capacitance are shown in Equation (11). It can be seen that there are two factors affecting the system leakage current: the common-mode voltage generated by the converter and the system common-mode loop impedance.

$$i_{cm} = 2C_{ds} \frac{du_{c ds}}{dt}$$

$$U_{c ds} = u_{cm} - i_{cm} \left(\frac{z}{3} \right) \tag{11}$$

With good insulation, the simplified path of the common mode current is shown in Fig.

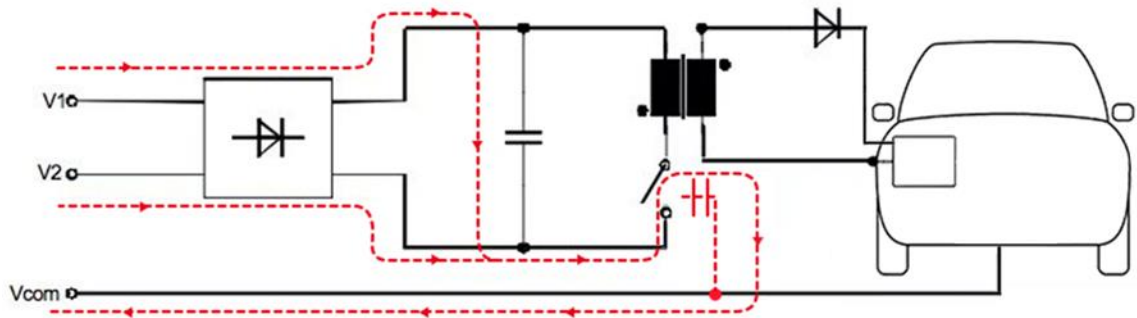


Figure 20 Simplified path of common mode current

According to the above analysis, the leakage current distribution of DC non-isolated charging pile system is summarized as follows:

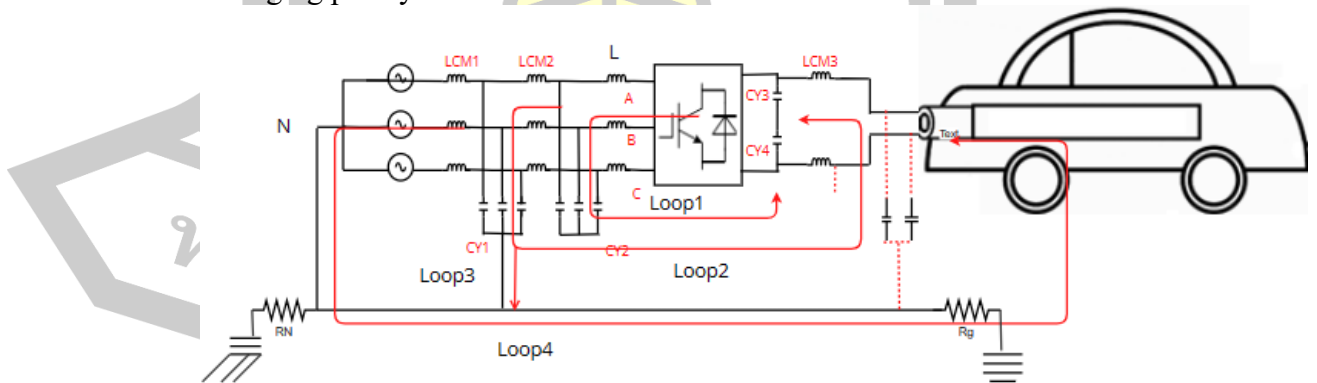


Figure 21 System leakage current distribution

The common-mode leakage current loop shown in Figure 4 employs a series of filters to control the propagation of the leakage current. The following are the roles and characteristics of the loops in the figure:

a. Loop 1 (common mode filter):

This is a common mode filter used to filter out high frequency common mode current components. Common mode filters typically include inductive and capacitive elements that block high frequency currents from passing through while allowing DC and low frequency currents to pass through. In this case, the high-frequency leakage current is filtered and prevented from going to the next stage.

b. Loop 2 (LC filter):

An LC filter is another circuit used for filtering that further filters out high-frequency common mode currents. It consists of an inductive element (usually a coil) and a capacitive element for filtering high frequency noise.

c. Loop 3 (distributed capacitance to ground):

This part of the circuit is mainly used to transmit low and medium frequency leakage currents. By distributing capacitance to ground, low and medium frequency leakage currents can be transmitted to ground without much effect on the system.

d. Loop 4 (earth):

This portion of the circuit transmits low and medium frequency leakage currents to earth, releasing the current into the ground. In this way, the system effectively directs the leakage current into the ground, ensuring that the current does not pose a hazard or interfere with the system.

These circuits work together to ensure that high frequency leakage currents are filtered and circulated within the system, while low and medium frequency leakage currents are directed to the ground, thereby protecting the system and improving safety. This design helps minimize the impact on the Residual Current Circuit Breaker (RCD), allowing it to more accurately detect potential leakage problems.

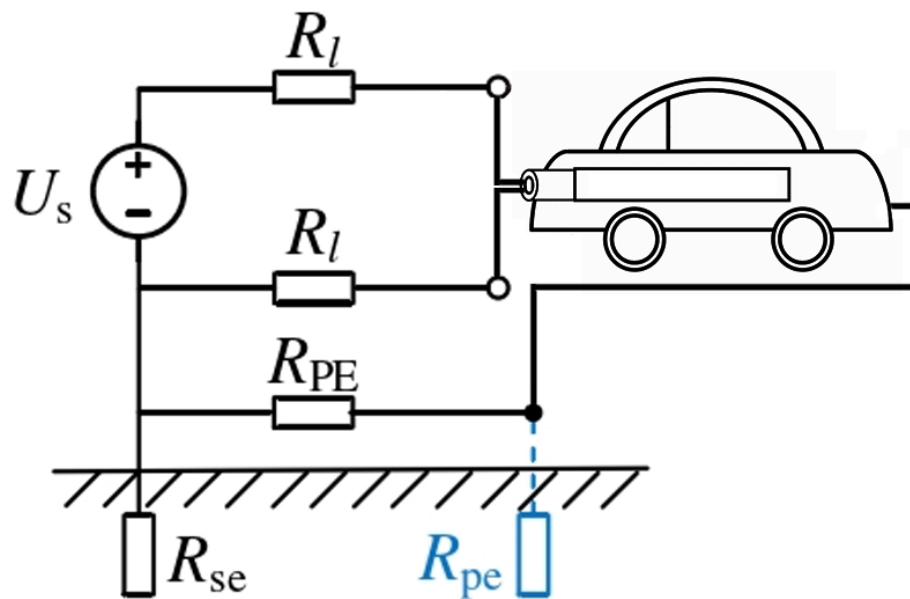


Figure 22 Equivalent Circuit Diagram for Zero Protection

Without repeated grounding resistance, when a single fault occurs in the system, the fault current will circulate directly in the PE wire (protective grounding cable), directing the fault current back to ground, and the voltage to ground of the equipment enclosure will be affected by the line impedance voltage divider, thus ensuring the safety of the equipment. To summarize, the zero protection can reduce the voltage of the equipment shell to ground, increase the fault current, so that it is easier to trigger the overcurrent protection, so as to cut off the power supply in time to ensure the safety of the system.

$$U = \frac{U_s}{R_{PE} + R_l + R_g} \times R_{PE} \leq \frac{2U_s}{3}$$

$$I_d = \frac{U_s}{R_{PE} + R_l + R_g}$$

(12)

The result of simulation through MATLAB is shown in Fig. 23:

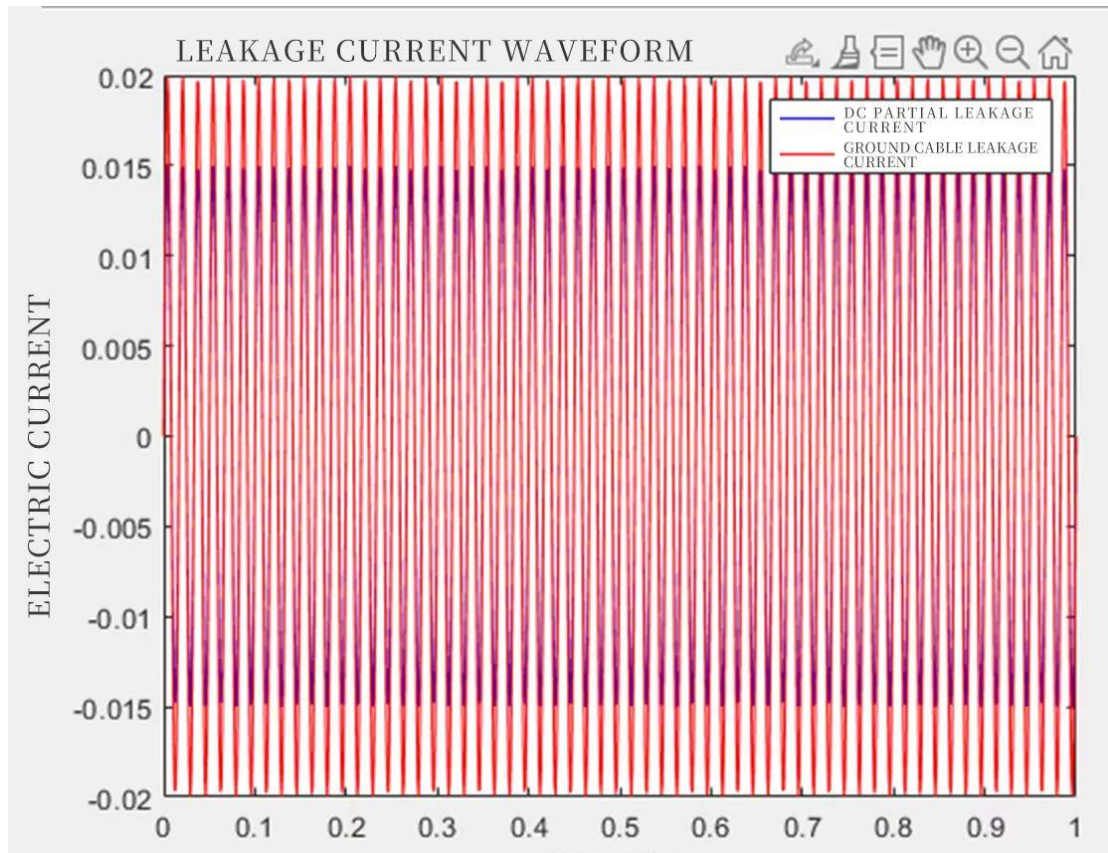


Figure 23 Leakage current simulation schematic

The red color is PE wire leakage current and the purple color is DC cable leakage current, obviously the PE wire leakage current is higher than the DC cable current.

In a non-isolated low-voltage DC power supply system, leakage currents are generated during normal operation which may be residual currents or caused by faults in the system. These fault currents may be AC, DC or a combination thereof. Since the PE wire is the lowest impedance conductor connected to ground, it is the main return path for leakage currents and can increase fault currents. Fluxgate sensors can detect both DC and AC currents. By installing a fluxgate sensor on the PE line, the system can detect leakage currents and, due to the low impedance characteristics of the PE line, fault currents are more likely to trigger overcurrent protection. This helps to cut off the power supply in time, ensuring the safety of the system against potential damage or danger.

Overall, the installation of fluxgate sensors on PE lines is an effective means of monitoring and protection in non-isolated low-voltage DC supply systems, ensuring

that the system is able to take timely and appropriate action in the event of leakage currents.

4.2 Sensor Temperature Characterization Study

4.2.1 Temperature Drift Study

Fluxgate sensors typically consist of two main parts: a magnetic probe and a circuitry section. The magnetic probe is responsible for sensing changes in the external magnetic field, while the circuitry section processes and amplifies these signals and converts them into a useful voltage or current output.

An important point in the performance evaluation and temperature characterization of fluxgate sensors is to understand the behavior of the magnetic probe at different temperatures, especially over a wide temperature range. The temperature drift of a magnetic probe is the variation of its output signal at different temperatures. In order to investigate this phenomenon, a series of experiments are required, which include subjecting the magnetic probe to different temperature environments and recording its output signal.

Tests were conducted by subjecting the magnetic probe to temperatures ranging from 0°C to 60°C and recording its temperature characteristic curve over this wide temperature range. The temperature characteristic curve shows that the relationship between the output of the magnetic probe and temperature is approximately proportional linear, meaning that the output signal of the magnetic probe changes in approximately the same proportion as the temperature changes. Understanding the temperature drift characteristics of a magnetic probe at different temperatures is important for calibrating and compensating for its performance in real-world applications where temperature variations can lead to errors. By understanding the temperature characteristics of the magnetic probe, this experiment takes the measure of SiO₂ aerogel to minimize the temperature-induced effects, thus improving the accuracy and reliability of the fluxgate sensor.

The objective of this test was to investigate the variation of the output voltage of the fluxgate sensor at different temperatures. The test procedure is as follows:

Initial temperature: The temperature chamber is set to 0°C. Start recording data: Start the chamber, gradually increase the temperature from 0°C to 60°C, and gradually decrease the temperature from 60°C to 0°C to complete a cycle.

Data Acquisition Process: At each temperature point, the actual output voltage value corresponding to each magnetic probe is collected. It should be noted that since all magnetic probes are placed in slightly different locations, their output voltage values will vary. However, in this test, the focus is on the amount of change in the output voltage as the temperature changes, rather than the absolute value.

Based on the experimental data, a graph of the variation curve of the output voltage of the fluxgate sensor at different temperatures can be plotted to analyze the effect of temperature on the performance of the sensor.

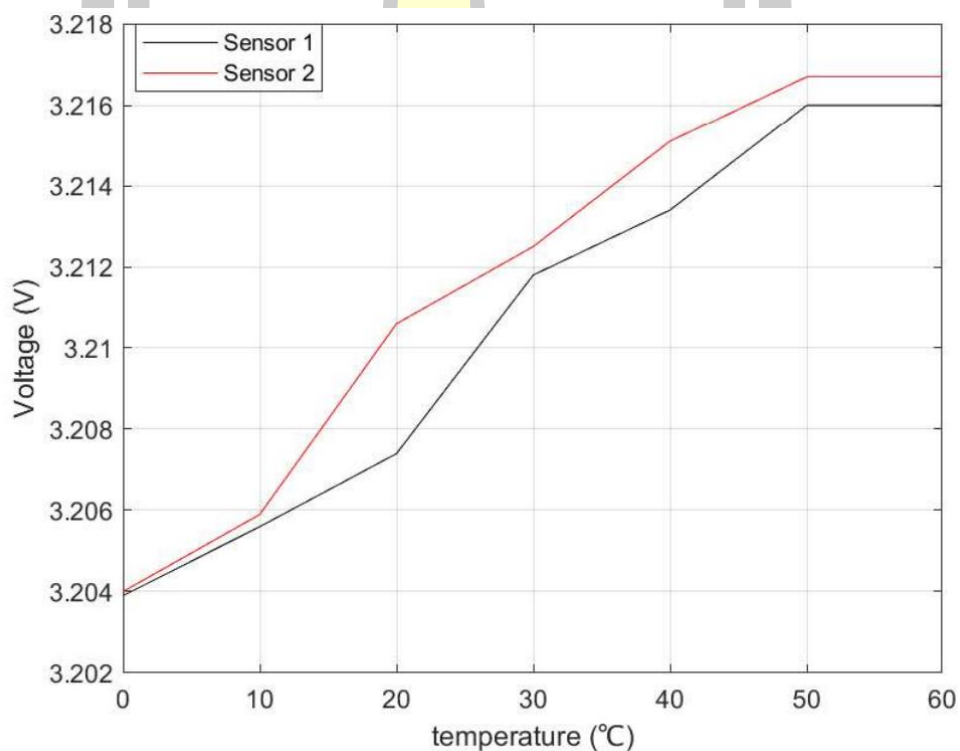


Figure 24 V-T diagram of fluxgate sensor without aerogel structure
The following conclusions can be drawn from the analysis of the test data:

1. Temperature has a significant effect on the output voltage (magnetic induction) of a fluxgate sensor. The output voltage of the sensor gradually increases as the temperature increases, while a decrease in temperature results in a gradual decrease in

the output voltage. This indicates the existence of temperature drift in the fluxgate sensor under different temperature conditions.

2. During the cycle of warming and cooling, the consistency between the magnetic probes is good, i.e., the deviation of the measured value of each magnetic probe at the same temperature is small. This indicates that the magnetic fluxgate sensor has relatively consistent performance changes at different temperatures and has good stability.

3. Although individual magnetic probes exhibit temperature drift over the entire temperature range, their temperature drift amplitude is different. This means that different magnetic probes may require different calibration or compensation methods at different temperature conditions to ensure their measurement accuracy.

To simulate the magnetic field characteristics of the core at different temperatures, we can use the following magnetic field equations:

$$B = \mu(H + H_m \sin(\omega t)) \quad (13)$$

Where B is the magnetic induction, and μ is the magnetic permeability, and H is the magnetic field strength, and H_m is the maximum amplitude of the magnetic field, is the angular frequency, and t is the time. ω is the angular frequency, and t is the time.

However, in practical applications, temperature variations can have a significant impact on the magnetic field performance of the core. Therefore, we introduce the temperature coefficient T_C into the expression for H

$$H = H_0 * (1 + T_c (T - 20)) \quad (14)$$

H_0 is the initial magnetic field strength, T_c is the temperature coefficient, and T is the temperature.

In order to plot the hysteresis return of the core in MATLAB and to take the temperature effect into account, we can do the following. First, we define the required parameters and variables such as H_0 , T_c , ω , t , and T . Next, we create a nested loop to traverse the different temperatures and time points, calculate the magnetic field strength B at each point, and store the results in a matrix. Finally, we use MATLAB's

plotting functions to visualize the B-T mapping relationship, presenting the hysteresis return line of the core as a function of temperature.

This approach will allow this study to more professionally model the magnetic properties of iron cores, taking into account the important effect of temperature on their performance, in order to plot an exhaustive B-T mapping relationship.

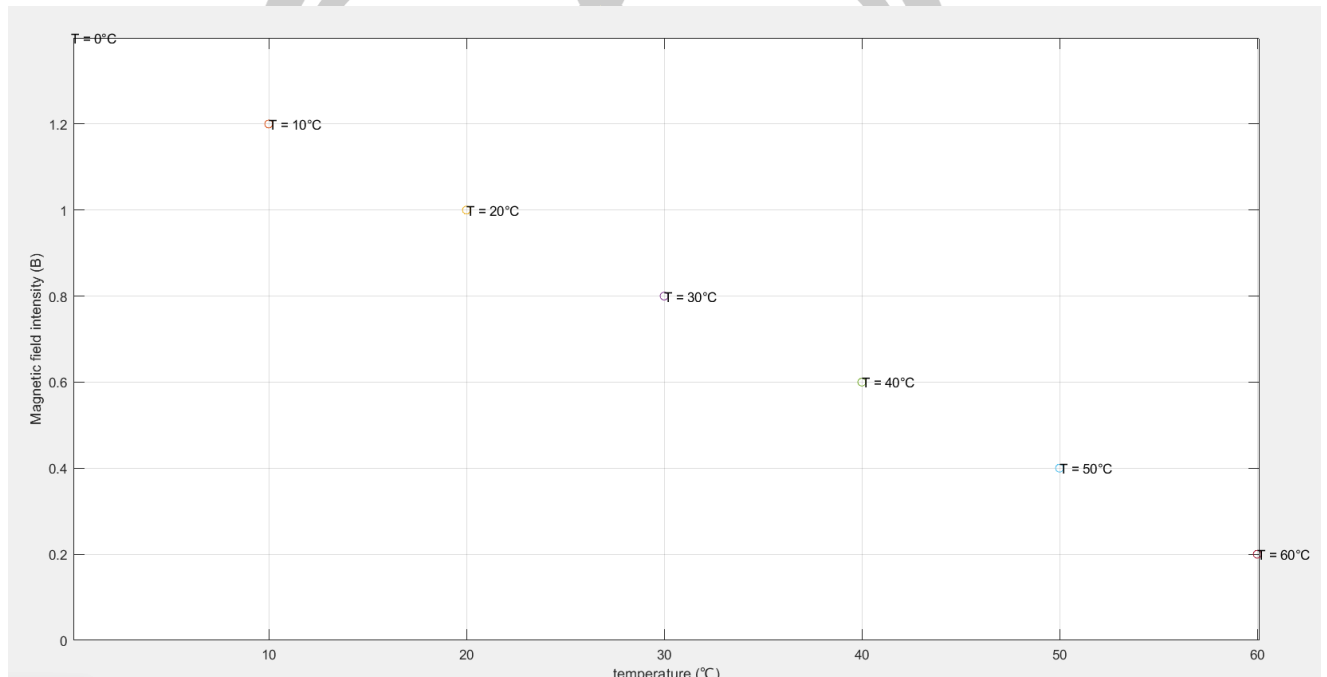


Figure 25 B-T Mapping Relationship

For in-depth modeling of fluxgate sensors, various influences are involved, including temperature drift, saturation effects, and magnetic material properties. A more specific modeling process is described below:

Temperature drift modeling:

Considering the output voltage of a Hall element as a function of temperature, we can use the following equation.

$$V_{out}(T) = V_{out0} \cdot (1 + \alpha \cdot (T - T_0)) \quad (15)$$

where: $V_{out}(T)$ is the output voltage after considering temperature drift.

V_{out0} is the reference temperature.

T_0 is the output voltage at the reference temperature.

α is the temperature coefficient, which can be positive or negative depending on the material properties.

Modeling of saturation effects:

Saturation effects can be modeled by introducing a saturation function. For the magnetic induction B and the applied magnetic field $B_{applied}$ relationship between them, we can use:

$$B = B_{applied} \tanh\left(\frac{B_{applied}}{B_{saturation}}\right) \quad (16)$$

Where. $B_{saturation}$ is the saturated magnetic induction.

The Jiles-Atherton model:

This model is based on the principle of energy balance within ferromagnetic materials. It describes the evolution of the magnetic moment of a ferromagnetic material with time in the presence of a magnetic field. The model divides the magnetization strength M into two parts, where M_{rev} denotes the reversible part and M_{irr} denotes the irreversible part. This division allows the model to better describe the behavior of the material in a circulating magnetic field, including the effects during demagnetization. The irreversible magnetization process in ferromagnetic materials is responsible for hysteresis and the formation of hysteresis loops.

$$H_e = H + \alpha M \quad (16)$$

$$M = M_{rev} + M_{irr} \quad (17)$$

$$M_{rev} = c (M_{an} - M_{irr}) \quad (18)$$

H is the magnetic field strength; α is the mean field coefficient (representing the coupling between magnetic domains); M is the magnetization strength; H_e is the effective magnetic field strength; M_s is the saturation magnetization strength; M_{an} is the hysteresis-free magnetization strength; and M_{irr} is the irreversible magnetization strength; M_{rev} is the reversible magnetization strength and c is the magnetic domain wall bending constant.

The hysteresis-free magnetization strength can be expressed as:

$$M_{an} = M_s \times \left[\coth\left(\frac{H_e}{a}\right) - \left(\frac{a}{H_e}\right) \right] \quad (19)$$

Differential equation for the intensity of irreversible magnetization.

$$\frac{DM_{irr}}{dH} = \frac{(M_{an} - M_{irr})}{(k\delta - \alpha(M_{an} - M_{irr}))} \quad (20)$$

δ is the direction of change of the magnetic field strength, the if $\frac{dH}{dt} > 0$ $\delta = 1$; else $\delta = -1$;

From the above relationship, the magnetization strength is related to the magnetic field strength as:

$$\frac{dM}{dH} = \frac{M_{an} - M}{(1+c)(k\delta - \alpha(M_{an} - M_{irr}))} + \frac{c}{1+c} \frac{dM_{an}}{dH} \quad (21)$$

The 4th order Runge-Kutta method is a method for numerically solving ordinary differential equations (ODEs). This method estimates the location of the next point by calculating the average slope of the step equation. For the Jiles-Atherton (J-A) model, we can use this method to solve its differential equations.

$$Y_{n+1} = y_n + h\phi(x_n, y_n, h) \quad (22)$$

$$\Phi(x_n, y_n, h) = \sum_{i=1}^r c_i K_i \quad (23)$$

$$K_1 = f(x_n, y_n) \quad (24)$$

$$K_i = f(x_n + \lambda_i, h, y_n \sum_{j=1}^{i-1} \mu_{ij} K_j), i=2, \dots, r \quad (25)$$

Where c_i, λ_i, μ_{ij} are all constants.

Based on the above equation to obtain the 4th order Runge-Kutta method, it is necessary to let $r = 4$, then we have the formula for the 4th order Runge-Kutta method as follows.

$$K_1 = f(x_n, y_n) \quad (26)$$

$$K_2 = f\left(x_n + \frac{h}{2}, y_n + \frac{h}{2} \times K_1\right) \quad (27)$$

$$K_3 = f\left(x_n + \frac{h}{2}, y_n + \frac{h}{2} \times K_2\right) \quad (28)$$

$$K_4 = f\left(x_n + h, y_n + h \times K_3\right) \quad (29)$$

$$Y_{n+1} = y_n + \frac{K_1 + 2K_2 + 2K_3 + K_4}{6} \times h \quad (30)$$

Where x_n is the current time, h , y_n is the current state, and h is the time step.

The Jiles-Atherton model was solved numerically in MATLAB using the fourth-order Runge-Kutta method, and the hysteresis regression line was obtained as in Fig. 26.

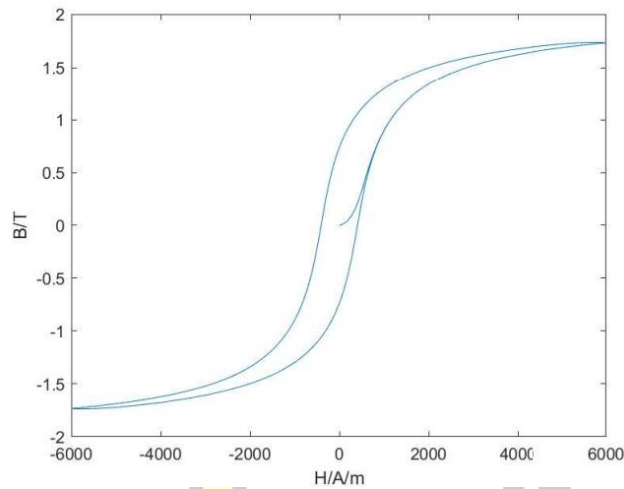


Figure 26 Hysteresis regression line

Now, we introduce the effect of temperature. Typically, the effect of temperature can be modeled by the temperature dependence of the material parameters.

$$M_{an} = M_{an0} + a(T - T_0) \quad (31)$$

Where M_{an0} is the reference temperature T_0 the hysteresis-free magnetization intensity at a is the temperature coefficient.

Introducing this temperature dependence into the original Jiles-Atherton model, we get:

$$\frac{dM}{dH} = \frac{(M_{an0} + a(T - T_0)) - M}{(1 + c)(k\delta - \alpha(M_{an0} + a(T - T_0)) - M_{irr})} + \frac{c}{1 + c} \frac{dM_{an0} + a(T - T_0)}{dH} \quad (32)$$

This equation describes the variation of the hysteresis loop with magnetic field strength, taking into account the effect of temperature. In practical applications, the parameters a and other temperature-dependent parameters need to be obtained by fitting experimental or literature data.

The B-H hysteresis regression lines for different temperature conditions are shown in Fig. 27:

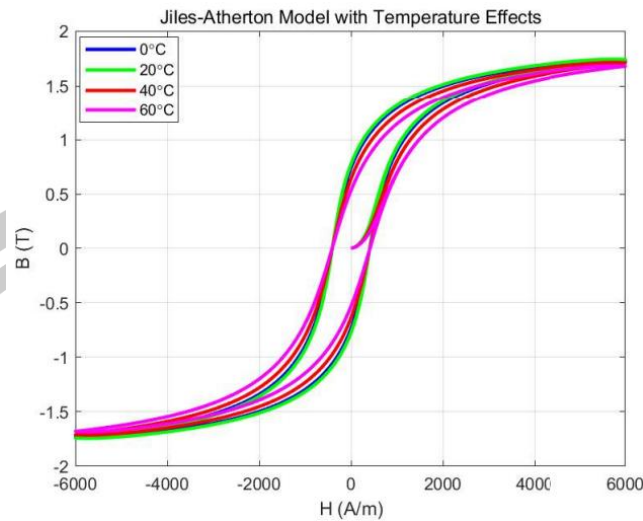


Figure 27 MATLAB fitting of hysteresis return curve with temperature

The saturation depth of the hysteresis loop increases with temperature, i.e. the core material saturates more easily at higher temperatures. The saturation time increases with temperature, thus affecting the sensitivity of the sensor.

The introduction of this model allows the hysteresis loop properties to vary with temperature, more accurately describing the magnetic properties of ferromagnetic materials at different temperatures. In specific applications, the values of temperature-related parameters can be obtained by fitting experimental data to more accurately model the behavior of fluxgate sensors at different temperatures.

From the simulation results, it can be seen that when the core material changes at different temperatures, its electromagnetic properties may exhibit inconsistency and instability, which may negatively affect the performance of the sensor. This instability is mainly due to the temperature sensitivity of the core material, which may cause the electromagnetic performance of the sensor to change under different temperature conditions. This variation may affect the linearity of the sensor, making it more difficult to maintain consistency and thus making linear fitting and temperature compensation more difficult. Therefore, choosing the right core material as well as taking measures such as temperature compensation and quality control are very important in solving these problems. These measures can help ensure that the sensor has stable performance under different temperature conditions, thereby improving its suitability and accuracy.

4.2.2 Aerogel Insulation Structure Fluxgate Sensor

Silicon dioxide aerogels possess a number of outstanding physical properties, including high specific surface area ($635\text{m}^2/\text{g}$), high contact angle (153°), and low thermal conductivity (0.049 W/ m K). These properties make it an outstanding thermal insulator, particularly suitable for applications that operate under extreme temperature conditions. Utilizing the advantages of silica aerogel, this paper designs a fluxgate sensor structure with unique dual thermal regulation properties. This structure is able to exhibit excellent performance in both extremely cold environments (-30°C) and high temperature environments (100°C).

The sensor structure cleverly capitalizes on the temperature properties of aerogel. In cold environments, it has a special ability to delay reaching temperature equilibrium, thus maintaining the internal temperature at 20°C or higher. Similarly, in hot environments, the structure is able to effectively reduce the internal temperature to below 31°C in very hot environments (100°C).



Figure 28 Schematic of aerogel insulation

A model of a fluxgate structure with a 3 mm aerogel insulation wrapped around the periphery is built and thermal simulation of the model is performed. (a) is screenshot of the side of the simulation model ; (b) is screenshot of the front of the simulation model.

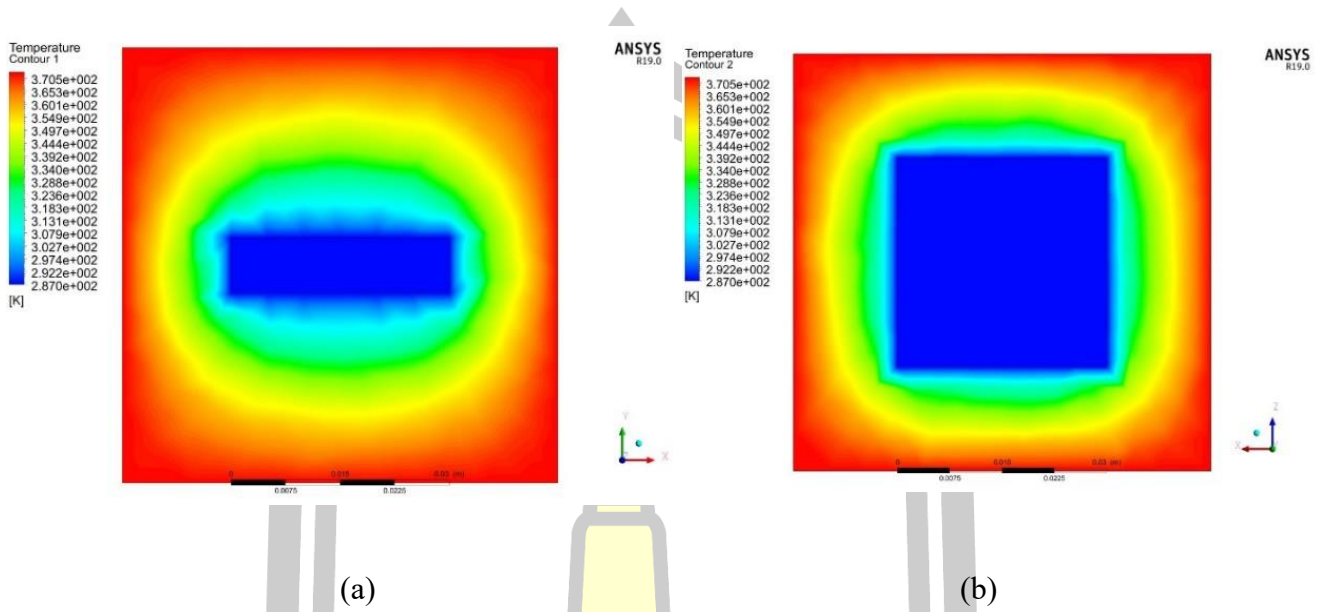


Figure 29 Screenshot of thermal simulation model of fluxgate aerogel insulation structure

Take the model centerline as a reference as in Fig. 30 and output the temperature distribution state curve:

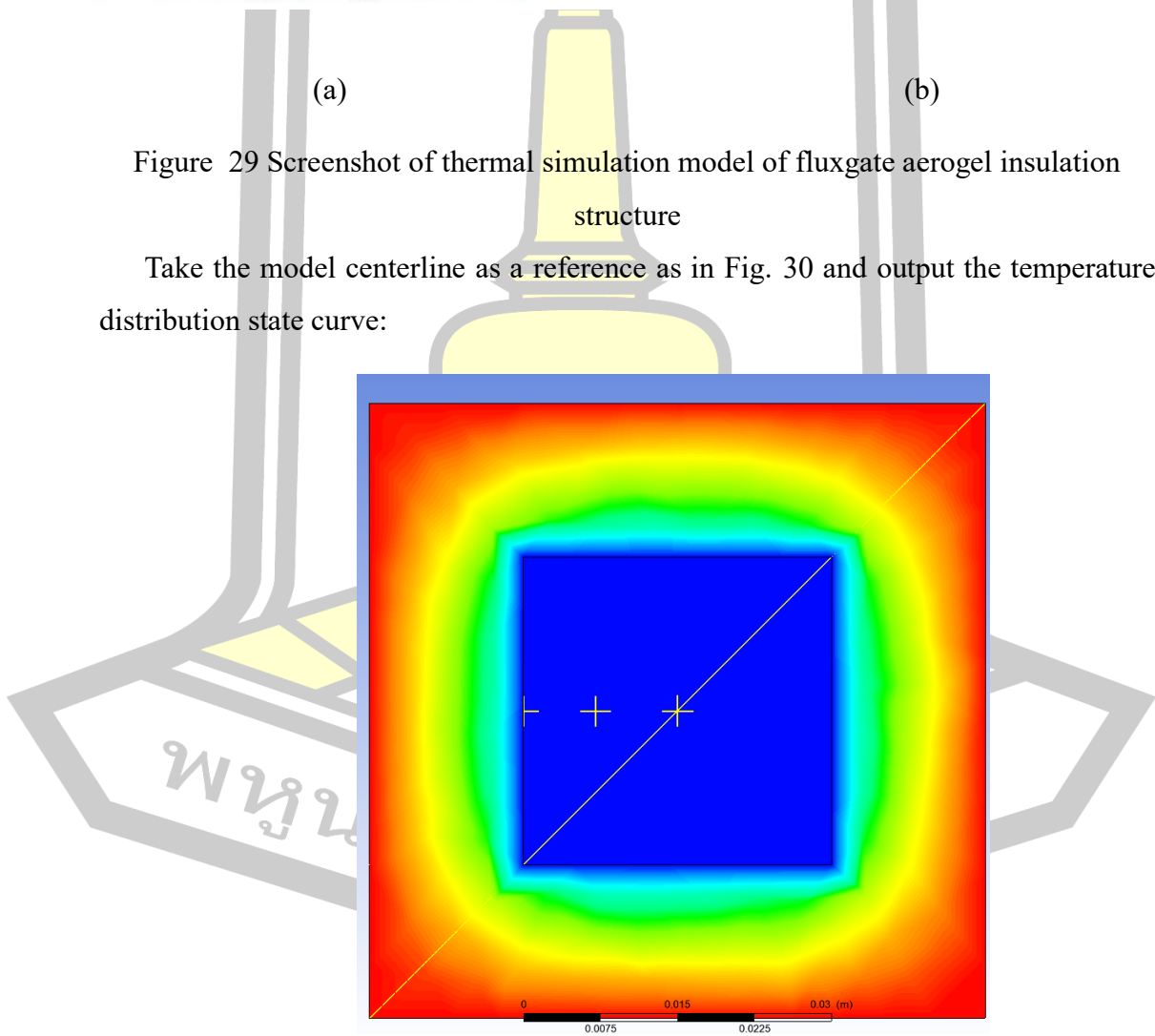


Figure 30 Centerline Schematic

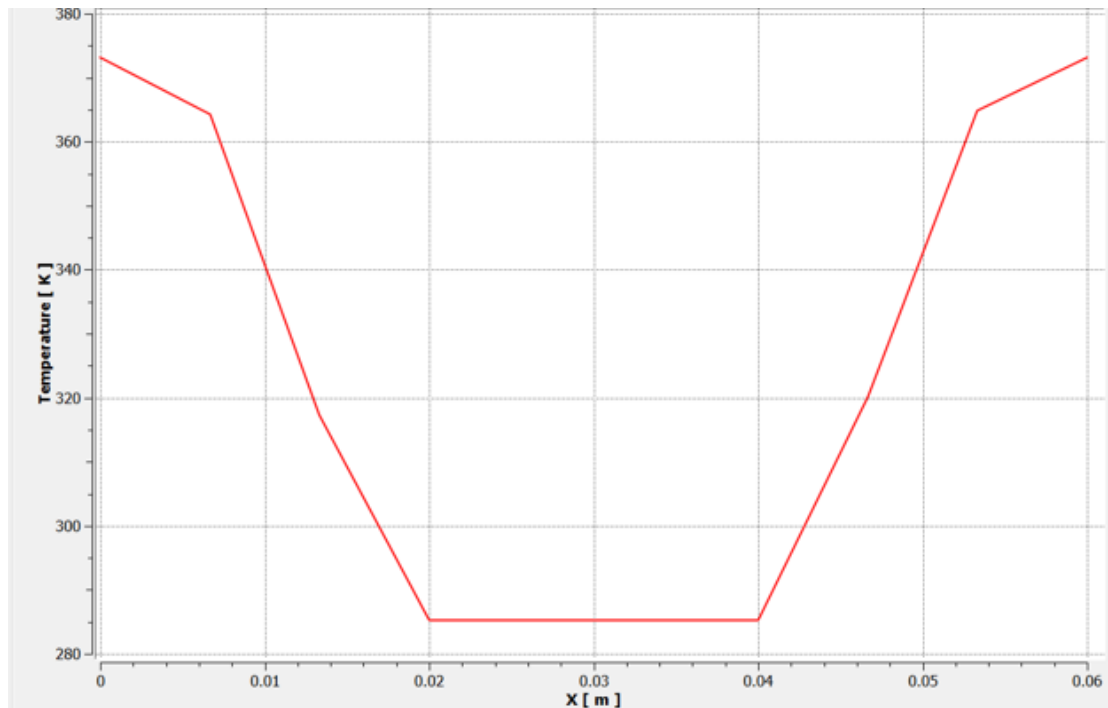
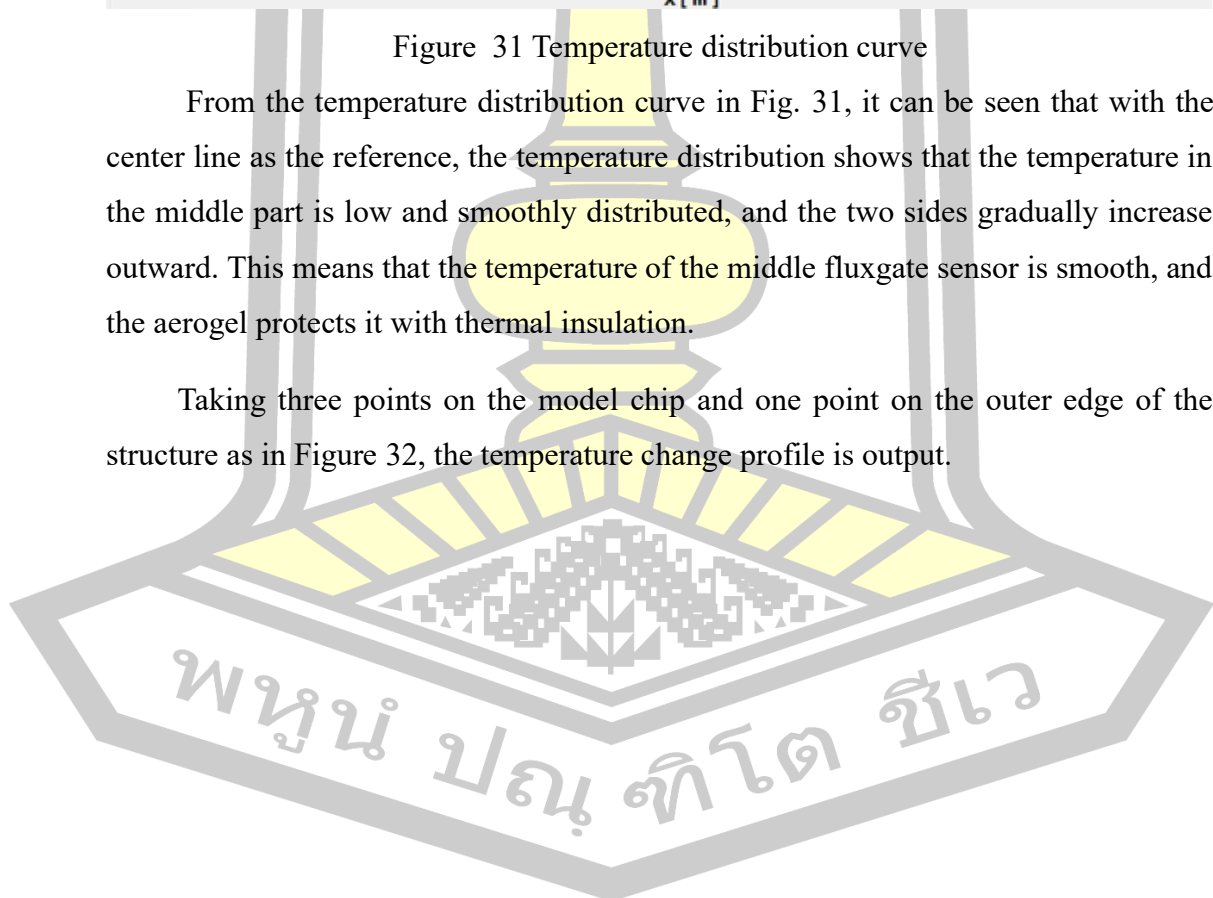


Figure 31 Temperature distribution curve

From the temperature distribution curve in Fig. 31, it can be seen that with the center line as the reference, the temperature distribution shows that the temperature in the middle part is low and smoothly distributed, and the two sides gradually increase outward. This means that the temperature of the middle fluxgate sensor is smooth, and the aerogel protects it with thermal insulation.

Taking three points on the model chip and one point on the outer edge of the structure as in Figure 32, the temperature change profile is output.



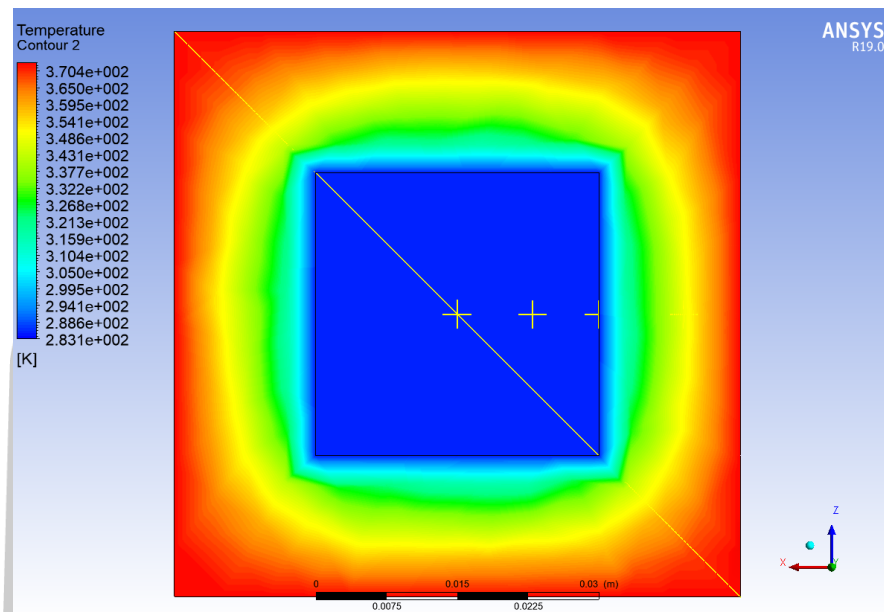


Figure 32 Schematic diagram of the pickup point

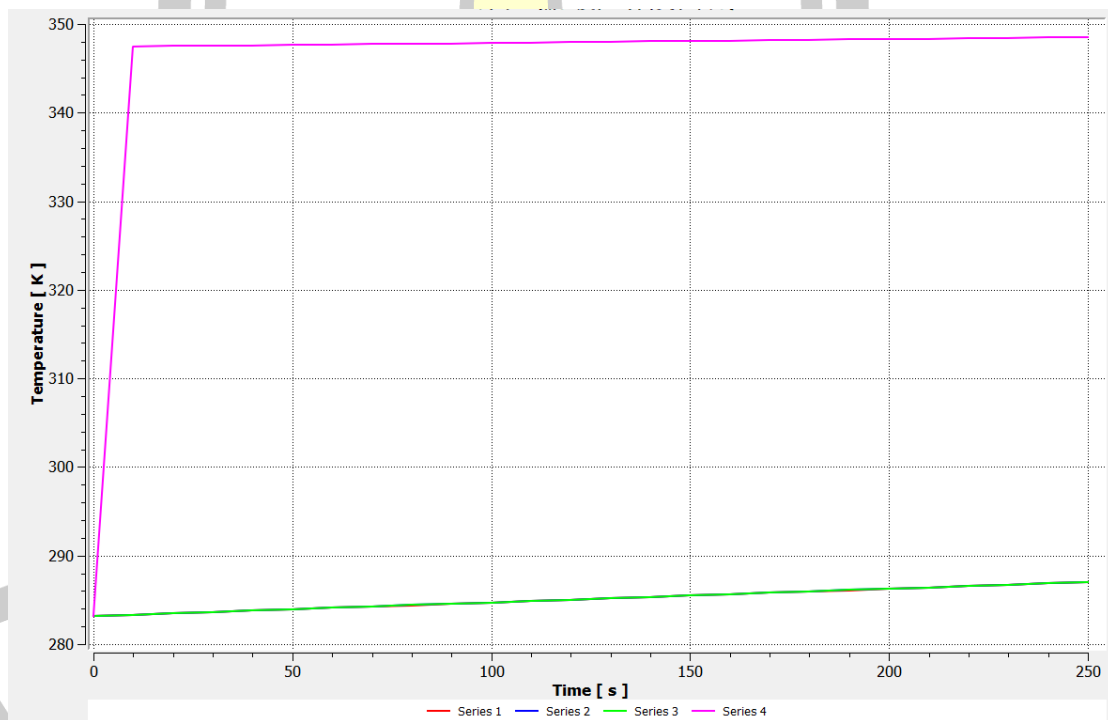


Figure 33 Temperature variation curves at different positions

From Fig. 31 we can observe that the temperature profile over time at the three points on the sensor is relatively smooth with a small rate of change, however, the temperature at the boundary points rises very quickly until it is in line with the ambient temperature.

A 3 mm thick aerogel layer was wrapped around the exterior of the fluxgate sensor and thermally simulated by ANSYS, which showed that the aerogel layer effectively insulated the fluxgate sensor. This thermal insulation creates a stable operating environment inside the sensor and greatly reduces the effect of temperature on its performance.

The most significant advantage of this design is that it effectively minimizes the negative impact of temperature changes on the performance of the fluxgate sensor. By minimizing the interference of temperature variations on performance, the structure is able to capture current information more accurately, allowing it to exhibit significant performance advantages over other fluxgate sensors. This innovative design provides a new solution for high-performance fluxgate sensors under temperature-varying charging pile engineering conditions, bringing important advances to the field of current measurement.

Overall, these analytical results emphasize the important effect of temperature on the performance of fluxgate sensors, and therefore, in practical applications, temperature compensation or calibration measures need to be considered to ensure the accuracy and stability of the sensors under different temperature conditions. The experimental adoption of SiO₂ aerogel measures to minimize the temperature-induced effects has a rather obvious advantage over algorithmic fitting for sensors with high consistency requirements.

4.3 Leakage Current Modeling and Analysis

The simulation model was developed in PLECS simulation platform in literature [47] and the simulation results are presented. The simulation parameters of the proposed CCMVI are shown in Table 7. The topology used for simulation is shown in Fig. 32.

Table 7 Simulation parameters of CCMVI [47]

Parameters	Values
Input voltage (V_g)	100 V
Grid phase voltage (peak)	150 V
PWM carrier frequency	10 kHz
Fundamental frequency	50 Hz
Capacitors (C_a, C_c and C_e)	470 μ F
Parasitic capacitor (C_{PE})	220 nF

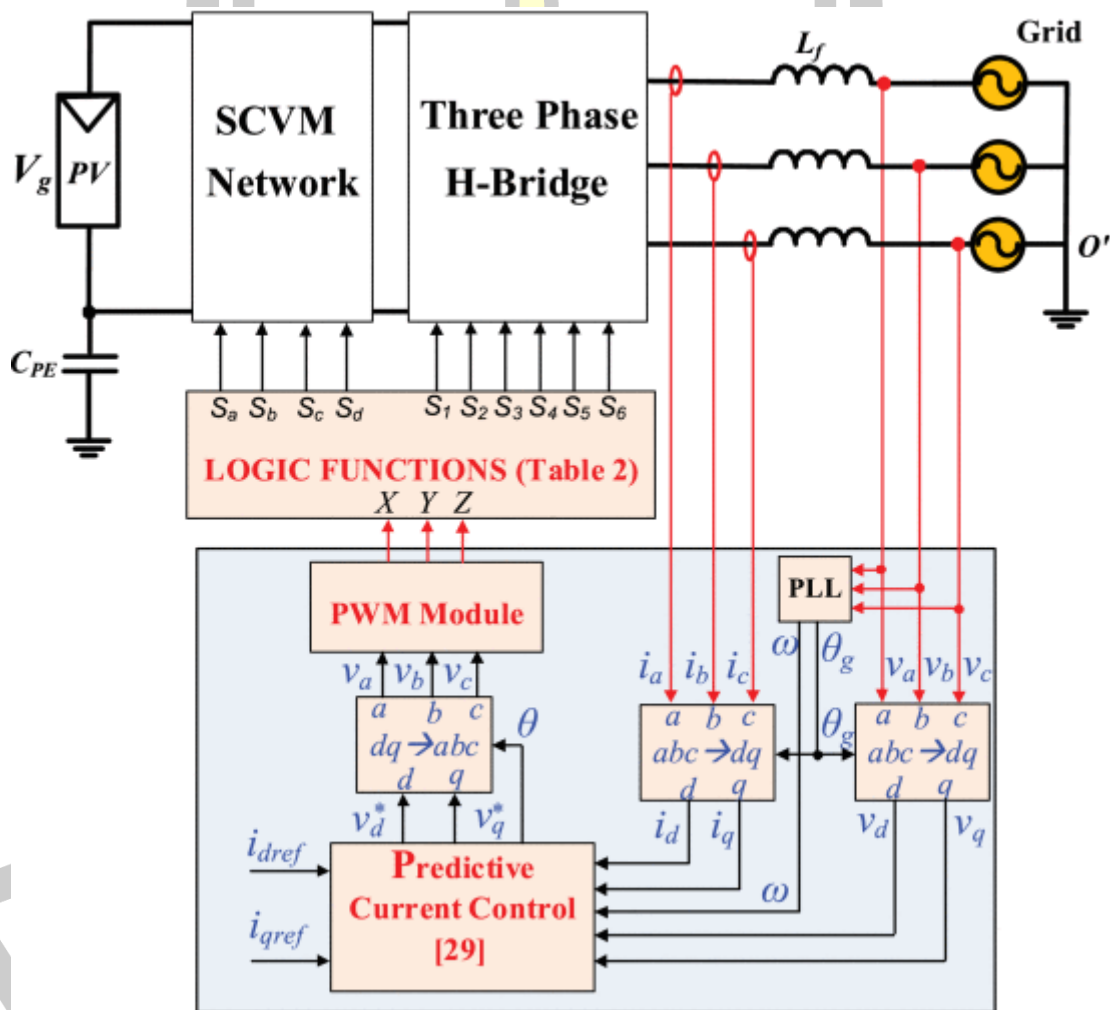


Figure 34 Simulation topology

As shown in Fig. 35, the proposed inverter injects a sinusoidal current of 6 A into the grid at $t = 0.2$ s. From Fig. 33, it can be seen that the CMV at the ends of the parasitic capacitors is about 0 V. The RMS value of the leakage current is about 0.5 mA. In this case, the harmonic spectral analyses of the grid current and the leakage current are shown in Fig. 34. The THD value of the grid current is about 1%.

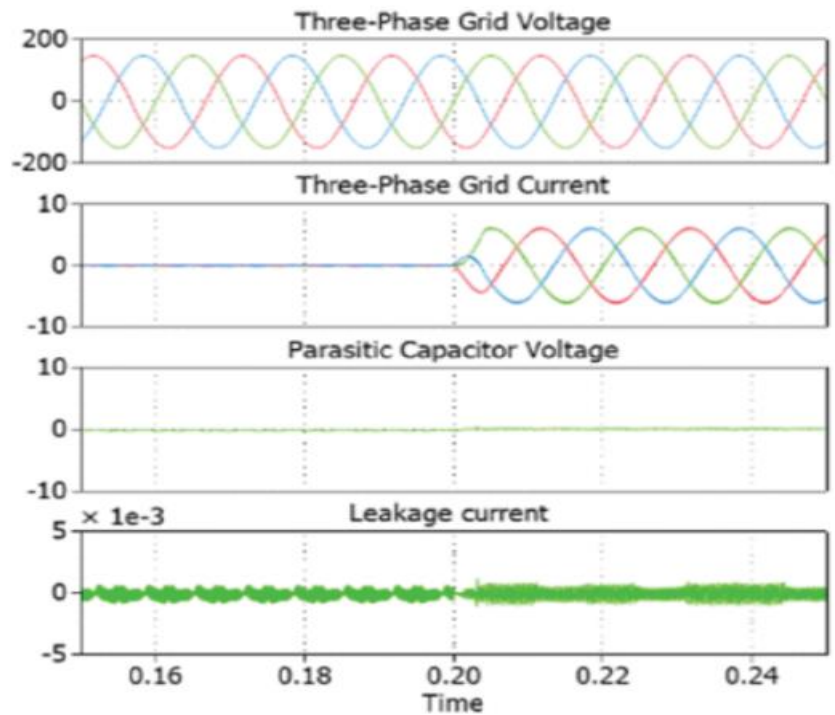


Figure 35 Numerical changes of indicators after changing injection current from 0 A to 6 A

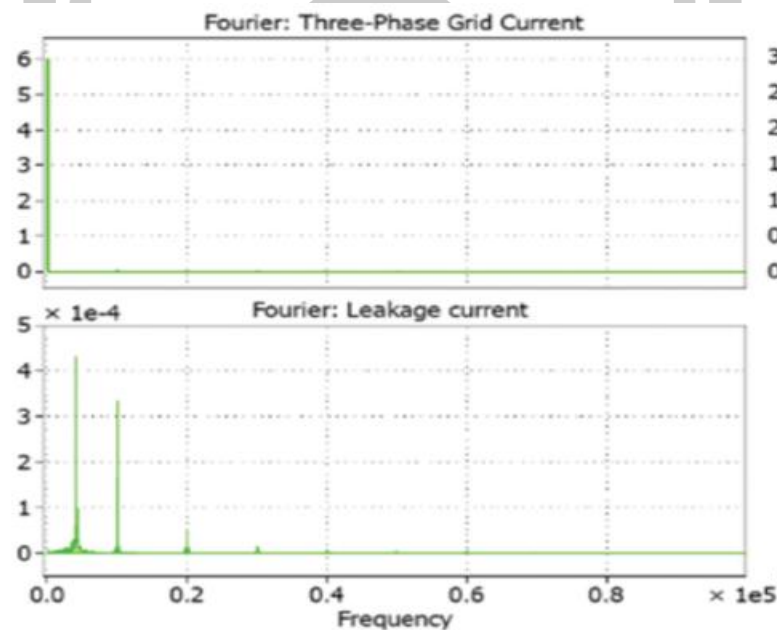


Figure 36 Harmonic spectrum of grid current and leakage current

In sensor design, the capacitance (C) between the sensor and the leakage current can be illustrated by the following theoretical equation, the relationship between the sensor and the leakage current can be expressed by the basic relationship between current and voltage

$$I_{leak} = C \frac{dV_{leak}}{dt} \quad (33)$$

I is the current and C is the capacitance between the sensor and the leakage current.

This equation illustrates the effect of capacitance on leakage current detection. By adjusting the size of the capacitance, the response of the leakage current signal to a change in voltage can be affected, thus adjusting the sensitivity of the sensor.

From the above simulation it can be seen that there are several sets of signals with different sizes, from which the data of leakage current is obtained and a matlab simulation model is built as in Fig. 36.

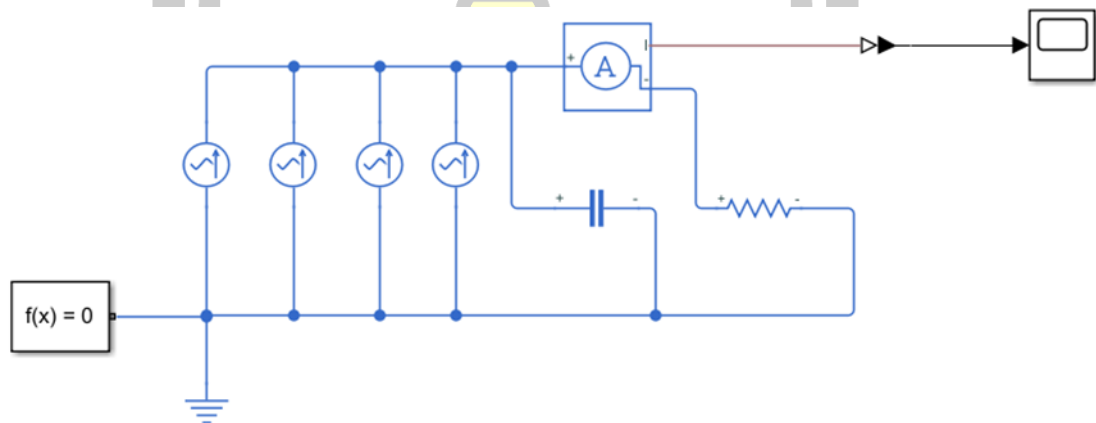


Figure 37 MATLAB leakage current simulation model

As shown in Fig. 36, the ideal waveform of leakage current obtained by the sensor under the condition that the value of capacitance between the relative leakage current of the sensor is zero.

พหุ ประถมศึกษา

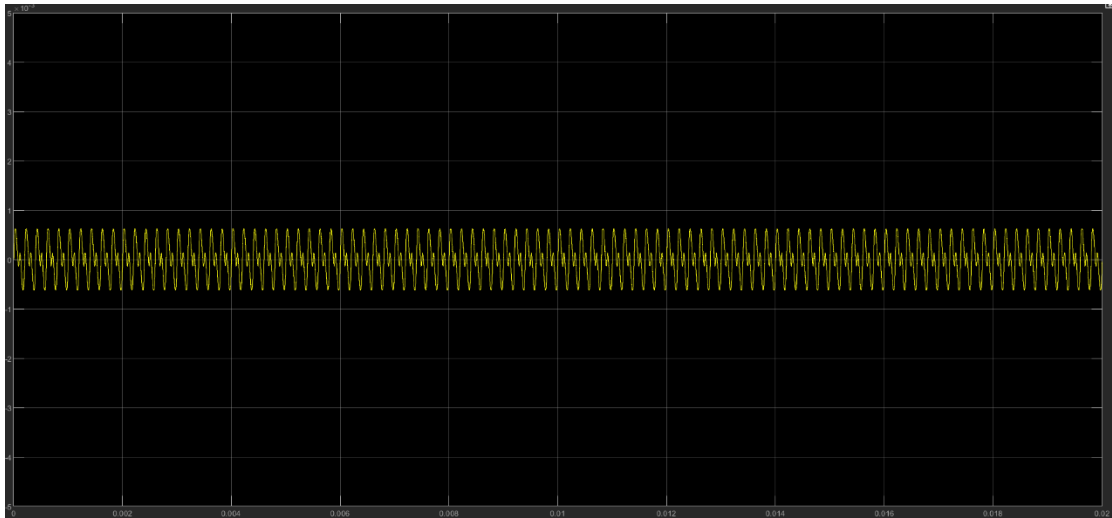
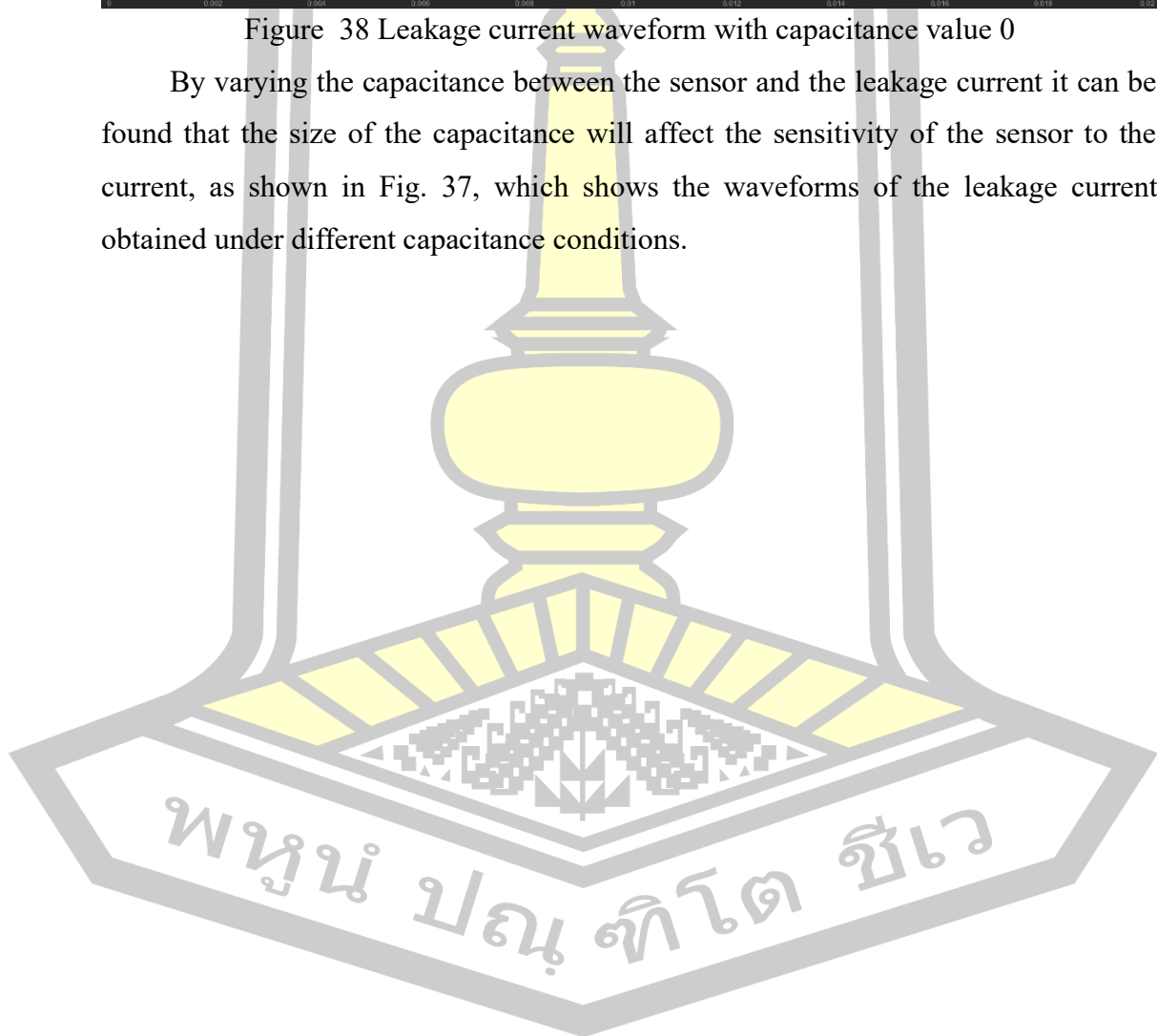
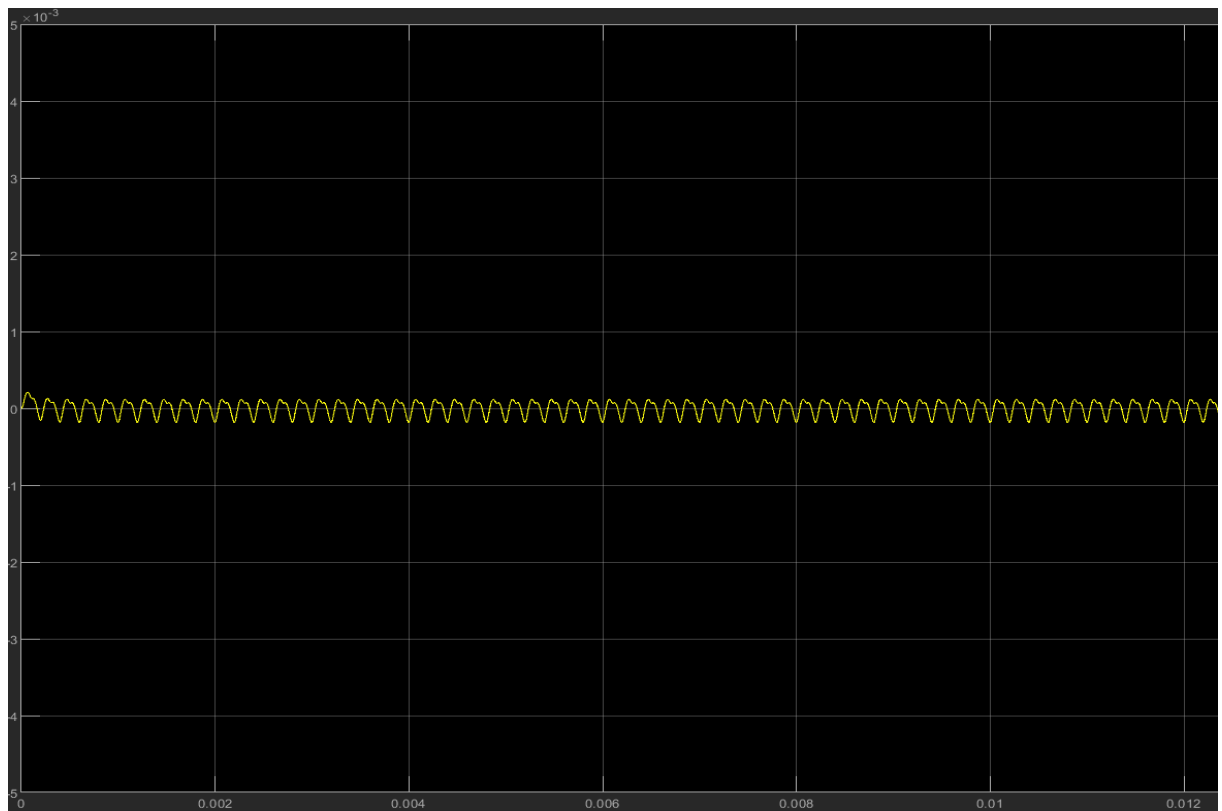


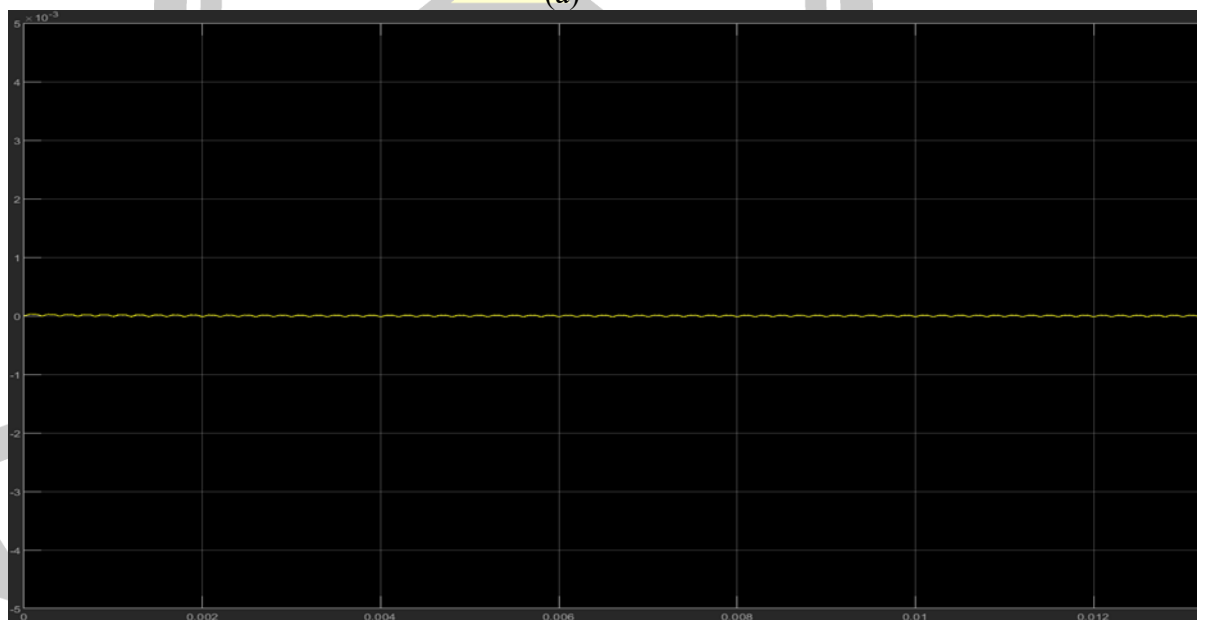
Figure 38 Leakage current waveform with capacitance value 0

By varying the capacitance between the sensor and the leakage current it can be found that the size of the capacitance will affect the sensitivity of the sensor to the current, as shown in Fig. 37, which shows the waveforms of the leakage current obtained under different capacitance conditions.





(a)



(b)

Figure 39 Leakage current waveforms obtained for different capacitance conditions

Leakage currents are usually small-amplitude, low-frequency signals, so capacitance should be selected with this in mind to better accommodate this characteristic. In sensor design, it is often desirable to choose an appropriate capacitance size that allows the sensor to respond well to the leakage current signal

without introducing too much noise. It is insightful to verify the effect of capacitance values on current signal acquisition through simulation results. This aids in a more thorough evaluation prior to actual fabrication and implementation.

Overall, considering the impact of capacitance size on sensor performance is a key factor in the design process, especially in application scenarios where accurate detection of small amplitude signals is required.



Chapter 5 Summary

5.1 Summary

The focus of this paper is on the causes of leakage current generation in a charging station converter system, which stems from the presence of incomplete insulation in the circuit, which leads to current flow to ground through unexpected paths. In order to gain a deeper understanding of this phenomenon, the study is analyzed in detail using circuit models and mathematical relational equations, focusing mainly on the generation mechanism of leakage current in the charging electrical system of the charging pile converter. In order to address the temperature characteristics and temperature drift of the fluxgate sensor, this study employs both experimental and MATLAB simulation methods. First, the experimental part evaluates the performance of the fluxgate sensor under different temperature conditions. These experiments were designed to analyze the output variation of the sensor at different temperatures to identify the effect of temperature on the sensor performance. The results of these experiments provide useful information about the temperature characteristics of the fluxgate sensor. To address the temperature drift problem, this paper proposes a solution by wrapping a 3 mm thick layer of aerogel around the exterior of the fluxgate sensor. This aerogel layer serves as a thermal insulator, which effectively mitigates the effect of sensor temperature fluctuations on performance and maintains the stability of the sensor's internal operating environment. To verify the effectiveness of this thermal insulation solution, thermal simulations were performed. The results of these simulations show that the aerogel thermal insulation layer significantly reduces sensor temperature fluctuations and ensures that the sensor is able to provide accurate leakage current measurements under different temperature conditions. This is critical for the personal safety of users in electric vehicle charging pile application scenarios as it improves the accuracy of the measurements and reduces the errors, thus better protecting the users from the potential risks associated with current leakage. Modeling and simulation of the leakage signal generated by the charging pile system combined with the leakage current sensor through MATLAB can help to provide an in-depth understanding of the system performance and the characteristics of the leakage current in order to better evaluate and improve the design of the leakage current sensor. This modeling and simulation process can help researchers better understand

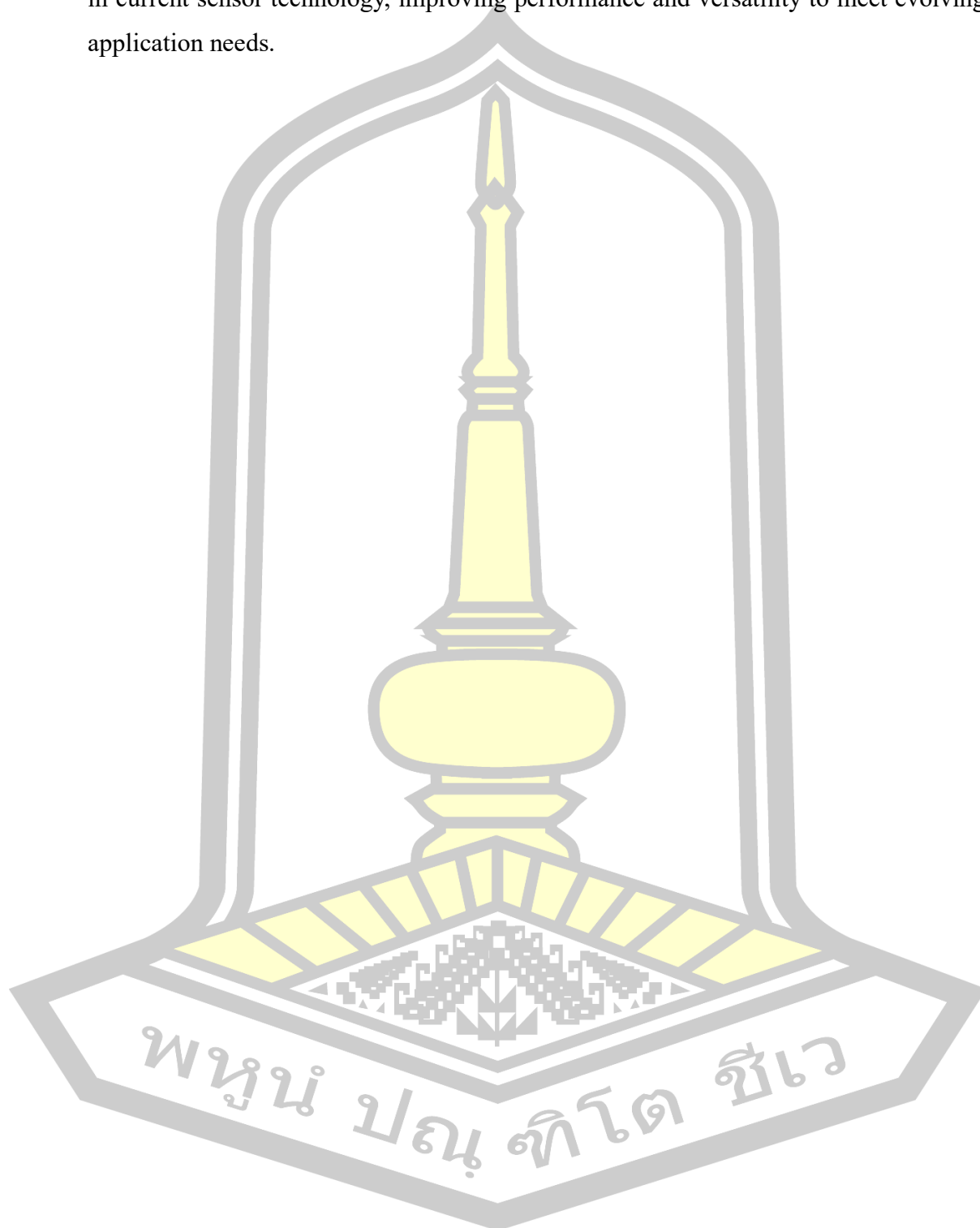
the leakage current problem, evaluate the impact of different design choices, reduce system risk, and provide better assurance of the safety and performance of electric vehicle charging piles. Factors affecting the measurement accuracy of fluxgate current sensors are explored in the study, and a temperature compensation strategy for these factors is proposed. By using SiO₂ aerogel thermal insulation, the experimental results show that this innovative temperature insulation method is more effective than the traditional temperature compensation method.

5.2 Prospects for work

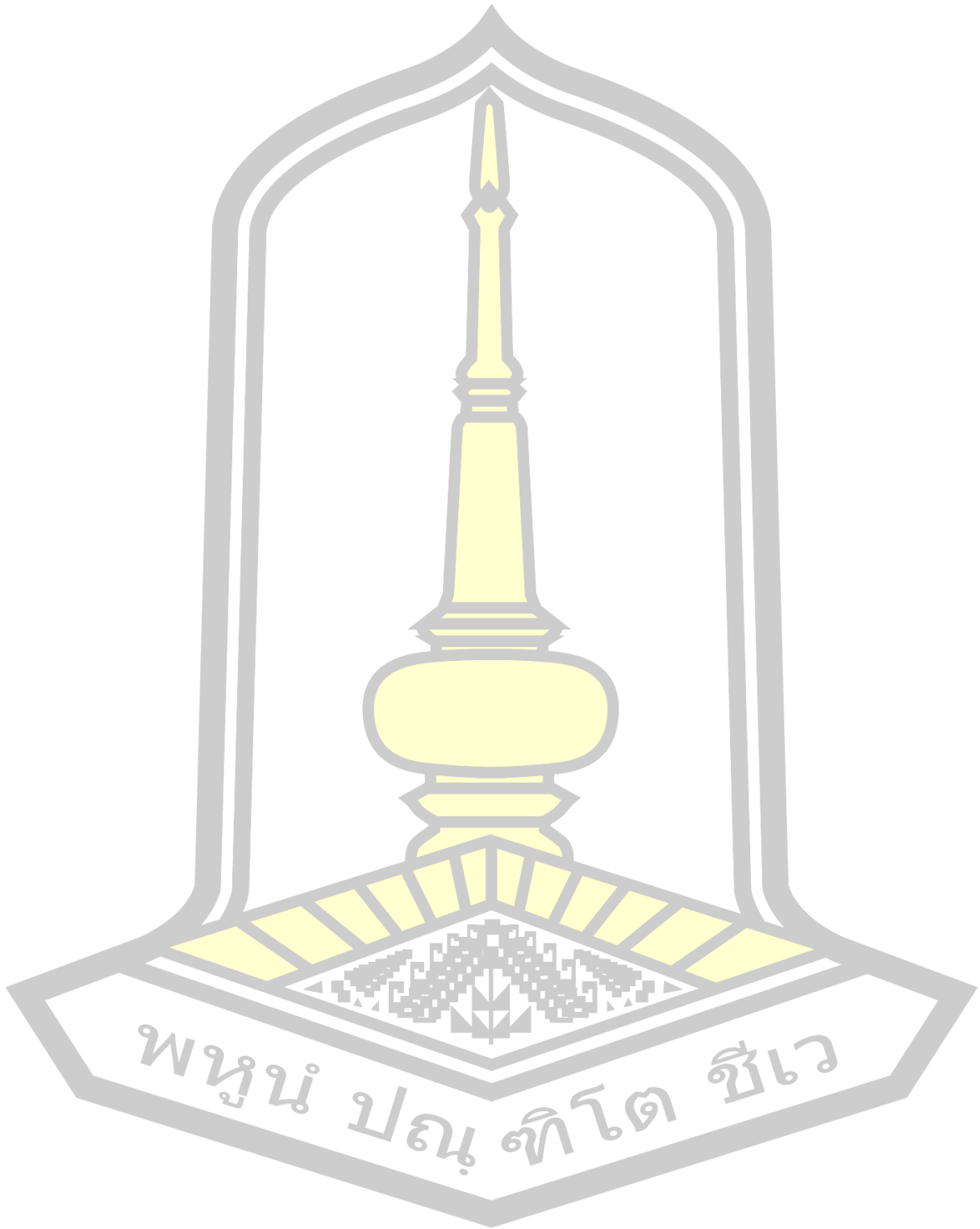
This leakage current only sensor is very promising and will further advance charging pile technology. Here are some extended ideas:

1. Versatility: Integrating temperature measurement into a smart current sensor is a great idea. This would allow the sensor to be used not only for current measurement, but also to provide environmental monitoring. This would be very useful for applications that require monitoring of environmental conditions, such as industrial automation or temperature sensitive laboratory environments.
2. energy efficiency Considering the battery life, future designs could focus more on energy efficiency. This may include the use of low-power chips, energy harvesting technologies (e.g., photovoltaic cells or vibrational energy harvesting) to extend the stand-alone operation time of the sensor.
3. IoT integration: Consider integrating sensors with Internet of Things (IoT) platforms. This will make data collection easier and enable users to monitor current and temperature data via smartphones or computers.
4. Security enhancements: Consider network security in the design. This will help protect sensor data, especially where privacy or critical infrastructure is involved in the application.
5. Application diversification: focus on exploring more different application areas. Current sensors can be used in a variety of fields, such as electric vehicle charging, solar power plant monitoring, industrial automation, home energy management.

Successful implementation of future work may lead to additional innovations in current sensor technology, improving performance and versatility to meet evolving application needs.



REFERENCES



- [1] International Energy Agency (IEA), "Global EV Outlook 2021."
- [2] Market Research Future, "Electric Vehicle Market Research Report - Global Forecast to 2025."
- [3] Mao, Ling, Zhang, Zhonghao, Zhao, Jinbin, Qu, Keqing, & Li, Fen. 2011 A new species of the genus *Pterostilbene* (Coleoptera, Staphylinidae) from China. (2022). Current status and outlook of vehicle-pile-network convergence technology. *Journal of Electrotechnology*, 37(24), 6357-6371.
- [4] State Council of China, "Made in China 2025."
- [5] European Alternative Fuels Observatory (EAFO), "Incentives and Taxation for Electric Vehicles in Europe."
- [6] U.S. Department of Energy, "Federal Incentives for Electric Vehicles."
- [7] Xinhua Net, "China's Electric Vehicle Charging Piles Reach 3,581,000 Units." May 9, 2022.
- [8] Wang K. The Design & Research of New Energy Vehicle Facilities. Diss. Beijing: Beijing Institute of Technology, 2015.
- [9] Liu, Y. Liu, M. Lu, and G. Li. " Discussion On The Future Development Trend Of High Power Charge." *Automotive Practical Technology* 14 (2018): 7-11.
- [10] Zeng, Rong ,et al." A Prospective Look on Research and Application of DC Power Distribution Technology." *Chinese Journal of Electrical Engineering* 38.23 (2018): 6791-6801.
- [11] Wang, F., et al. " Analysis on potential causes of safety failure of new energy vehicles." *Energy Storage Science and Technology* 11.5 (2022): 1411.
- [12] Zhang, Yue, et al. "Leakage current issue of non-isolated integrated chargers for electric vehicles." 2018 IEEE Energy Conversion Congress and Exposition (ECCE). IEEE, 2018.
- [13] C.L. Liao, X.C. Cui, and Y.J. Xiong. " Analysis on potential causes of safety failure of new energy vehicles." *Electrical Measurement and Instrumentation* 52.22 (2015): 100-107.
- [14] Lenz, James, and S. Edelstein. "Magnetic sensors and their applications." *IEEE Sensors journal* 6.3 (2006): 631-649.

- [15] Lopez, Oscar, et al. "Eliminating ground current in a transformerless photovoltaic application." *IEEE transactions on energy conversion* 25.1 (2010): 140-147.
- [16] Xiao H. F. Research on the Key Technologies for High-efficiency Utilization of Photovoltaic Generators. Nanjing: Nanjing University of Aeronautics and Astronautics, 2010.
- [17] Xiao, H. F., et al. "Study on Leakage Current Model for Transformerless Photovoltaic Grid-connected Inverter." *Chinese Journal of Electrical Engineering* 18 (2010): 9-14.
- [18] Zhou, X. Y., et al. "Effect of SVPWM vector synthesis methods on the DC bus charge station leakage current." *Power System Protection and Control* 41.21 (2013): 1-8.
- [19] Maalandish, Mohammad, et al. "Leakage current elimination with improved non-isolated nine-level inverter for grid-connected PV panels." *Journal of Energy Management and Technology* 1.2 (2017): 46-55.
- [20] Li, Hong, et al. "An improved H5 topology with low common-mode current for transformerless PV grid-connected inverter." *IEEE Transactions on Power Electronics* 34.2 (2018): 1254-1265.
- [21] Freddy, Tan Kheng Suan, et al. "Modulation techniques to reduce leakage current in three-phase transformerless H7 photovoltaic inverter." *IEEE Transactions on Industrial Electronics* 62.1 (2014): 322-331.
- [22] H. Ma, P. Shao, and L. Lan. "H10 three-phase inverter with forward and reverse clamping circuit for leakage current suppression." *Electric Machines & Control/Dianji Yu Kongzhi Xuebao* 26.11 (2022).
- [23] Concari, Luca, et al. "H8 inverter for common-mode voltage reduction in electric drives." *IEEE Transactions on Industry Applications* 52.5 (2016). 4010-4019.
- [24] Matiushkin, Oleksandr, et al. "Comparative Analysis of Buck-Boost Inverters Based on Unfolding Circuit Versus H5, H6, HERIC Topologies." *2022 International Symposium on Power Electronics, Electrical Drives, Automation and Motion (SPEEDAM)*. IEEE, 2022.
- [25] Jakka, Venkat N., et al. "Voltage balancing of series connected clamping diodes in medium voltage npc converter enabled by gen-3 10 kv sic mosfets for asynchronous

ronous micro-grid power conditioning system (ampcs)." 2019 IEEE Energy Conversion Congress and Exposition (ECCE). IEEE, 2019.

[27] Liu, Jie, et al. "Grounding Fault Model of Low Voltage Direct Current Supply and Utilization System for Analyzing the System Grounding Fault Characteristics ." *Symmetry* 13.10 (2021): 1795.

[28] Ren Chaojun. (2022). Research on Electric Shock Protection Technology for Non-Isolated Low Voltage DC Power Supply System Master's Thesis, Beijing jiaotong University). <https://link.cnki.net/doi/10.26944/d.cnki.gbfju.2022.003710>doi:10.26944/d.cnki.gbfju.2022.003710 .

[29] Liu, Yongmei, et al. "An electric shock impedance modeling method of living organisms in low-voltage distribution network." 2016 China International Conference on Electricity Distribution (CICED). IEEE, 2016.

[30] Ziegler, Silvio, et al. "Current sensing techniques: a review." *IEEE Sensors Journal* 9.4 (2009): 354-376.

[31] Collomb, David, Penglei Li, and Simon J. Bending. "Nanoscale graphene Hall sensors for high-resolution ambient magnetic imaging." *Scientific reports* 9.1 (2019): 14424.

[32] Isolated Current and Voltage Transducers : Characteristics-Applications-calculations. 3rd Edition [EB/OL]. [2017-08-15]. http://www.lem.com/images/stories/files/Products/P1_5_1_industry/CH24101E.pdf

[33] Yuan, Kai-Xin, Ai-Min Du, and Heng Tang. " Progress on Optical Fiber Sensors Based on Graphene/Graphene Oxide." *Advances in Geophysics* 35.3 (2020): 1199-1204.

[34] Ripka, Pavel. "Review of fluxgate sensors." *Sensors and Actuators A: Physical* 33.3 (1992): 129-141.

[35] LIU Tengfei. Study and Design of the Ring-Core Fluxgate Sensor [D]. Huazhong University of Science and Technology, 2010.

[36] XU Wei, ZOU Xudong, ZHANG Zhihong et al. Research progress of fluxgate sensors based on MEMS [J]. *Magnetic Materials and Devices*, 2023, 54(02): 95-101. DOI:10.19594/j.cnki.09.19701.2023.02.017

[37] Seitz, Thomas. "Fluxgate sensor in planar microtechnology." *Sensors and Actuators A: Physical* 22.1-3 (1990): 799-802.

- [38] Kawahito, S., et al. "Micromachined solenoids for highly sensitive magnetic sensors." TRANSDUCERS'91: 1991 International Conference on Solid-State Sensors and Actuators. Digest of Technical Papers. IEEE, 1991.
- [39] Belloy, E., et al. "A hybrid technology for miniaturized inductive device applications." Sensors and Actuators A: Physical 85.1-3 (2000): 304-309.
- [40] Andò, B., Baglio, S., Bulsara, A. R., Caruso, V., In, V., & Sacco, V. (2006, April). Investigate the optimal geometry to minimize the demagnetizing effect in RTD-Fluxgate. In 2006 IEEE Instrumentation and Measurement Technology Conference Proceedings (pp. 2175-2178). IEEE.
- [41] Snoeij, Martijn F., et al. "Integrated fluxgate magnetometer for use in isolated current sensing." *IEEE Journal of Solid-State Circuits* 51.7 (2016): 1684-1694.
- [42] Kankan Qi, Chao Shi, and Bing Lu. "Temperature Characterization of Fluxgate Sensor Probes." *Journal of Sensing Technology* 27.11 (2014): 1486-1489.
- [43] Pang, H. F., et al. "Study on Temperature Characteristic of Fluxgate Sensor Detectors." *Journal of Testing Technology* 25.3 (2011): 278-282.
- [44] Yin, Gongwei; Wang, Changming; Kong, Deren. Temperature Compensation of Fluxgate Magnetometer Based on BP Neural Network. 2007. PhD Thesis. Wuhan: Huazhong University of Science and Technology.
- [45] Yin, Gongwei, Wang, Changming, and Kong, Deren. Study of Feedback Coils and Magnetic Core Temperature Effect of Fluxgate Magnetometer. Diss. Wuhan: Huazhong University of Science and Technology, 2007.
- [46] Nie Yongzhong, Lin Mingchao. Rotational speed sensor [P]. Fujian Province: CN215297431U, 2021-12-24.
- [47] Tran, Tan-Tai, et al. "A three-phase constant common-mode voltage inverter with triple voltage boost for transformerless photovoltaic system." *IEEE Access* 8 (2020): 166692-166702.
- [48] Effect of high-power fast charging on charging cable temperature in electric vehicles. *New Energy Progress*, 7(2), 184-189.

BIOGRAPHY

NAME	Mingchao Lin
DATE OF BIRTH	1994/02/23
PLACE OF BIRTH	Quanzhou City, Fujian Province, China
ADDRESS	Quanzhou City, Fujian Province, China
POSITION	Student
PLACE OF WORK	-
EDUCATION	2018 B.Eng in Mechanical Engineering and Automation, Faculty of Mechanical and Electrical Engineering, Putian University, China 2024 M.Eng in Electrical and Computer Engineering, Faculty of Engineering, Mahasarakham University, Thailand
Research grants & awards	None
Research output	Paper

